SOLIDIFICATION SIMULATION OF BINARY Al-Si ALLOYS:

PREDICTION OF PRIMARY DENDRITE ARM SPACING WITH MACRO-SCALE SIMULATIONS (~1MM LENGTH SCALE)

SOLIDIFICATION SIMULATION OF BINARY Al-Si ALLOYS:

PREDICTION OF PRIMARY DENDRITE ARM SPACING WITH MACRO-SCALE SIMULATIONS (~1MM LENGTH SCALE)

By

HONGDA WANG, B.ENG., MASc.

A Thesis

Submitted to the School of Graduate Studies

in Partial Fulfillment of the Requirements

for the Degree of

Doctor of Philosophy

McMaster University

DOCTOR OF PHILOSOPHY (2009) **McMaster University**

(Mechanical Engineering) **Hamilton, Ontario**

TITLE: Solidification Simulation of Binary Al-Si Alloys: Prediction of Primary Dendrite Arm Spacing with Macro-Scale Simulations (~1mm Length Scale)

AUTHOR: Hongda Wang

B. Eng (Tongji University)

MASc. (McMaster University)

SUPERVISORS: Dr. Mohamed S. Hamed & Dr. Sumanth Shankar

NUMBER OF PAGES: **v, 136**

ABSTRACT

A new and improved algorithm and numerical method has been developed and validated to simulate the solidification of binary alloys considering optimized thermo-physical material properties, undercooling of the liquidus temperature prior to solidification event of the primary phase, fluid flow induced by natural convection and shrinkage during solidification in the solidifying domain. The simulation was for a two dimensional unsteady state solidification process inside a cylindrical container. The validation was carried out with reliable experiment results for both upward and downward solidification modes. An additional advantage of the present numerical algorithm is the estimation of the instantaneous primary dendrite arm spacing at any location in the solidified component. It has been shown that the Bouchard-Kirkaldy model (unsteady state solidification) to evaluate the primary dendrite arm spacing in an unsteady solidification process coupled with the Lehmann model to evaluate the primary arm spacing with the effect of fluid velocity in the liquid phase is accurate within acceptable error. The results from simulations using these models have a good agreement with experiment results for instantaneous primary dendrite arm spacing in the solidified microstructure. The effect of fluid flow on the evaluation of primary arm spacing is pronounced during downward solidification. However, the effect of primary arm spacing on fluid flow is insignificant, so it is acceptable to apply average primary arm spacing during macro-scale solidification simulations. To obtain a valid simulation, the thermo-physical material properties of the solid phase should be considered as function of temperature and that of the liquid can be considered as an average constant value. The inclusion of solidification shrinkage in the simulation has negligible effect on the solidification parameters during the upward solidification mode, however, significantly changes the direction and magnitude of the fluid velocity in the liquid phase and the magnitude of primary arm spacing in the downward solidification mode. A valid solidification simulation of binary alloys to estimate accurate primary dendrite arm spacing could be achieved only with the consideration of the undercooling of the liquidus temperature, optimized thermo-physical properties, and fluid flow in the domain caused by both solidification shrinkage and natural convection effects.

ACKNOWLEDGEMENTS

The author would like to express his deep and sincere gratitude to his supervisors Dr. Mohamed S. Hamed and Dr. Sumanth Shankar for their continuous guidance and advice. Their patient, encouragement and assistance throughout this project have made the past four years a memorable experience.

I would like also to thank my supervisory committee members: Dr. Nikolas Provatas and Dr. Stephen Tullis, for their encouragement and valuable suggestions.

Special appreciation is extended to Sharcnet for its high speed academic research computing network.

Last but not lease, I would like to thank my parents and my family, for their love and unconditional support. Thanks to my mom, Meiyun Lin; dad, Qinren Wang; wife, Ying Chen and sons, William and Edward.

CONTENTS

EXECUTIVE SUMMARY

In this executive summary, an introduction to this study, the motivation, key results and conclusions along with a brief summary of each publication that constitutes this dissertation shall be presented.

INTRODUCTION

Casting is one of the most common manufacturing routes for various aero-space, automotive, domestic and defense components. Typically casting alloys are binary eutectics in nature with small amounts of other alloying additions. The Al-Si hypoeutectic alloy and the Fe-C alloy are the most commonly used casting alloys. During their solidification, the primary phase usually evolves as dendrites followed the eutectic phases. While designing a cast component, the mechanical property and performance requirements for the design are initially estimated. The arm spacing between the primary and secondary dendrites in a cast microstructure is directly related to the mechanical properties of the component [1-8]. Figure 1 shows an example of a typical relationship between the dendrite arm spacing in the microstructure and the mechanical properties such as the Ultimate Tensile Strength (UTS). Figure 1(a) and Figure 11(b) show the effect of primary dendrite arm spacing (λ_1) and secondary dendrite arm spacing (λ_2) on UTS, respectively.

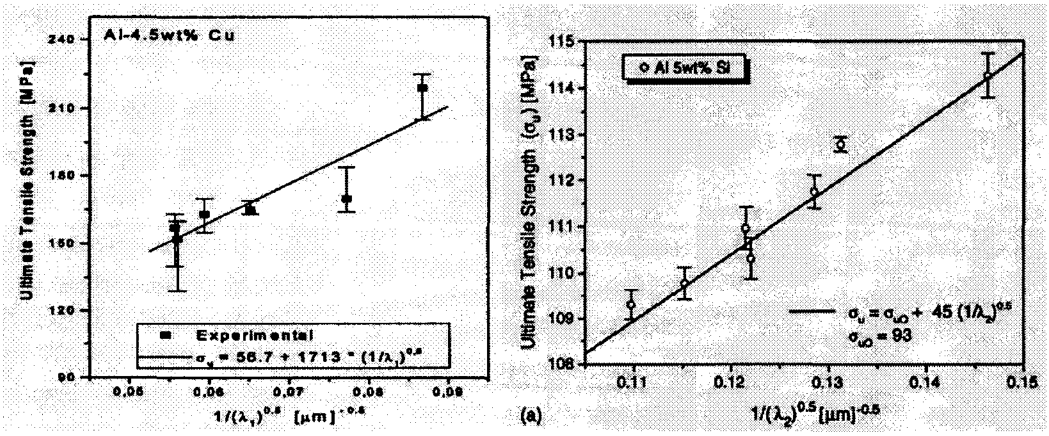

(a) (b)

Figure 1: Ultimate tensile strength distribution at various (1) Primary arm spacing (λ_1) for Al-4.5wt%Cu alloy [8]; (b) Secondary arm spacing (λ_2) for Al-5wt%Si alloy [4].

In order to achieve a required mechanical property for a cast component, certain primary and secondary arm spacing has to be obtained during solidification. The values of λ_1 and λ_2 strongly depend on the heat extraction process during solidification of the casting. Typically casting mould design, cooling system in the mould, melt pouring temperature and mould coating will have to be designed to obtain the required cooling rate for the casting and the required values of λ_1 and λ_2. Currently, casting processes are designed based on the experience of the designer of several experiments to identify the optimum mould parameters. A predictive tool to enable evaluation of λ_1 and λ_2 by numerical simulations would greatly enhance the efficiency of casting process design. Presently, there are two independent groups of researchers working on numerical solidification simulation of casting alloys, namely, the researchers working on the global (macro-scale) trying to evaluate the thermal, mass and momentum distribution in a casting mould with a control volume resolution of about 1 mm size [9-19], and the researchers who are working on a control volume scale of about 1 μm size (micro-scale) to evaluate mechanisms of solidification and prediction of λ_1 and λ_2 for the micro-scale computing domain [20-25]. The inability of the researchers working in the macro-scale simulations to predict λ_1 and λ_2 is a largely responsible for the lack of a valid simulation tool for casting designers. The main reasons for the prior art in macro-scale simulation to be unable to validate a solidification simulation and predict λ_1 and λ_2 are presented below:

- Until now the phenomenon of undercooling below the liquidus temperature during solidification could not be considered in the macro-scale simulations [9-19]. Undercooling is a critical phenomenon during solidification and greatly influences the values of λ_1 and λ_2 [26].
- Thermo-physical properties of the solid and liquid phases during solidification have not been optimized.

This dissertation is aimed at developing a valid numerical algorithm for the macro-scale solidification simulation of binary alloys and further enables direct prediction of λ_1 and λ_2.

Figure 2(a) shows the schematic a typical binary alloy phase diagram. Figure 2(a) also shows the solidification path for a typical hypoeutectic binary alloy with an average solute concentration of C_o. When this alloy solidifies from an initial temperature of T_{ini}, there are three distinct phase regions, namely, the liquid between T_{ini} and the liquidus temperature T_{liq}, a semi-solid region (mushy zone) where in the liquid and solid phases co-exist between T_{liq} and the solidus (eutectic) temperature T_{eut}, and the solid phase below T_{eut}. Typically the solidification does not commence at the T_{liq} but there is a distinct undercooling below the liquidus temperature (ΔT) contributed by the *kinetics of solidification, rate solute diffusion in liquid, and radius of the growing dendrite tip* [26]. Figure 2(b) shows a snapshot of typical uni-directional solidification (casting) process inside a cylindrical container along with the heat extraction direction and the details of primary arm spacing (λ_1). Typical temperature distribution in the mushy zone ranging from the eutectic temperature (T_{eut}) to initial temperature (T_{ini}) is also shown in Figure 2(a) along with the three distinct phase regions during solidification of binary alloys. The cooling rate, $\left(\frac{\partial T}{\partial t}\right)$ during solidification of this alloy is evaluated by the product of the temperature gradient, $G=\frac{\partial T}{\partial y}$ at the liquid/mushy zone interface (shown by point A) and the velocity of the growing dendrite tip, $R=\frac{\partial y}{\partial t}$ at the same point A. Specifically, $\left[\left(\frac{\partial T}{\partial t}\right)=G\cdot R=\left(\frac{\partial T}{\partial y}\right)\cdot\left(\frac{\partial y}{\partial t}\right)\right]$. The value of λ_1 is directly evaluated by the magnitudes of G and R in addition to the value of the flow velocity, U, at the liquid / mushy zone interface in Figure 2(a).

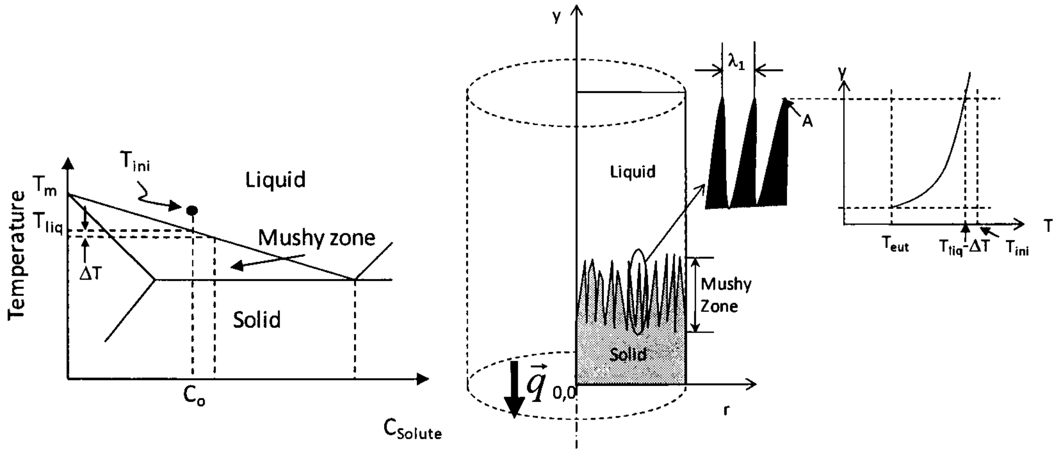

(a) (b)

Figure 2: Schematic of (a) typical phase diagram for metal alloys (b) the snapshot for casting process inside a cylindrical container with primary dendrite spacing (λ_1) and temperature distribution inside mushy zone.

It is critical to be able to carry out a valid solidification simulation of binary cast alloys in order to better predict the cast component quality (gas porosity/shrinkage) and the primary/secondary dendrite arm spacing (mechanical properties). Presently, there are two independent schools of solidification simulation of binary alloys. One deals with control volumes in the order of a micro-meter (micro-scale simulation) and the other in the order of a millimeter (macro-scale simulation). The valid prediction of the dendrite arm spacing in a solidification microstructure will require consideration of fluid flow, shrinkage, changes in thermo-physical materials properties and undercooling of the liquidus temperature prior to solidification of the primary phase. Presently, the state of the art is that the micro-model can predict the dendrite arm spacing but cannot incorporate the actual fluid flow observed in the domain and the macro-model could not predict valid arm spacing because the simulations could not incorporate the undercooling of the liquidus temperature. Hence, there have been no macro solidification simulation efforts that could be fully validated by experiment results for the values of the primary arm spacing.

In this study, we wish to present a new and improved algorithm and numerical procedure to evaluate valid primary dendrite arm spacing at any location of a uni-directionally solidified component. The alloys used in this study are the technologically important Al-Si hypoeutectic alloys, such as the Al - 3, 5 and 7 wt%Si. The other reason to use these alloys is that results for critically controlled directional solidification experiments for the validation of these simulations in both global and micro scales are available in the prior-art [27, 28]. The numerical method and the solidification simulation in present work could be used for other binary alloys with various solute concentrations as well. This algorithm has the ability to incorporate the undercooling of the liquidus temperature, transient fluid flow and solidification shrinkage to quantify the primary dendrite arm spacing during solidification. Further, the thermo-physical material properties of the solid and liquid phases have been optimized to enable a valid prediction of the arm spacing. Furthermore, the use of the new numerical procedure reduced the computing cost by half when compared to the existing procedures. The effect of undercooling was incorporated in the simulation by using Burden et al [29, 30] for evaluating undercooling in binary alloy systems. This model was chosen because it was the only recommended model for the range of solidification rates used in this study. There have been several models to predict the primary dendrite arm spacing without the effect of fluid flow in the solidification domain. Four of the popular models were used in this study to evaluate primary arm spacing without fluid flow: Hunt[31], Trivedi[32], Kurz-Fisher[33], Bouchard-Kirkaldy[34] models. The value of primary arm spacing from each of these four models were subsequently incorporated into the Lehmann model[35] which updates the primary arm spacing with the effect of transient fluid velocity. Bouchard-Kirkaldy[34] model coupled with the Lehmann model[35] is the only combination that predicted the primary arm spacing in an unsteady state solidification process.

Solidification simulations were carried out in two computing domains as shown in Figure 3(a) and Figure 3(b). The upward solidification mode is shown in Figure 3(a) wherein the mushy zone/liquid interface velocity is in the direction opposite to the gravity vector and in downward solidification mode shown in Figure 3(b) is in the same direction as the gravity vector. The two domains were selected because the fluid flow patterns in them are significantly different from each other. The upward solidification will have a diminished fluid flow velocity which is solely caused by the effect of solidification shrinkage, whereas, the downward solidification will have a strong fluid flow field caused by both shrinkage and natural convection in the domain (positive density gradient against the direction of gravity vector).

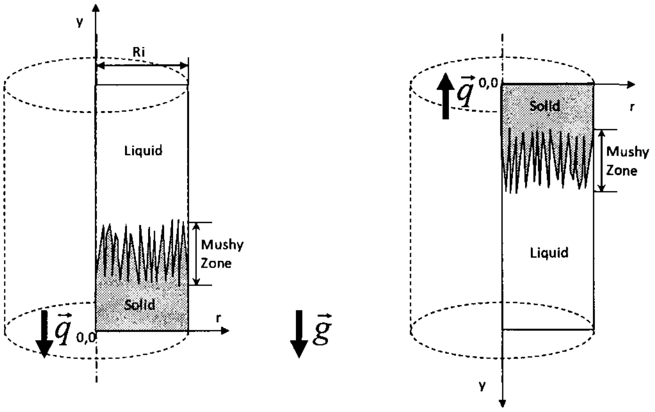

(a) (b)

Figure 3: Schematic during the solidification simulations. (a) upward solidification and (b) downward solidification.

The domains were designed such that the dimensions, thermal boundary conditions and velocity boundary conditions are similar to those used in experiments [27, 28] for each mode of solidification, respectively. The alloys were various compositions of Al-Si hypoeutectic alloys ranging between 3 wt% to 7 wt% Si. Peres et al [27] and Spinelli et al [28] performed experiments for upward and downward solidification inside a cylindrical domain, respectively.

Figure 4 shows the salient results for the primary arm spacing from this study. Figure 4 shows that amongst the several models[31-34] used to predict the primary dendrite arm spacing, the Bouchard-Kirkaldy model[34] coupled with the Lehmann model[35] showed the best agreement with experiment results[28] and that the optimized simulations with the new algorithm are valid.

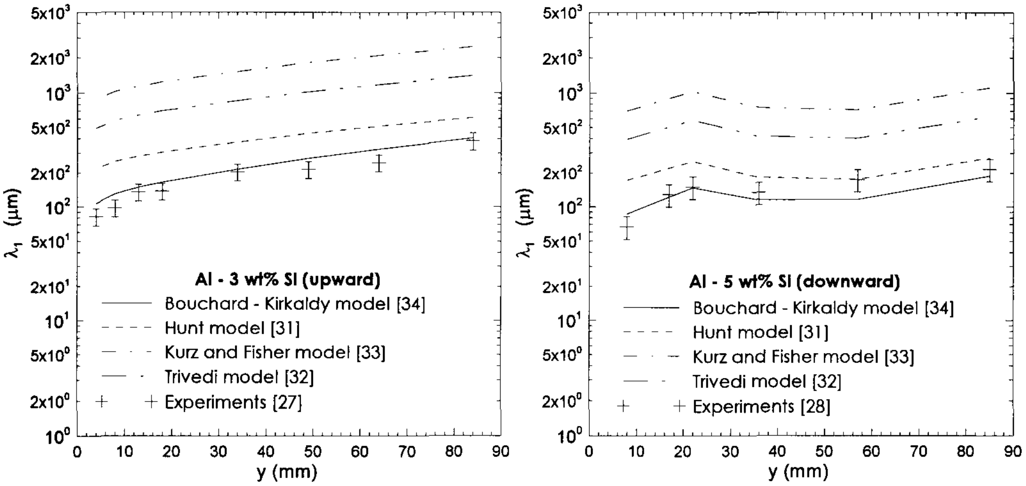

(a) (b)

Figure 4: Primary arm spacing distribution in the domain at r=0 and various locations of y in a uni-directional solidification process. (a) upward solidification showing that simulations carried out with the Bouchard-Kirkaldy model[34] has good agreement with the experiment results[27], and (b) downward solidification showing that simulations carried out with the Bouchard-Kirkaldy[34] model coupled with the Lehmann model[35] has good agreement with the experiment results[28].

Velocity boundary conditions

Figure 5 shows a schematic of the velocity boundary conditions used in both the upward solidification mode (Figure 5(a)) and downward solidification mode (Figure 5(b)).

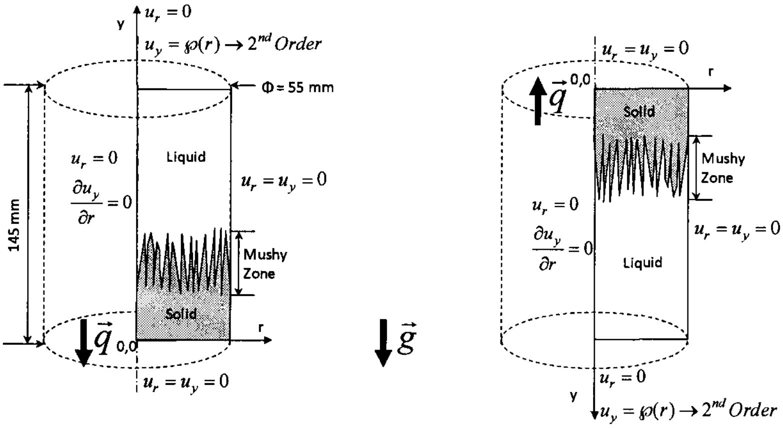

(a) (b)

Figure 5: Velocity boundary conditions for (a) upward solidification, (b) downward solidification.

The critical boundary condition that was determined by further simulations was the velocity, u_y at feeding end of the cavity (y = H). In laboratory experiments on directional solidification, the mass of solidifying material remains constant at all times. However, in downward solidification simulations, this condition cannot be maintained because of the inherent complexities arising from the formation of shrinkage voids which will introduce a third phase in air apart from the two already existing phases in liquid and solid. Hence, in downward solidification simulation, fresh liquid was introduced at the boundary defined by y = H with a parabolic velocity profile to avoid the formation of the third phase; air. In upward solidification simulation, the mass of the solidifying material can be maintained as constant at all times since the gravity vector will assist the liquid to fill the shrinkage voids formed during solidification and prevent the formation of any air as third phase. However, fresh liquid was introduced continuously at the boundary defined by y=H in upward solidification as well because there was insignificant difference between maintaining a constant mass of the solidifying materials and introducing fresh liquid at all times. This was elaborated by simulating four specific conditions for the velocity at the boundary defined by y=H, as defined below:

1. Constant velocity of u_y at top wall(feeding boundary), with domain reducing due to shrinkage [36].
2. Constant velocity profile of $u_y(r)$ at top wall, without domain reducing [14, 15].
3. Parabolic velocity profile of $u_y(r)$ at top wall, with domain reducing [37, 38].
4. Parabolic velocity profile of $u_y(r)$ at top wall, without domain reducing [39]

Figure 6 presents the results of the above-mentioned four simulation conditions. It can be observed that there is insignificant difference in the resultant solidification times for the four boundary conditions (maximum deviation ~ 1.7 s or 2.8%). This shows that any of the four conditions can be used to simulate the directional solidified experiments for validation of the simulation results. Further, the same logic was applied to the downward solidification mode as well to justify that the use of liquid flow with parabolic velocity profile at the boundary defined by y=H to reproduce the experiment conditions.

In all our solidification simulations the boundary conditions at y = H was defined by Equation (1)

$$u_y(r) = u_{\max}\left\{1 - \left(\frac{r}{Ri}\right)^2\right\} \tag{1}$$

where Ri is radius as shown in Figure 3; u_{max} is the maximum velocity located at r = 0. The integration of $u_y(r)$ in the boundary area yields the Volume Flow Rate (VFR) due to shrinkage at each time step and is presented in Equation (2).

$$VFR = \int_0^H \int_0^{Ri} 2\pi \cdot r \left\{ \frac{1}{r} \frac{\partial (r u_r)}{\partial r} + \frac{\partial u_y}{\partial y} \right\} \cdot dr \cdot dy \qquad (2)$$

VFR from Equation (2) can be used to evaluate u_{max} at each time step by using Equation (3).

$$VFR = \int_0^{Ri} u_y(r) \cdot 2\pi \cdot r \cdot dr = \int_0^{Ri} u_{\max} \left\{ 1 - \left(\frac{r}{Ri} \right)^2 \right\} \cdot dr \qquad (3)$$

where H is the height of cavity and u_r is velocity in r.

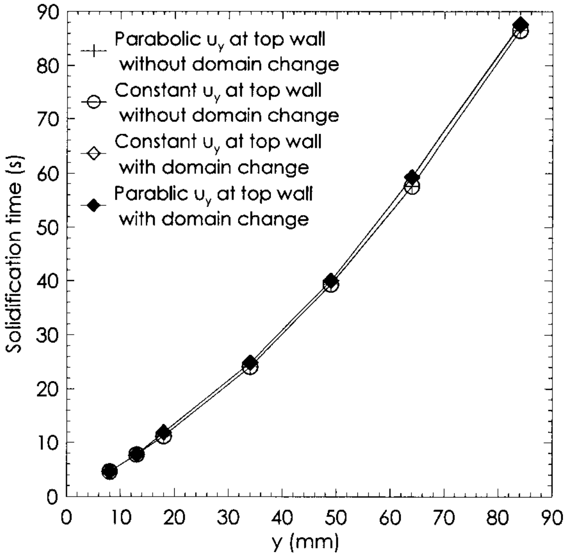

Figure 6: Solidification time (at interface of mushy zone/liquid) for four assumptions of velocity boundary at top wall of Al-3wt%si upward solidification.

AUTHOR'S CONTRIBUTION TO PUBLICATIONS

All the five papers were written by the author and the two co-supervisors. The following are the contributions by author in all five papers:

- Conceive, design, develop, implement and validate the algorithms, numerical procedure, simulation experiments, analysis of results and all the manuscripts for publications.
- Write the discussions for the observed results.
- Derive and write the conclusions.

MAIN CONTRIBUTIONS OF RESEARCH

- Developed a Fortran code to simulate 2-D and unsteady solidification problems for hypoeutectic Al-Si alloys inside a cylindrical container by solving momentum, continuity, energy and concentration equations.
- Solved instability problem due to source term inside energy equation to reduce computing time by up to 50% (Publication A).
- Developed an innovative numerical technique and algorithm to include undercooling in the liquid at the mushy zone/liquid interface during solidification (Publication A).
- Investigated the effect of undercooling in the liquid at the mushy zone/liquid interface on solidification time, and primary arm spacing (Publications A and B).
- Carried out a macro-scale simulation combined with a micro-scale evaluation to investigate and validate numerical results for the transient value of primary dendrite arm spacing during solidification (Publications A and B).
- Optimized the thermo-physical properties of material and phases to be used during solidification simulation of hypoeutectic Al-Si alloys (Publication C).
- Evaluated and quantified the effect of fluid flow caused by solidification shrinkage on the various solidification parameters and primary dendrite arm spacing (Publication D).
- Quantified the critical interaction between the magnitude and type of fluid flow and primary dendrite arm spacing during directional solidification (Publication E).

This dissertation is a compilation of the five journal publications were written from the results of this study: *Publications A to E*. In each of the publications, specific topics related to the study are analyzed and discussed along with extensive background prior art information on the respective topics of the publications.

DETAILS OF THE PUBLICATIONS

Publication A

Title	Solidification of Al-Si Alloys with Dendrtie Tip Undercooling Part 1: Transient Temperature Distribution and Solidification Time
Authors	Hongda Wang, Mohamed S. Hamed, Sumanth Shankar
Journal	Acta Materialia (Submitted in April, 2009)
Objectives	• Developed a more efficient algorithm. • Developed a new numerical method to consider undercooling of the liquidus temperature during binary alloy solidification.
Details	• Validated new algorithm by transient temperature distribution and solidification time. • Investigated the effect of undercooling on solidification time.
Conclusions	• A new and more efficient algorithm for solidification simulation of binary alloys has been proposed and validated. The present algorithm treated the strong non-linearity caused by the phase transformation term in the energy equation by solving the concentration equation before solving the energy equation. Further, the energy equation was wholly used instead of the concentration equation to evaluate the liquid fraction inside the mushy zone. • The transient temperature distribution in liquid, mushy zone and solid regions and solidification times have been validated by experiments. • The effect of undercooling of the liquidus temperature prior to the solidification event has been successfully quantified. Simulations with the effect of undercooling are far more agreeable with the experiment results for solidification times than those without.

Publication B

Title	Solidification of Al-Si Alloys with Dendrtie Tip Undercooling Part 2: Solidification Parameters
Authors	Hongda Wang, Mohamed S. Hamed, Sumanth Shankar
Journal	Acta Materialia (Submitted in April, 2009)
Objectives	• Investigated the effect of undercooling on fluid flow. • Investigated the effect undercooling on other solidification parameters such as temperature gradient, velocity of mushy zone/liquid interface and primary dendrite arm spacing during solidification. • Validate predicted primary arm spacing by experiments.
Details	• Investigated the effect of undercooling on fluid flow. • Investigated the effect undercooling on temperature gradient in liquid at the mushy zone/liquid interface. • Investigated the effect of undercooling on velocity of liquid-solid interface. • Investigated the effect of undercooling on primary dendrite arm spacing.
Conclusions	• The effect of undercooling, ΔT has a significant effect on the velocity of the fluid flow in the downward solidification and there is no significant effect in the upward solidification mode. • The effect of ΔT is pronounced on the distribution of the temperature gradient of the liquid at mushy zone/liquid interface, G in the computing domain during both upward and downward solidification modes. • The effect of ΔT is pronounced on the distribution of the velocity of the mushy zone/liquid interface, R in the computing domain during both upward and downward solidification modes. • The effect of ΔT is pronounced on the primary dendrite arm spacing in the downward solidification mode but not significant in the upward solidification mode. • There are three distinct regions in the downward solidification mode because of significant changes in the velocity of the fluid flow in the computing domain in these regions.

Publication C

Title	Optimization of Material Properties in Solidification Simulation of Binary Al-Si Alloy
Authors	Hongda Wang, Sumanth Shankar, Mohamed S. Hamed
Journal	Metallurgical and Materials Transactions A (Submitted in April, 2009)
Objectives	Investigated the effect of thermo-physical material properties on solidification parameters
Details	• Investigated the effect of thermal conductivity of solid on transient temperature distribution and solidification time. • Investigated the effect of specific heat of solid on transient temperature distribution and solidification time. • Investigated the effect of density of solid on solidification time. • Investigated the effect of diffusivity of solute in liquid on solidification time.
Conclusions	• For the solidification simulation of Al-3wt%Si alloy, all material properties of the liquid phase and the density of the solid phase can be assumed constant, however, the thermal conductivity and specific heat capacity of the solid phase will have to be considered as a function of temperature. • The thermo-physical material properties of the liquid and solid phases can be assumed to be constant for the solidification simulation of binary Al-Si alloys if the variation between the maximum and minimum values of each property is less than 5%. If the variation is greater than 5%, it is best if the properties were assumed as a function of temperature. • Diffusivity of solute in liquid has a marginal effect on solidification time when undercooling was considered. • The effect of undercooling of liquidus temperature prior to the solidification event of the primary phase should be considered during solidification simulation of binary alloys.

Publication D

Title	Effect of Shrinkage on Primary Dendrite Arm Spacing during Binary Al-Si Alloy Solidification
Authors	Hongda Wang, Sumanth Shankar, Mohamed S. Hamed
Journal	Metallurgical and Materials Transactions A (Submitted in April, 2009)
Objectives	• Investigated the effect of shrinkage on solidification parameters and primary dendrite arm spacing for both upward and downward solidification.
Details	• Investigated the effect of shrinkage on fluid flow for downward solidification. • Investigated the effect of shrinkage on velocity of mushy zone/liquid interface for both upward and downward solidification. • Investigated the effect of shrinkage on temperature gradient of liquid at mushy zone/liquid interface for both upward and downward solidification. • Investigated the effect of shrinkage on primary arm spacing for both upward and downward solidification.
Conclusions	• Considering the effect of shrinkage in the downward solidification increases the magnitude of the velocity of fluid flow and reverses the direction of flow. • Shrinkage decreases mushy zone/liquid interface velocity for both upward and downward solidification. • Shrinkage had little effect on the temperature gradient of liquid at the mushy zone/liquid interface in the upward solidification mode and had a significant effect on the same in the downward solidification mode. • The effect of shrinkage during solidification is not important to be considered for the estimation of primary arm spacing during simulation of upward solidification process wherein the velocity of the mushy zone/liquid interface is against the direction of the gravity vector. • However, it is critical to consider the effect of shrinkage during numerical simulation of downward and horizontal solidification process for the estimation of primary arm spacing, wherein the effect of density gradient in the liquid phase induces natural convection phenomenon causing strong fluid flow fields in the solidifying domain.

Publication E

Title	Interaction between Primary Dendrite Arm Spacing and Velocity of Fluid Flow during Solidification of Binary Al-Si Alloys
Authors	Hongda Wang, Mohamed S. Hamed, Sumanth Shankar
Journal	Acta Materialia (Submitted in April, 2009)
Objectives	Investigated the interaction effect between primary dendrite arm spacing and fluid velocity during upward and downward solidification.
Details	• Determined the optimized model for the estimation of primary arm spacing. • Investigated effect of changing primary dendrite arm spacing on fluid flow. • Investigated effect of fluid flow on primary dendrite arm spacing.
Conclusions	• In both the upward and downward solidification modes, the Bouchard-Kirkaldy model coupled with the Lehmann model to evaluate the primary arm spacing in a binary Al-Si hypoeutectic alloy is found to be the best among the various models available in the literature such as the Hunt, Trivedi and Kurz-Fisher models. • The use of any constant value of the primary arm spacing in the range of 100 to 450 μm do not create an appreciable change in the fluid flow field and velocity in the domain during the upward solidification mode. In the downward solidification domain the use of any constant value of the primary arm spacing in the range of 100 to 450 μm only causes a marginal change in the fluid velocity. Hence, the estimation of fluid flow field and velocity by an approximate value of λ_1 is acceptable. • While evaluating the primary arm spacing in the downward and horizontal solidification modes (presence of strong fluid flow caused by natural convection), the effect of instantaneous fluid velocity in the domain should be considered (using the Bouchard-Kirkaldy model coupled with the Lehmann model) to achieve a valid prediction of the primary dendrite arm spacing. The estimation of primary arm spacing without the effect of fluid velocity in the solidifying domain is erroneous. • In downward solidification mode, there are three regions of solidification. The fluid flow in region one is dominated by solidification shrinkage followed by the emergence of stronger flow due to natural convection in region two and finally the stabilization of flow due to natural convection.

From the conclusion of the five publications mentioned in the this section, it is evident that the new algorithm and numerical approach presented herein is more effective than the conventional ones in saving nearly half the computing cost and incorporating the effect of undercooling of the liquidus temperature prior to solidification event of the primary phase during binary alloy uni-directional solidification simulation. Moreover, the algorithm and numerical procedure have been well validated by experiment results. The thermo-physical properties of the solid phase in such a simulation should be considered as a function of temperature and that of the liquid phase may be considered as an average constant. To achieve a valid solidification simulation with the new algorithm, the effect of solidification shrinkage, transient fluid flow in the domain, undercooling of liquidus temperature (Burden and Hunts model [29, 30]) and optimized thermo-physical properties should all be considered together and such a solidification simulation could predict valid primary dendrite arm spacing using the Bouchard-Kirkaldy model [34] coupled with the Lehmann model [35] and such a prediction can be validated by experiment results.

REFERENCES

[1] X. C. Sha, D. Z. Li, Y. T. Zhang, X. G. Zhang, and Y. Y. Li, "Modelling effect of hot rolling process variables on microstructure and mechanical properties of low carbon strip steels," *Ironmaking and Steelmaking*, vol. 31, pp. 169-175, 2004.

[2] I. Johansen and H. J. Roven, "Mechanical properties of a rapidly solidified Al-Si-Ni-Mn alloy " *Materials Science & Engineering A (Structural Materials: Properties, Microstructure and Processing)*, vol. A179-A180, pp. 605-608, 1994.

[3] W. R. Osorio, C. A. Santos, J. M. V. Quaresma, and A. Garcia, "Mechanical properties as a function of thermal parameters and microstructure of Zn-Al castings," *Journal of Materials Processing Technology*, vol. 143-144, pp. 703-709, 2003.

[4] P. R. Goulart, J. E. Spinelli, W. R. Os'orio, and A. Garcia, "Mechanical properties as a function of microstructure and solidification thermal variables of Al-Si castings," *Materials Science and Engineering A*, vol. 421, pp. 245-253, 2006.

[5] S. G. Shabestari and F. Shahri, "Influence of modification, solidification conditions and heat treatment on the microstructure and mechanical properties of A356 aluminum alloy," *Journal of Materials Science Letters*, vol. 39, pp. 2023-2032, 2004.

[6] W. R. Osorio, P. R. Goulart, G. A. Santos, C. M. Neto, and A. Garcia, "Effect of dendritic arm spacing on mechanical properties and corrosion resistance of Al 9 wt pct Si and Zn 27 wt pct Al alloys," *Metallurgical and Materials Transactions A: Physical Metallurgy and Materials Science*, vol. 37, pp. 2525-2538, 2006.

[7] S. G. Shabestari and H. Moemeni, "Effect of copper and solidification conditions on the microstructure and mechanical properties of Al-Si-Mg alloys " *Journal of Materials Processing Technology - Proceedings of the International Conference in Advances*, vol.

153-154, pp. 193-198, 2004.

[8] J. M. V. Quaresma, C. A. Santos, and A. Garcia, "Correlation between unsteady-state solidification conditions, dendrite spacings, and mechanical properties of Al-Cu alloys," *Metallurgical and Materials Transactions A: Physical Metallurgy and Materials Science*, vol. 31, pp. 3167-3178, 2000.

[9] W. D. Bennon and F. P. Incropera, "A continuum model for momentum, heat and species transport in binary solid – liquid phase change systems - I. Model formulation," *International Journal of Heat and Mass Transfer*, vol. 30, pp. 2161-2170, 1987.

[10] W. D. Bennon and F. P. Incropera, "A continuum model for momentum, heat and species transport in binary solid – liquid phase change systems - II. Application to solidification in a rectangular cavity," *International Journal of Heat and Mass Transfer*, vol. 30, pp. 2171-2178, October 1987.

[11] W. D. Bennon and F. P. Incropera, "Numerical analysis of binary solid – liquid phase change using a continuum model," *Numerical Heat Transfer*, vol. 13, pp. 277-296, 1988.

[12] S. D. Felicelli, J. C. Heinrich, and D. R. Poirier, "Simulation of freckles during vertical solidification of binary alloys," *Metallurgical Transactions B (Process Metallurgy)*, vol. 22, pp. 847-859, Dec. 1991.

[13] S. D. Felicelli, J. C. Heinrich, and D. R. Poirier, "Numerical models for dendritic solidification of binary alloys," *Numerical Heat Transfer, Part B: Fundamentals*, vol. 23, pp. 461-481, 1993.

[14] J. C. Heinrich and D. R. Poirier, "The effect of volume change during directional solidification of binary alloys," *Modeling and Simulation in Materials Science and Engineering*, vol. 12, pp. 881-899, Sep. 2004.

[15] E. McBride, J. C. Heinrich, and D. R. Poirier, "Numerical simulation of incompressible flow driven by density variations during phase change," *International Journal for Numerical Methods in Fluids*, vol. 31, pp. 787-800, Nov. 1999.

[16] V. R. Voller and C. Prakash, "Fixed grid numerical modeling methodology for convection - diffusion mushy region phase – change problems," *International Journal of Heat and Mass Transfer*, vol. 30, pp. 1709-1719, 1987.

[17] H. Wang, S. Shankar, and M. S. Hamed, "Numerical model for binary alloy solidification," in *5th International Conference on Computational Heat and Mass Transfer*, Canmore, Canada, 2007, pp. 345-351.

[18] D. Xu and Q. Li, "Gravity- and solidification-shrinkage-induced liquid flow in a horizontally solidified alloy ingot," *Numerical Heat Transfer: An International Journal of Computation and Methodology*, vol. Part A: Applications, 20, pp. 203-221, 1991.

[19] L. S. Yao, "Natural convection effects in the continuous casting of a horizontal cylinder," *International Journal of Heat and Mass Transfer*, vol. 27, pp. 697-704, 1984.

[20] J. C. Ramirez, C. Beckermann, A. Karma, and H.-J. Diepers, "Phase-field modeling of binary alloy solidification with coupled heat and solute diffusion," *Physical Review E*, vol. 69, pp. 051607-1-051607-16, May 2004.

[21] J. A. Warren, W. J. Boettinger, C. Beckermann, and A. Karma, "Phase-field simulation of solidification," *Annual Review of Materials Science*, vol. 32, pp. 163-194, 2002.

[22] C. Beckermann, Q. Li, and X. Tong, "Microstructure evolution in equiaxed dendritic growth," *Science and Technology of Advanced Materials*, vol. 2, pp. 117-126, 2001.

[23] K. R. Elder, M. Grant, N. Provatas, and J. M. Kosterlitz, "Sharp interface limits of phase-field models," *Physical Review E (Statistical, Nonlinear, and Soft Matter Physics)*, vol. 64, pp. 021604/1-021604/18, Aug. 2001.

[24] N. Provatas, N. Goldenfeld, and J. Dantzig, "Modeling solidification using a phase-field model and adaptive mesh refinement," *Solidification 1999. Proceedings*, pp. 151-160, 1999.

[25] A. Karma and W.-J. Rappel, "Phase-field method for computationally efficient modeling of solidification with arbitrary interface kinetics," *Physical Review E (Statistical Physics, Plasmas, Fluids, and Related Interdisciplinary Topics)*, vol. 53, pp. R3017-R3020, 1996.

[26] M. C. Flemings, *Solidification processing*. New York, NY.: McGraw-hill Book Co., 1974.

[27] M. D. Peres, C. A. Siqueira, and A. Garcia, "Macrostructural and microstructural development in Al-Si alloys directionally solidified under unsteady-state conditions," *Journal of Alloys and Compounds*, vol. 381, pp. 168-181, November 3 2004.

[28] J. E. Spinelli, M. D. Peres, and A. Garcia, "Thermosolutal convective effects on dendritic array spacings in downward transient directional solidification of Al-Si alloys," *Journal of Alloys and Compounds*, vol. 403, pp. 228-238, Novermber 2005.

[29] M. H. Burden and J. D. Hunt, "Cellular and dendritic growth. I," *Journal of Crystal Growth*, vol. 22, pp. 99-108, 1974.

[30] M. H. Burden and J. D. Hunt, "Cellular and dendritic growth. II," *Journal of Crystal Growth*, vol. 22, pp. 109-116, 1974.

[31] J. D. Hunt, "Solidification and casting of metals," *Proceedings of the International Conference on Solidification and Casting of Metals, The Metals Society, London*, pp. 3-9, 1979.

[32] R. Trivedi, "Interdendritic spacing: part II. A. comparison of theory and experiment," *Metallurgical Transactions A (Physical Metallurgy and Materials Science)*, vol. 15A, pp. 977-982, 1984.

[33] W. Kurz and D. J. Fisher, "Dendritic growth and limit of stability tip radius and spacing," *Acta Metall.*, vol. 29, pp. 11-20, 1981.

[34] D. Bouchard and J. S. Kirkaldy, "Prediction of dendrite arm spacings in unsteady- and steady-state heat flow of unidirectionally solidified binary alloys," *Metallurgical and Materials Transactions B (Process Metallurgy and Materials Processing Science)*, vol. 28B, pp. 651-663, Aug. 1997.

[35] P. Lehmann, R. Moreaub, D. Camela, and R. Bolcatob, "A simple analysis of the effect of convection on the structure of the mushy zone in the case of horizontal Bridgman solidification. Comparison with experimental results," *Journal of Crystal Growth*, vol. 183,

pp. 690-704, 1998.

[36] D. Samanta and N. Zabaras, "Modelling convection in solidification processes using stabilized finite element techniques," *International Journal for Numerical Methods in Engineering*, vol. 64, pp. 1769-1799, 2005.

[37] K. C. Chiang and H. L. Tsai, "Shrinkage-induced fluid flow and domain change in two-dimensional alloy solidification," *International Journal of Heat and Mass Transfer*, vol. 35, pp. 1763-1770, 1992.

[38] K. C. Chiang and H. L. Tsai, "Interaction between shrinkage-induced fluid flow and natural convection during alloy solidification," *International Journal of Heat and Mass Transfer*, vol. 35, pp. 1771-1778, 1992.

[39] M. J. M. Krane and F. P. Incropera, "Analysis of the effect of shrinkage on macrosegregation in alloy solidification," *Transport Phenomena in Solidification ASME HTD*, vol. vol 284, pp. 13-27, 1994.

SOLIDIFICATION OF Al-Si ALLOYS WITH DENDRITE TIP UNDERCOOLING
PART 1: TRANSIENT TEMPERATURE DISTRIBUTION AND SOLIDIFICATION TIME

Hongda Wang[1,2], Mohamed S. Hamed[1], Sumanth Shankar[2,*]
[1]Thermal Processing Laboratory (TPL)
[2]Light Metal Casting Research Centre (LMCRC)
McMaster University, Hamilton, ON, Canada L8S 4L7

ABSTRACT

This is Part 1 of the two-part publication wherein a novel solution approach for the numerical simulation of the solidification process of binary Al-Si hypoeutectic alloys during upward and downward solidification modes is presented. The aim of this work is to elaborate the effect of considering temperature undercooling of the liquid ahead of the dendrite tip during solidification. Undercooling is always observed during solidification but the phenomenon could not be considered in simulation processes because of the present day numerical solution procedures adopted. In the new approach presented herein, the temperature distribution in the mushy zone was used to define the fraction of solid, which enabled the evaluation of the effect of dendrite tip temperature undercooling on the characteristics of the binary alloy solidification. The present numerical algorithm was found to significantly reduce the computation time. The momentum, continuity, energy and concentration equations were solved using finite-volume method. The momentum and continuity equations were coupled by the SIMPLE algorithm. The temperature and the liquid concentration inside the mushy zone were coupled by using the local equilibrium assumptions. Transient temperature distribution and solidification time from the numerical analysis, with consideration of natural convection due to temperature and concentration gradients, had been successfully simulated and validated with experiment results from binary alloy solidification of Al-Si hypoeutectic alloys. Numerical results with consideration of dendrite tip temperature undercooling were found to have better agreement with experimental works.

NOMENCLATURE

c_{ps}	Specific heat of solid as a function of temperature (J Kg^{-1} K^{-1}) [1];
c_{pl}	Specific heat of liquid (J Kg^{-1} K^{-1}) [1];
C_L	Liquid concentration (wt%);
C_o	Average alloy composition (wt%);
C_S	Solid concentration (wt%);
D	Solute diffusivity coefficient of liquid (6.25 x 10^{-9} (m^2 s^{-1})) [2];
G	Temperature gradient in liquid at the mushy zone/liquid interface (°C mm^{-1});
k	Average partition coefficient (0.116) [3];

---

[*] Corresponding Author: shankar@mcmaster.ca , voice: (905) 512-1324

K_s	Thermal conductivity of solid as a function of temperature (W m^{-1} K^{-1}) [1];
K_l	Thermal conductivity of liquid (W m^{-1} K^{-1}) [1];
L	Latent heat of fusion (J Kg^{-1}) [3];
m	The slope of liquidus line (– 6.675 (K $wt\%^{-1}$)) [3];
p	Pressure(Pa);
R	Velocity of mushy zone/liquid interface (mm s^{-1});
t	Time (s);
T	Temperature (°C);
T_{liq}	Liquidus temperature (°C) [3];
T_{ini}	Initial temperature of liquid (°C);
T_m	Melting temperature of pure aluminum (660 °C) [3];
T_{eut}	Eutectic temperature (578.6 °C) [3];
$\dot{T}$	Instantaneous tip cooling rate = G×R (°C s^{-1});
ΔT	Undercooling of T_{liq} (°C);
U_r	Velocity in r direction (mm.s^{-1});
U_y	Velocity in y direction (mm.s^{-1});
U	Flow velocity in the liquid of mushy zone/liquid interface (mm.s^{-1});
β	Contraction ratio $\left[\beta = \frac{\rho_s - \rho_l}{\rho_l}\right]$ (volumetric shrinkage during solidification) [1];
β_C	Solute expansion coefficient (-4.26×10^{-4} (K^{-1})) [1];
β_T	Thermal expansion coefficient (1.39×10^{-4} (K^{-1})) [1];
Γ	Gibbs-Thomson coefficient (1.97×10^{-7} (K m^{-1})) [4];
ϕ	Liquid fraction;
ρ_l	Liquid density (Kg m^{-3}) [1];
ρ_s	Solid density (Kg m^{-3}) [1];
μ	Dynamic viscosity 1.3×10^{-3} (Pa s) [1];
λ_1^0	Primary arm spacing if no fluid flow effect is considered (μm);
λ_1	Primary arm spacing (μm);

THERMO-PHYSICAL MATERIAL PROPERTIES

Properties	**Al-3wt%Si**	**Al-5wt%Si**	**Al-7wt%Si**
K_s	228.08 – 0.061055×T	226.01-0.077488×T	223.93-0.093920×T
K_l	85.476	84.568	83.661
C_{ps}	887.23+0.50227×T	883.54+0.50227×T	879.85+0.50227×T
C_{pl}	1168.9	1163.7	1158.6
ρ_s	2627.9	2621.6	2614.5
ρ_l	2415.0	2422.8	2430.6
L	4.05×10^5	4.25×10^5	4.45×10^5

INTRODUCTION

Solidification is the phenomenon of phase transformation from liquid phase to solid phase. Solidification mechanisms for pure metals and alloys are different from each other. Solidification for pure metals is mainly dominated by heat transfer conditions [5-7]. However, both heat and mass transfer conditions affect the solidification of metallic alloys. During solidification of binary alloys, there are three distinct zones, namely, the liquid, solid and the intermediate two phase (solid and liquid) region termed the mushy zone [8]. During the past few decades, there have been several attempts to simulate solidification of binary alloys [5, 7, 9-17]. These simulation attempts can be broadly classified into three categories:

- Solution to energy equation (thermal profiles) alone [17, 18].
- Solution to both energy equation and concentration equation (solute concentration profiles) with the assumption of equilibrium solidification conditions, and using the Lever rule and/or Scheil equation [8] to evaluate the liquid fraction ϕ in the mushy zone [9, 11].
- Solution to both energy and concentration equations (solute concentration profiles) with the assumption of equilibrium solidification condition and evaluate ϕ from the governing equations without lever rule or Scheil equation assumptions [12, 13, 15, 19].

Although, the third approach is the most recent and advanced among the above mentioned techniques, none of them could completely validate their numerical simulations with experiment results, such as transient temperature distribution and solidification time, because all these techniques have unique approaches to couple and solve the energy and concentration equations (to determine liquid fraction in the mushy zone) and each of these approaches have made certain statements to avoid the instability problem caused by the strong non-linearity introduced by the phase transformation term in the energy equation. Some of the common assumptions include linear variation of temperature with ϕ [17] and absence of undercooling temperature [8] of the dendrite tip temperature.

Undercooling of the temperature at the dendrite tip can be caused by three factors: *kinetics of solidification, rate solute diffusion in liquid, and radius of the dendrite tip* [8]. If the effect of undercooling of the dendrite tip temperature was considered, the temperature and solute concentration gradients ahead of the dendrite tip would be higher because the temperature of liquid/mushy zone interface would be lower than the T_{liq}. Hence, assuming no undercooling of the temperature of dendrite tip will lead to erroneous evaluation of the dendrite arm spacing in the microstructure [20-23].

Undercooling can be considered in solidification simulation of binary alloys only if the energy equation is directly applied to determine ϕ. In present work, a new approach to numerically simulate binary alloy solidification considering the effect of temperature undercooling at dendrite tip has been proposed wherein the energy equation alone is used to evaluate ϕ and a new coupling scheme for T and C_L inside the mushy zone has been utilized to avoid instability problems in the energy equation caused by the phase transformation term.

BACKGROUND

Typically, during dendritic solidification in the mushy zone of a binary alloy, the interface temperature of the dendrite tip and the liquid will require an undercooling from the T_{liq} to sustain growth [8]. ΔT depends on G, R, Γ, k, D, m and C_o.

Burden et al [24, 25] presented an expression for ΔT as given in Equation (1). The magnitude of ΔT in Equation (1) was validated by experiments for cooling rates ranged up to 3 °C/s [24, 25]. The magnitude of undercooling in the present work is not a constant throughout the solidification process but is updated at every time step for each control volume (CV) in the domain.

$$\Delta T = (\frac{GD}{R}) + \frac{\left(-8mR(1-k)C_o\Gamma\right)^{\frac{1}{2}}}{D^{\frac{1}{2}}} \quad (1)$$

If numerical simulations do not consider ΔT, the estimation of G will be lower than the actual values in an experiment and this may lead to a prediction of shorter solidification times.

The early efforts to simulate binary alloy solidification by Voller et al [17] considered only the energy equation (enthalpy balance) wherein the instability problem caused by strong non-linearity introduced by the phase transformation term was alleviated by assuming the ϕ as a linear function of temperature inside the mushy zone. The algorithm was not validated with any experiments. Subsequently, Bennon et al [9, 11] proposed a numerical algorithm to simulate alloy solidification using one form of the concentration and energy equations in all three zones (solid, liquid and mushy). The volume fraction of liquid was evaluated by applying the lever rule according to the alloy phase diagram at each temperature. Contrary to reality, a complete diffusion of solute atoms in the solid phase was assumed. The ΔT value and the volumetric shrinkage (β) during phase transformation was not considered. No experimental validation of the algorithm was presented.

Felicelli et al [12] proposed a numerical algorithm for simulating solidification of binary alloys in which the energy and concentration equations were themselves used to evaluate liquid fraction ϕ in the mushy zone rather than the lever rule or Scheil equation [9, 11]. One form of concentration equation was used to define the solute concentration in the solid, mushy zone and liquid regions alike. One form of energy equation was used in the solid and liquid regions. However, in the mushy zone, a modified form of energy equation was used, wherein, the concentration equation was substituted into the phase transformation term in the energy equation to overcome the instability caused by the phase transformation term [9, 11]. The ϕ in the mushy zone was evaluated from the concentration equation until the liquid temperature reached the eutectic point. Subsequently, at the eutectic temperature, ϕ has to be evaluated by the energy equation. ΔT was not used in this algorithm because concentration equation was used to determine ϕ in the bulk of the mushy zone and if ΔT was considered at the dendrite tip, then the completion of the solidification simulation would be practically impossible due to the very small order of D ($\sim 10^{-9}$). An outline of the numerical algorithm used by Felicelli et al [12] is shown in Figure 1. This algorithm has been one of the most popular method this date to simulate binary alloy solidification [12-15]. This algorithm did not consider ΔT or β. However, McBride et al [15] further developed this algorithm by considering β and the fluid flow occurring as a result of volumetric shrinkage. Heinrich et al, [11] corrected the flow fields during solidification at eutectic temperatures. No experimental validation in transient temperature distribution or solidification time of these numerical simulations has been carried out.

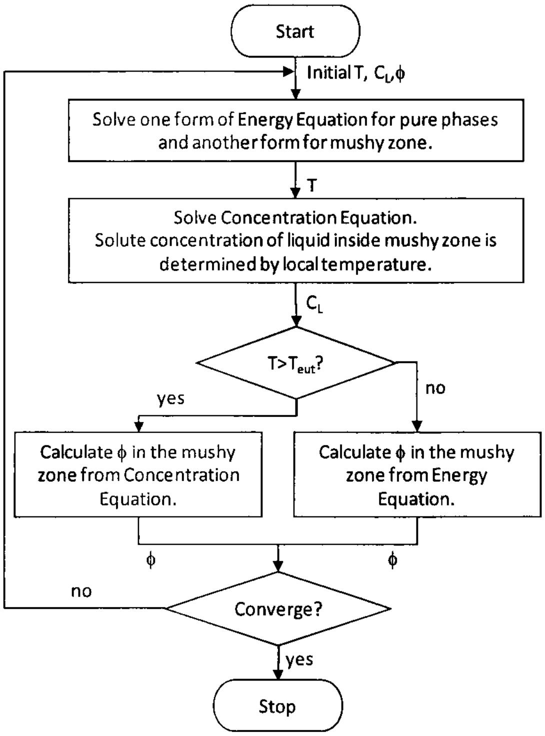

Figure 1: Flowchart of algorithm for binary alloy solidification proposed by Felicelli et al [12].

GOVERNING EQUATIONS

The governing equations for the simulation conditions shown in Figure 2 are presented in this section. The energy equation is presented in Equation (2) and the concentration equation in Equation (3).

$$\overbrace{\frac{\partial((\phi\rho_l c_{pl} + (1-\phi)\rho_s c_{ps})T)}{\partial t}}^{\text{Transient Term}} + \overbrace{\rho_l c_{pl} u_r \frac{\partial T}{\partial r} + \rho_l c_{pl} u_y \frac{\partial T}{\partial y}}^{\text{Convection Term}} + \overbrace{\rho_s L \frac{\partial \phi}{\partial t}}^{\text{Phase Transformation Term}}$$

$$= \underbrace{\frac{1}{r}\frac{\partial}{\partial r}(r(\phi K_l + (1-\phi)K_s)\frac{\partial T}{\partial r}) + \frac{\partial}{\partial y}((\phi K_l + (1-\phi)K_s)\frac{\partial T}{\partial y})}_{\text{Diffusion Term}} \tag{2}$$

$$\overbrace{\frac{\partial(\phi\rho_l C_L + (1-\phi)\rho_s C_S)}{\partial t}}^{\text{Transient Term}} + \overbrace{\rho_l u_r \frac{\partial C_L}{\partial r} + \rho_l u_y \frac{\partial C_L}{\partial y}}^{\text{Convection Terms}}$$

$$= -\rho_l[\underbrace{\beta C_L \frac{\partial \phi}{\partial t}}_{\substack{\text{Source Term} \\ \text{from Shrinkage}}} \underbrace{- D(\frac{1}{r}\frac{\partial}{\partial r}(\phi r \frac{\partial C_L}{\partial r})) - D\frac{\partial}{\partial y}(\phi \frac{\partial C_L}{\partial y})}_{\text{Diffusion Term}}] \tag{3}$$

Temperature of a CV in the mushy zone was determined by Equation (4) wherein local equilibrium conditions were assumed [8].

$$T = T_m + mC_L \tag{4}$$

If re-melting of solid does not occur, the average solute concentration of the solid phase in a CV was evaluated by Equation (5).

$$C_S = \frac{1}{1-\phi}\int_\phi^1 kC_L d\phi \tag{5}$$

Re-melting is the phenomenon that the already solidified solid phase is melted inside CV during solidification procedure. This may occur because the convective current with higher temperature is flowed into this CV. If re-melting of solid occurs, C_S must be taken from the history of C_S during solidification [12]. During solidification procedure as solid phase inside CV keeps on growing (no re-melting), the magnitude of C_S has to be recorded with the decreasing of ϕ from the first piece of solid at the beginning of solidification according to equation (5). As re-melting occurs, C_S need to be obtained from the recorded history according to the different ϕ instead of directly applying equation (5).
Mass conservation is presented in Equation (6).

$$\frac{1}{r}\frac{\partial(ru_r)}{\partial r} + \frac{\partial u_y}{\partial y} = \beta\frac{\partial \phi}{\partial t} \tag{6}$$

The momentum equations in the r and y directions as defined in Figure 2 are presented in Equations (7) and (8), respectively.

$$\rho_l \frac{\partial u_r}{\partial t} + \rho_l \frac{u_r}{\phi}\frac{\partial u_r}{\partial r} + \rho_l \frac{u_y}{\phi}\frac{\partial u_r}{\partial y} + \rho_l \frac{\beta}{\phi}\frac{\partial \phi}{\partial t} u_r$$

$$= -\phi \frac{\partial p}{\partial r} + \frac{1}{r}\frac{\partial (r 2\mu \frac{\partial u_r}{\partial r})}{\partial r} - \frac{2\mu u_r}{r^2} + \frac{\partial (\mu \frac{\partial u_y}{\partial r} + \mu \partial \frac{\partial u_r}{\partial y})}{\partial y} + \mu \frac{\beta}{3}\frac{\partial (\frac{\partial \phi}{\partial t})}{\partial r} - \frac{\mu \phi u_r}{k_n} \qquad (7)$$

$$\rho_l \frac{\partial u_y}{\partial t} + \rho_l \frac{u_r}{\phi}\frac{\partial u_y}{\partial r} + \rho_l \frac{u_y}{\phi}\frac{\partial u_y}{\partial y} + \rho_l \frac{\beta}{\phi}\frac{\partial \phi}{\partial t} u_y$$

$$= -\phi \frac{\partial p}{\partial y} + \frac{1}{r}\frac{\partial [r(\mu \frac{\partial u_y}{\partial r} + \mu \partial \frac{\partial u_r}{\partial y})]}{\partial r} + \frac{\partial (2\mu \frac{\partial u_y}{\partial y})}{\partial y} + \mu \frac{\beta}{3}\frac{\partial (\frac{\partial \phi}{\partial t})}{\partial y} - \frac{\mu \phi u_y}{k_p} + \rho_l^{*} \phi g_y \qquad (8)$$

Where ρ_l^{*} is applied with Boussinesq assumption: $\rho_l^{*} = \rho_l \left(\beta_T (T - T_{ini}) - \beta_c (C_L - C_o)\right)$

The undercooling can be estimated by the model presented in Burden et al [24, 25] and given in Equation (1) and shown below:

$$\Delta T = (\frac{GD}{R}) + \frac{\left(-8mR(1-k)C_o\Gamma\right)^{\frac{1}{2}}}{D^{\frac{1}{2}}} \qquad (1)$$

The magnitude of undercooling in the present work is not a constant throughout the solidification process but is updated at every time step for each control volume (CV) in the domain.

A simplified version of the Kozeny – Carman model [26, 27] was used to define the permeability of the mushy zone as a function of liquid fraction. Asai et al [28] proposed the simplified model shown in Equation (9). The morphology of the dendrites in Equation (9) is assumed to be conical with a large height to base diameter ratio and the magnitude of permeability in the direction normal to dendrite growth, K_n is identical to the parallel direction, K_p.

$$K_p = K_n = \frac{1}{5\left(\frac{6}{\lambda_1}\right)^2}\frac{\phi^3}{(1-\phi)^2} \qquad (9)$$

Bouchard et al [20] proposed an expression, presented in Equation (10), for the primary dendrite from both a theoretical and empirical assessments of unsteady solidification conditions. Lehmann et al [29] proposed a theoretical expression, presented in Equation (11), to evaluate primary dendrite arm spacing as a function of fluid flow velocity in the mushy zone.

$$\lambda_1^0 = a_1 \left(\frac{16 C_o^{\frac{1}{2}} G_o \varepsilon \Gamma D}{(1-k) m G R} \right)^{\frac{1}{2}} \tag{10}$$

$$\lambda_1 = \lambda_1^0 \left(1 + \frac{U}{R} \right)^{-\frac{1}{2}} \tag{11}$$

In Equation (10), $G_0\varepsilon$ is the characteristic parameter ($\approx$ 360 K.mm^{-1}) [20] and the constant a_1 = 250 [30] for the Al-Si hypoeutectic alloys.

DOMAIN DEFINITION

In this section the formulation, initial and the boundary conditions of the problem are presented for two different solidification conditions:

- *Upward Solidification* → heat extraction is in the same direction as gravity vector. Schematic and boundary conditions for C_L and T are shown in Figure 2(a). There is no natural convection of the liquid because the density gradient is positive in the direction of the gravity vector [31]. Thermal boundary condition for Al-5wt%Si at heat extracting side is: $h = 4500 \times t^{-0.09}$ (W m^{-2} K^{-1}) [18]. For Al-3wt%Si, thermal boundary condition at heat extracting side is defined as transient temperature distribution from correlation equation, equation (12), from experimental work Peres et al [18]:

$$\mathrm{f(t)} = \begin{cases} -12 \times \mathrm{t} + 644 \quad (\mathrm{t} \le 10\mathrm{s}) \\ 637.44 - 63.08 \times \ln(\mathrm{t}) + 198.96/\ln(\mathrm{t}) - 8.30 \times \ln(\mathrm{t})^2 - 115.26/\ln(\mathrm{t})^2 + 0.89 \times \ln(\mathrm{t})^3 \quad (\mathrm{t} > 10\mathrm{s}) \end{cases} \tag{12}$$

- *Downward Solidification* → heat extraction is in the opposite direction to gravity vector. Schematic and boundary conditions for C_L and T are shown in Figure 2(b). There is natural convection of the liquid phase because the density gradient is positive against the direction of the gravity vector [31]. Thermal boundary condition for Al-5wt%Si at heat extracting side is: h = 2400 (W m^{-2} K^{-1}) [30]. For Al-7wt%Si, thermal boundary condition at heat extracting side is defined as transient temperature distribution by the correlation equation, equation (13), from experimental work Spinelli et al [30]:

$$\begin{aligned} \mathrm{f(t)} = {} & 620.35 - 9.89 \times \mathrm{t} + 9.32 \times 10^{-2} \times \mathrm{t}^2 + 4.00 \times 10^{-3} \times \mathrm{t}^3 - 1.60 \times 10^{-4} \times \mathrm{t}^4 + 2.68 \times 10^{-6} \times \mathrm{t}^5 - 2.50 \times 10^{-8} \times \mathrm{t}^6 \\ & + 1.43 \times 10^{-10} \times \mathrm{t}^7 - 4.90 \times 10^{-13} \times \mathrm{t}^8 + 9.10 \times 10^{-16} \times \mathrm{t}^9 - 7.20 \times 10^{-19} \times \mathrm{t}^{10} \end{aligned} \tag{13}$$

Boundary conditions for C_L at y = 0 in either upward or downward solidification is defined as equation (14):

$$C_L = \begin{cases} C_o & T > T_{liq} - \Delta T \\ g(\phi) & T = T_{liq} - \Delta T \quad g(\phi) \text{ defined by Equation (3)} \\ g(T) & T < T_{liq} - \Delta T \quad g(T) \text{ defined by Equation (4)} \end{cases} \tag{14}$$

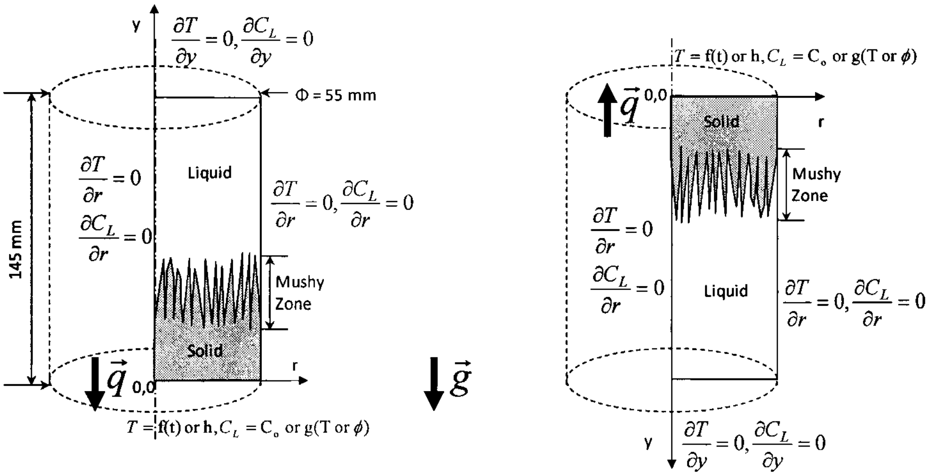

(a) (b)

Figure 2: Schematic and boundary conditions for C_L and T during the solidification simulations. (a) upward solidification and (b) downward solidification. The dimensions of the geometry are identical in (a) and (b).

Al – Si alloys melt with a marginal superheat temperature was considered inside a cylindrical geometry. All dimensions and boundary conditions used in the simulation were similar to those reported in the experimental study [18, 30]. Heat flux $\vec{q}$ in heat extracting boundary is getting smaller during solidification according to experiment conditions [18, 30] for both upward and downward cases. The simulation geometry is a cylinder with a diameter of 55 mm and height of 145 mm. As shown in Figure 2, the computational domain is a two dimensional cross-section of the geometry and owing to symmetry only one half of the cylinder was used in the simulation. Figure 2 also shows the directions of the heat flux (extraction), $\vec{q}$ and the gravity vector, $\vec{g}$.

The velocities at the boundaries of the computing domain presented in Figure 2 are shown in Figure 3. In Figure 3, the velocity, $u_y(r)$ at y = 145mm is adopted a second order (parabolic) function of r, as discussed in wang [32]. $u_y(r)$ is defined by equation (15):

$$u_y(r) = u_{\max}\left\{1 - \left(\frac{r}{R}\right)^2\right\} \tag{15}$$

where u_{max} is the maximum velocity at r = 0 and evaluated by the shrinkage observed during solidification. Volume flow rate (VFR) due to shrinkage at y = 145mm is calculated at each time step during simulation and is given in equation (16):

$$VFR = \int_0^H \int_0^{Ri} 2\pi \cdot r \left(\frac{1}{r}\frac{\partial (r u_r)}{\partial r} + \frac{\partial u_y}{\partial y} \right) \cdot dr \cdot dy \tag{16}$$

Ri and H are the radius and height of computing domain, respectively. With values of VFR after each time step, u_{max} could be evaluated and subsequently, the boundary condition could be determined at each time step.

The initial condition for velocity at t=0 for both the domains in Figure 3 is $u_r = u_y = 0$. The initial liquid temperature for upward solidification domain in Figure 3 (a) is 2 °C superheat above the liquidus temperature (644.0 °C for Al-3wt%Si, and 617.3 °C for Al-7wt%Si) and that for the downward solidification domain in Figure 3(b) is 5 °C superheat above the liquidus temperature (633.7 °C for Al-5wt%Si and 620.3 °C for Al-7wt%Si). Initial conditions for C_s, λ_1 and ϕ are: $C_s = C_o \times k$, $\lambda_1 = 300\mu m$ and $\phi = 1$, respectively.

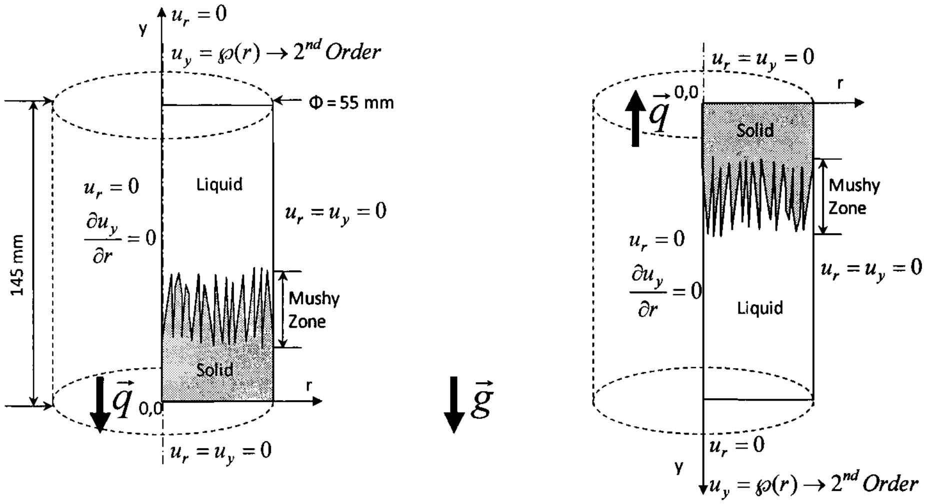

(a) (b)

Figure 3: Velocities at the boundaries of the computing domains presented in Figure 2. (a) upward solidification and (b) downward solidification.

The initial conditions for solute concentration for upward solidification were 3 wt% Si and 7 wt% Si and that for downward solidification simulations were 5 wt% Si and 7 wt% Si. The initial conditions for the temperature and solute concentration were identical to those reported in the experiment work [18, 30]. The material properties were obtained from two sources [1, 3] and presented in an earlier section of this manuscript, titled nomenclature.

NUMERICAL METHODS

Some important numerical methods related to these simulations will be introduced here. Numerical methods are discussed in following topics:

- Discretization schemes for transient, diffusion and convection terms
- Coupling scheme for momentum and continuity equations
- Grid dependence test
- Time step
- Convergence criteria

Discretization Method

Governing equations (2,3 and 6-8) were discretized by finite-volume method using a staggered grid [33]. One set of grid points was applied for T, C_L, p and the other set of grid points was used for u_r and u_y. Grid points with solid lines in Figure 4 are for T, C_L and p and those with dash lines are for u_r and u_y. Smaller letters (ip or jp) represent node numbers for u_r and u_y. Capital letters (IP or JP) represent node numbers for other parameters. Only nodes marked with vectors in r direction have a none zero value for u_r and only nodes marked with vectors in y direction have a none zero value for u_y. In the following discussion in this section, energy equation (Equation (2)) will be taken as an example for the discretization method.

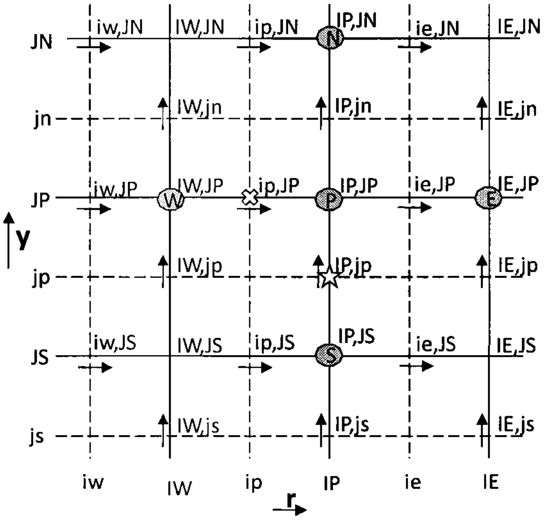

Figure 4: Staggered grid points distribution for two sets of parameters.

In order to enlarge the time step during simulation, implicit method was applied. In the energy equation, except that $\frac{\partial T}{\partial t}$ at the left side of the equation was discretized as $\frac{T_{IP,JP}^{new} - T_{IP,JP}^{old}}{t^{new} - t^{old}}$, all other temperatures in the equations were set as T^{new} for the simulation, where superscript 'new' means T at current time step and 'old' means T at previous time step.

Diffusion term was discretized by central difference scheme. For example, in energy equation, $\frac{\partial^2 T}{\partial y^2}$ was discretized as: $\frac{\frac{T_{IP,JN}-T_{IP,JP}}{y_{JN}-y_{JP}}-\frac{T_{IP,JP}-T_{IP,JS}}{y_{JP}-y_{JS}}}{y_{jn}-y_{jp}}$.

Hybrid difference scheme was applied for convection terms. In order to apply hybrid difference scheme, Pe number needed to be defined at all directions for each node for all velocity nodes. For example, to discretize term $\frac{\partial(u_y T)}{\partial y}$ by staggered grid with hybrid difference scheme, Pe number at north ($Pe_{IP,jn}$) and south ($Pe_{IP,jp}$) sides of node (IP,JP) need to be calculated. From staggered grid points shown in Figure 4, $Pe_{IP,jp}$ = $\frac{u_{y(IP,jp)}}{\frac{k_l}{\rho_l c_{PL}}/(y_{JP}-y_{JS})}$ and $Pe_{IP,jn}$ = $\frac{u_{y(IP,jn)}}{\frac{k_l}{\rho_l c_{PL}}/(y_{JN}-y_{JP})}$. Pe number is bond to -2 and 2 if it is smaller than -2 or greater than 2. $\frac{\partial(u_y T)}{\partial y}$, therefore, can be discretized by following equation:

$$[u_{y(IP,jn)}(\frac{1}{2}(1+\frac{1}{2}Pe_{IP,jn})T_{IP,JP}+\frac{1}{2}(1-\frac{1}{2}Pe_{IP,jn})T_{IP,JN})-u_{y(IP,jp)}(\frac{1}{2}(1+\frac{1}{2}Pe_{IP,jp})T_{IP,JS}+\frac{1}{2}(1-\frac{1}{2}Pe_{IP,jp})T_{IP,JP})]/(y_{jn}-y_{jp})$$

Coupling Scheme for the Momentum and the Continuity Equations

There are three unknowns (u_r, u_y and p) in the momentum and the continuity equations. The SIMPLE algorithm was applied to solve these parameters in following steps:

1. Momentum equations were solved for u_r and u_y by assuming certain (constant) pressure distribution.
2. Applied certain assumption (explained below) to achieve the relationship between correction of u_r, u_y and pressure correction.
3. Pressure correction was solved by being substituted into continuity equation.
4. This pressure correction then was applied to correct the assumed pressure distribution in step 1.
5. Corrected u_r and u_y by pressure correction based on the relationship assumed in step 2.

As step 1, and step 3 to step 5 were iterated, true distribution of u_r, u_y and p can be obtained. The main character of SIMPLE algorithm is based on the typical assumption made in step 2 for the relationship between correction of u_r, u_y and pressure correction. Detail of SIMPLE algorithm is described in Patankar [33].

Grid Dependence Test

The reason for grid dependence check is to solve the conflict by: 1. Larger mesh (finer grid size) will result in more accurate numerical results. 2. Larger mesh (finer grid size) will result in more computing time. The purpose to perform grid dependence check is to try to find a proper size of grid to achieve good accuracy of numerical simulation and minimize the computing time by applying mesh as small as possible (grid size as large as possible) during numerical simulations.

The method for grid dependence check is performed by setting an initial guessed grid size (coarse grid size = a) inside computing domain. After numerical results were achieved, finer grid size (=b, where a > b) needed to be applied to gain the other set of numerical results. If difference between these two sets of results is not small enough, the even finer grid size (= c, where a > b > c) is needed to be applied. For example, if difference between numerical results from grid size = c and those from grid size = b is small enough, mesh for grid size = b would be applied for future simulations. Simulations for Al-3wt%Si upward solidification is used here as an example to illustrate the grid depend check. Schmidt number was calculated and kept constant when grid was refined.

Table 1 shows the results for grid dependence check for Al-wt3%Si upward solidification. Three sizes of grid are tested. They are 116 × 23, 145 × 28 and 180 × 35, respectively. Average grid sizes for these meshes are 1.25mm × 1.20mm, 1.00mm × 0.98mm, 0.80mm × 0.79mm. Difference of grid size between Mesh A and Mesh B and between Mesh B and Mesh C is about 25%. Numerical results for solidification time at mushy zone/liquid interface, G, R and λ_1 are shown in

Table 1 for all three sizes of mesh. Difference of all these parameters calculated based on various grid sizes is also indicated. It shows that maximum variation of numerical results between Mesh A and Mesh B is about 11.6%. However, variation of results between Mesh B and Mesh C is less than 3.5%, which indicates Mesh B (145 × 28) is accurate enough for future calculation.

Time Step

The purpose of time dependence check is similar as grid dependence check. In order to reduce computing time for transient problems, time step length should be as large as possible. However, large time step length could result in either divergence of simulation or loss of detail of solidification procedure. In order to perform time dependence check, various time lengths (Δt_1, Δt_2, Δt_3) would be applied for the simulations. If numerical results calculated from Δt_1 were similar (variation was less than 2%) as those from Δt_2 ($\Delta t_2 = 0.5 \times \Delta t_1$) and Δt_1 could catch all required details of the solidification procedure. In addition, numerical results calculated from Δt_3 ($\Delta t_3 = 2 \times \Delta t_1$) were not similar (variation was greater than 2%) as those from Δt_1 or results from Δt_3 could not catch all required details of the solidification procedure, Δt_1 could be applied for future simulations.

Table 1: Mesh applied for numerical simulation in order to perform grid dependence check for Al-wt3%Si upward solidification.

Mesh/average grid size (mm×mm)	Location y(mm)	Solidification time(s) /Variation %	G(°C mm^{-1}) /Variation %	R(mm s^{-1}) /Variation %	λ_1(μm) /Variation %
116×23/ 1.25×1.20 (Mesh A)	49	39.22/0.5	0.1536/5.4	0.912/0.5	296.8/2.3
	34	23.99/0.7	0.2152/3.3	1.119/0.8	227.1/1.5
	18	11.05/1.5	0.3099/3.2	1.394/1.4	170.9/3.1
	13	7.571/2.1	0.3532/3.8	4.5/0.8	152.9/2.4
	8	4.409/2.9	0.4179/5.3	1.653/2.7	134.6/4.0
	4	2.197/2.9	0.6300/11.3	1.760/11.6	106.8/0.5
145×28/ 1.00×0.98 (Mesh B)	49	39.41/0.3	0.1623/3.1	0.907/0.6	290.2/0.9
	34	24.17/0.5	0.2226/3.1	1.111/0.6	223.6/0.5
	18	11.22/0.9	0.3201/2.3	1.413/0.9	164.9/1.5
	13	7.735/1.2	0.3671/2.5	1.512/0.7	149.3/1.7
	8	4.538/1.4	0.4415/3.0	1.699/1.8	129.5/2.6
	4	2.263/1.7	0.5663/3.1	1.990/3.1	106.2/3.4
180×35/ 0.80×0.79 (Mesh C)	49	39.53	0.1675	0.902	287.7
	34	24.23	0.2296	1.105	222.5
	18	11.32	0.3278	1.426	162.4
	13	7.830	0.3764	1.523	146.8
	8	4.603	0.4552	1.729	126.2
	4	2.302	0.5842	2.054	102.7

Convergence Criteria

The convergence criteria were applied to determine the convergence of the iteration for energy (T), concentration (C_L), momentum and continuity (u_r and u_y) equations. As the maximum variation of numerical results for these parameters in two successive iterations inside any time step was smaller than the magnitude of the convergent criteria, the convergence of respective equation was assumed to be achieved. Only numerical results come from the convergent simulations were valid and accurate. Proper convergent criteria were determined by the order of accuracy of the discretization method, grid size and the time length for each time step. For example, if one magnitude, say ξ, was determined as a critical error for the energy equation, the temperature at each time step was considered convergent if maximum difference between two successive iterations inside any time step was smaller than ξ. In order to confirm the reliability of ξ, another magnitude, $\sigma = 0.5 \times \xi$ was further applied as a critical error. If results from ξ were similar as those from σ (variation of less than 2%), applying ξ as critical error, therefore, was safe for the simulations.

NUMERICAL SIMULATION PROCEDURE

One of the novelties of the numerical algorithm proposed in this study is the incorporation of ΔT during solidification in our simulations. Before the details of the numerical simulation procedure are presented, an overview of the methods developed to incorporate ΔT in the simulation is presented below.

How ΔT was Introduced in Binary Alloy Solidification Simulation?

Figure 5 presents a schematic of the steps during uni-directional solidification of the liquid from a melt superheat temperature T_{ini} to T_{eut}.

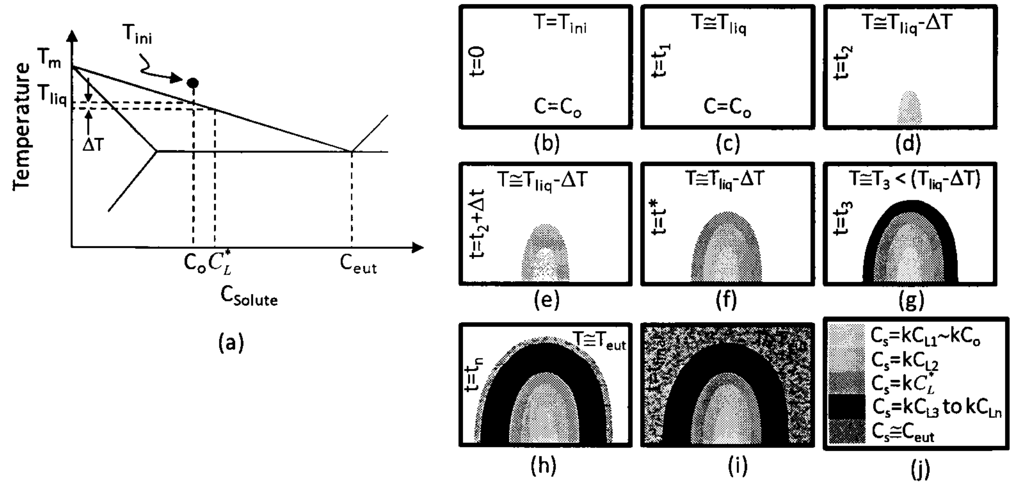

Figure 5: Schematic of the steps involved during uni-directional upward solidification of a binary alloy melt from a superheat temperature T_{ini} to T_{eut}. (a) schematic of binary alloy phase diagram, (b) to (i) various steps during solidification with increments of time in one CV and (j) index showing concentration of the various shades of solid phases in (b) to (i).

Table 2 shows the steps involved during solidification of a binary hypoeutectic alloy. In this study, all these steps were considered in each CV during solidification simulation. A detailed description of each step is also given below:

Step 1. T_{ini} decrease to T_{liq} (Figure 5(b) and Figure 5(c)) mainly due to the heat extraction during solidification. Concentration of the alloy melt is maintained at C_o. The time taken for this step is t_1.

Step 2. No solidification event occurs at T_{liq}. The first solid appears after an undercooling of ΔT as shown in Figure 5(d). The extent of undercooling is evaluated by Equation (1). The concentration of the first solid phase is represented by kC_{L1} wherein the liquid concentration C_{L1} is marginally greater than the average alloy composition C_o. The time taken for this step is t_2.

Step 3. During the next time step ($t_2+\Delta t$), the temperature remains constant as that in Step 2 (T_{liq} - ΔT). Evolution of the primary phase occurs during this step and the temperature will continue to remain constant (latent heat of fusion balances the heat extraction) until the solute concentration in the liquid at the mushy zone/liquid interface reaches C_L^* as shown in Figure 5(a) and 2(e).

Step 4. The solute concentration of the liquid at the mushy zone/liquid interface reaches C_L^* in time t* and the solute concentration in the solid is given by kC_L^* as shown in Figure 5(a) and Figure 5(f).

Step 5. The temperature begins to decrease again and layers of solid of the primary phase are formed at composition and the solute re-distribution in the liquid phases is defined by the concentration equation given by Equation (3), as shown in Figure 5(g). The solute concentration in the all layers of solid of primary phase is evaluated by Equation (5) for each time step if there is no re-melting of the solid phase due to convection of the liquid. In case re-melting occurs, the history of the solute concentration in the solid is used to evaluate the average concentration of the solid inside CV [12-14].

Step 6. Temperature of the liquid reaches the eutectic temperature and a layer of solid with eutectic solute concentration is formed marking the end of growth of the primary phase, as shown in Figure 5(h).

Step 7. The remaining liquid at the eutectic temperature is transformed into a two phase mixture to complete the solidification of the CV, as shown in Figure 5(i).

Table 2 The various steps in the solidification of a CV of a binary alloy.

Steps	**Time**	**T**	**C_S (New Layer)**	**C_L**	**Figure**
Step 1	0 to t_1	T_{ini} to T_{liq}	0	C_o	Figure 5(b) And Figure 5(c)
Step 2	t_2	T_{liq} to (T_{liq}-ΔT)	kC_{L1} ($\cong kC_o$)	$C_{L1} < C_L^*$	Figure 5(d)
Step 3	($t_2+\Delta t$)	(T_{liq}-ΔT) (no change)	kC_{L2}	$C_{L2} < C_L^*$	Figure 5(e)
Step 4	t^*	(T_{liq}-ΔT) (no change)	kC_L^*	C_L^*	Figure 5(f)
Step 5	t_3	$T_3 < (T_{liq}-\Delta T)$	kC_{L3}	$C_{L3} > C_L^*$	Figure 5(g)
Step 6	t_n	T_{eut}	C_{eut}	C_{eut}	Figure 5(h)
Step7	t_{final}	T_{eut}	C_{eut}	C_{eut}	Figure 5(i)

The unique feature in this model is the Steps 2 to 4 where the temperature of the CV is maintained at T_{liq}-ΔT until the solute concentration in the liquid inside CV reaches the equilibrium concentration of the solute, C_L^*, as suggested in Figure 5(a). This is observed during the solidification process of all binary alloys; however, the event has never been accounted for in any solidification simulation of binary alloys until this study. Introducing the Steps 2 to 4 will identify and account for the time period of recalescence during solidification.

Table 3 presents the list and details of the simulations carried out in this study. Typical deliverables from the simulations listed in Table 3 include transient temperature distribution, solidification time for the mushy zone/liquid interface, presented in Part I, λ_1, G and R, presented in Part II of this two-part publication. The finite-volume method was used in the algorithm presented in Figure 1(b). In the governing equations (Equations (2), (3), (6), (7) and (8)), the central differencing scheme was employed for all the diffusion terms, the convection terms were discretized by hybrid difference scheme. The implicit method was used for the transient terms. Convergent criteria for all parameters were determined by the two orders of mesh size, since the numerical simulation in present study is in two orders of accuracy.

Table 3: Identification and details of the simulations carried out.

Simulation Identification	**Type**	C_o	ΔT	**Comments**
SA	Upward Solidification	Al-3wt%Si	0	Algorithm in Figure 1(a) ($\beta=0$)
SB				Algorithm in Figure 1(b) ($\beta=0$)
S1	Upward Solidification	Al-3wt%Si	0	Algorithm in Figure 1(b) ($\beta>0$)
S2			Equation (1)	
S3		Al-7wt%Si	0	
S4			Equation (1)	
S5	Downward Solidification	Al-5wt%Si	0	
S6			Equation (1)	
S7		Al-7wt%Si	0	
S8			Equation (1)	

Figure 6 shows the flow chart for the procedure of numerical simulation. There are four loops named L1, L2, L3 and L4 in the procedure shown in Figure 6. L1 evaluates Equations (2) to (5) to obtain the transient temperature distribution, solute concentration distributions in liquid and solid and ϕ in the mushy zone at every time step during solidification. L2 evaluates Equations (6) to (8) to obtain the velocity distribution of liquid (fluid flow) using the Semi-Implicit Method for Pressure-Linked Equations (SIMPLE) algorithm [33]. L3 advanced the time steps during solidification. L4 has been newly proposed to evaluate the ΔT and λ_1 during solidification. The advantages of introducing loop L4 are those λ_1 can be predicted from solidification simulation at the macro-level (CV ~ 1 mm) itself and ΔT can be applied in a macro-level solidification simulation. Previous researchers could not introduce L4 because of the lack of experimental validation of transient temperature distribution and solidification time which would not enable an accurate prediction of the microstructure features such as λ_1. The parameters such as material and thermal properties as a function of temperature, undercooling, shrinkage and fluid flow from natural convection were optimized from several preliminary simulations to enable experimental validation of the transient temperature distribution and solidification times during simulation and further successfully introduce loop L4 in Figure 6.

The main feature of the algorithm presented in Figure 1 is the logic used in loop L1 shown in Figure 6. The procedure for loop L1 in a CV is as follows:

- At time step $t = t_m$, the solute concentration distribution in all three zones (liquid, solid and mushy zone) were determined by solving the concentration equation {Equation (3)}.
- Determine whether the CV is inside the mushy zone by checking whether T reached T_{liq}-ΔT by solving energy equation (2).
- Temperature distribution inside the mushy zone is calculated by solving the Equation (4) or is assumed as (T_{liq}-ΔT) for $C_L < C_L^*$ (Figure 5(d) to Figure 5(f)). Temperature distribution inside the liquid and solid phases is evaluated from the energy equation {Equation (2)}.
- Liquid fraction, ϕ in the mushy zone is evaluated with the temperature distribution data from the energy equation {Equation (2)}.
- Calculate average solute concentration of the solid phase using Equation (5) if there is no re-melting of the solid phase. In case of solid phase re-melting that may occur due to the fluid flow, the history of previous average solute concentration in the solid phase is used for the current time step [12].
- All the above steps are repeated until convergence.

It must be noted that the energy equation was used to evaluate temperature distribution only inside pure liquid and pure solid regions alike. The energy equation was used to evaluate liquid fraction inside the mushy zone, where temperature has been already evaluated by the local equilibrium assumption (equation (4)). Initially the temperature of the liquid inside a CV is evaluated by the energy equation {Equation (2)}. If the evaluated temperature is less than T_{liq} then, we have to re-evaluate the temperature with Equation (4), since the CV would have reached the mushy zone. This newly evaluated temperature of the mushy zone will be used in the energy equation {Equation (2)} to evaluate the first ϕ in the mushy zone. This evaluation is still not accurate in the first iteration of loop 4 since the ΔT has not yet been considered (ΔT=0). Hence, at the end of the first iteration of loop L4, the solidification simulation is equivalent to that with ΔT=0. The next iteration of loop L4 will update ΔT with a positive value and subsequent iterations of L4 will yield a modified temperature distribution in the CV.

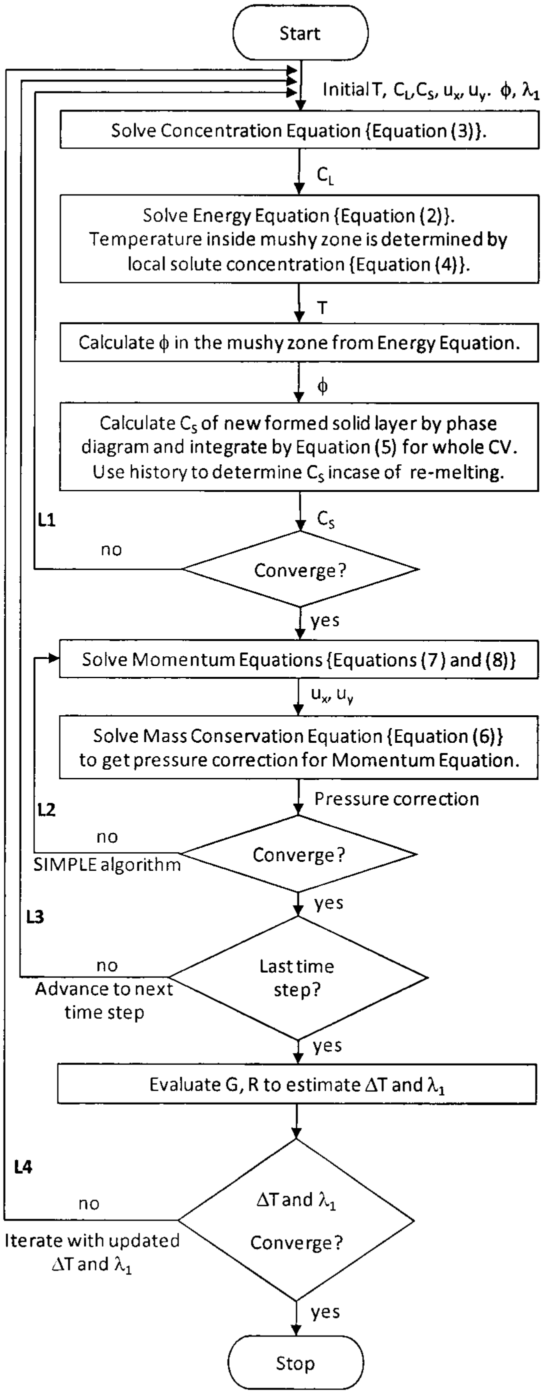

Figure 6: Numerical simulation procedure for the new proposed algorithm.

Loop L1 in Figure 6 shows the coupling scheme for energy and concentration equations of the new algorithm proposed in the present study. The main difference between the existing algorithm by Felicilli et al [12] shown in Figure 1 and the new algorithm in loop L1 of Figure 6 is that in the latter the concentration equation is solved first in all the three zones to avoid the instability caused by the phase transformation term in the energy equation. Further, the new algorithm solely uses the heat transfer condition to evaluate liquid fraction ϕ in the mushy zone. These two differences will enable introduction of ΔT term in the solidification and further reduce computational time. Moreover, contrary to conventional methods, the liquid fraction ϕ was evaluated solely from the energy equation in the present approach.

The previous state of simulating the macro structure (-1mm length scale) [12] is such that the critical effect of ΔT could not be considered and the instability of the energy equation due to the fact that phase transformation term could only be overcome by introducing the concentration equation into the energy equation in the mushy zone. Solving energy equation with previous method [12] also results in a significantly high computation cost. Further, no successful validation in heat transfer condition of the numerical simulation has been reported. In the present study, these shortcomings were overcome by a new numerical method to solve the energy and concentration equations in the three zones (solid, mushy and liquid) which also enabled us to introduce the ΔT term in our formulations. This method will be discussed later.

RESULTS AND DISCUSSION

All the results and discussion are in reference to Figure 2 and Figure 6. The results and discussion are presented for the following topics:

- Comparison of new algorithm with the popular version.
- Validation of transient temperature distribution.
- Effect of ΔT on solidification time (location of mushy zone/liquid interface)

Comparison of New Algorithm with the Popular Version

The results at the end of the first iteration of L4 in Figure 6 is presented as simulation SA and were used to compare with the results from the popular algorithm (simulation SB) [12-15] to determine the reliability of this newly proposed algorithm (shown in Figure 1(b) and Figure 6).

Comparison of the transient temperature distribution for SA obtained in the present study at the end of the first iteration of L4 in Figure 6 and that SB simulated by the algorithm presented in Heinrich et al [14] (Figure 1(a)) is reported in Figure 7.

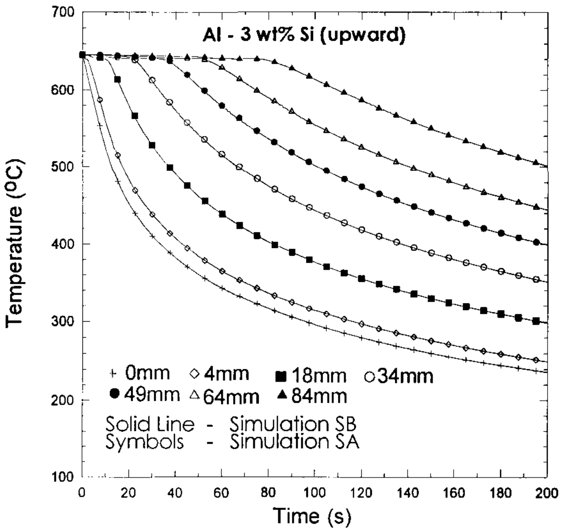

Figure 7: Transient temperature distributions for simulations SA and SB at r = 0 for various locations: y = 0, 4, 18, 34, 49, 64, and 84 mm (shown in Figure 2(a)) during upward solidification.

Figure 7 shows the temperature distribution at r = 0 during solidification without the effect of ΔT for seven locations between y = 0 and y = 84 mm, respectively. Also shown is the comparison between the present work and that of Heinrich et al [14] showing that using the new algorithm proposed in this study is as accurate as the popular method which indicate that the alternative logic used to determine ϕ from solely the heat transfer conditions rather than the concentration equation is valid. Further, the computing time for the new algorithm to obtain the results shown in Figure 7 was reduced by a maximum of 50% depending on the initial solute concentration of the alloy and the boundary conditions. The average cooling rates investigated in Figure 7 varied between 0.72 °C/s to 2.05 °C/s.

Validation of Transient Temperature Distribution

Transient temperature distribution is critical to evaluate solidification time, G, R and λ_1. The transient temperature distribution in the computing domain was validated with experiment results presented by two groups of researchers [18, 30]. Figure 8(a) and Figure 8(b) show the validation of the present algorithm using the experiments by Peres et al [18] and Spinelli et al [30]. Figure 8(a) and Figure 8(b) are for simulations S2 and S8, respectively. Simulations S2 and S8 show a good agreement with experiment and validate the simulations. In Figure 8(a) the maximum deviation in temperature is less than 10 °C located at y=64mm and t $\approx$ 100 s for upward solidification. When compared with the initial melt temperature of 644.05 °C, the deviation is less than 2%. In Figure 8(b), the maximum deviation is less than 13 °C (2%) located at y=64mm and t $\approx$ 100 s for downward solidification.

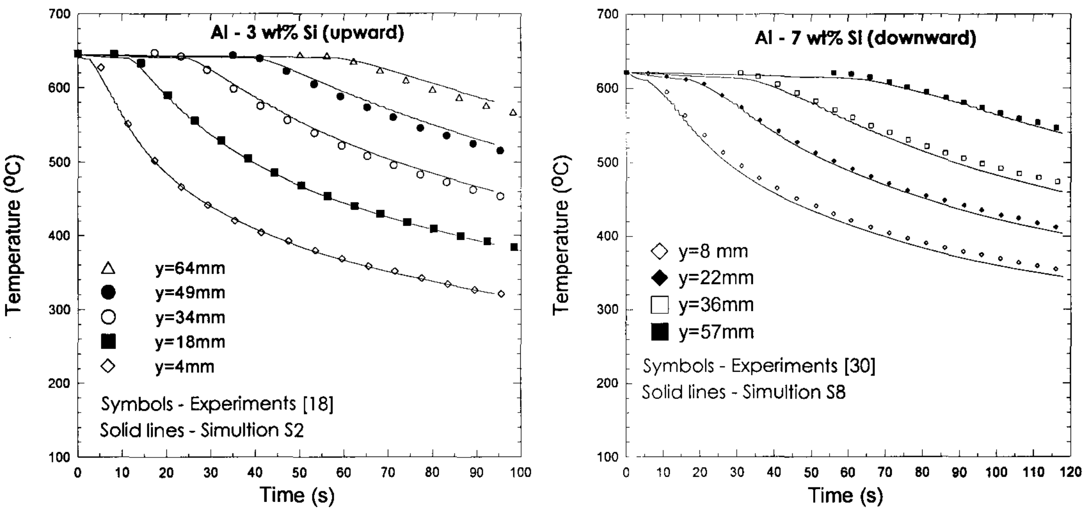

(a) (b)

Figure 8: Validation of transient temperature distributions for simulations S2 and S8 at r = 0 with experiment data by (a) Peres et al [18] for upward solidification simulation S2 and (b) Spinelli et al [30] for downward solidification simulation S8.

Effect of Undercooling on Solidification Time

Peres et al [18] have carried out experiments on upward solidification (Figure 2(a)) with Al-3wt%Si and Al-7wt%Si alloys, respectively. They have reported the solidification time (location of the mushy zone/liquid interface) by estimating the time taken for the interface to reach the location of each thermocouple in the experiments. These experiments were used to validate simulations S2 and S4. Figure 9 shows the results of these validations. Figure 9(a) shows the validation of the solidification times from simulation S2 (with ΔT) with the experiments [18] along with results from S1 (no ΔT). Figure 9(b) shows the validation of the solidification time from simulation S4 (with ΔT) with the experiments [18] along with results from S3 (no ΔT). Figure 9 shows that the simulations that include the effect of ΔT on solidification has as excellent agreement with the experiments with a maximum time deviation of <1.5% for the farthest thermocouple (y = 84 mm) in both Figure 9(a) and Figure 9(b) (refer to Figure 2(a)). The deviation may be due to the lack of uni-directional heat transfer in the experiments towards the later stages of solidification. However, the negligible deviation shows that experiments were nearly uni-directional for most of the solidification time. It can be seen in Figure 9(a) and Figure 9(b) that simulations S1 and S3 with no consideration of ΔT during solidification has a large deviation from the respective experiments. The maximum time deviation in S1 and S3 from experiments is 11.4% and 19.8%, respectively, at y=84 mm. In Al-3wt%Si alloy, the total time taken for the mushy zone/liquid interface to travel between y = 0 to y= 84 mm is 88 s from experiments, 86.7 s for S2; and 78 s for S1. In Al-7wt%Si alloy, the total time taken for the mushy zone/liquid interface to travel between y = 0 to y= 84 mm is 96 s from experiments, 94.7 s for S4; and 77 s for S3. The consideration of ΔT in the simulation reduces the value of the mushy zone/liquid interface velocity, R because it requires longer time for each CV to reach an undercooled temperature state (T_{liq}-ΔT) before any solidification event.

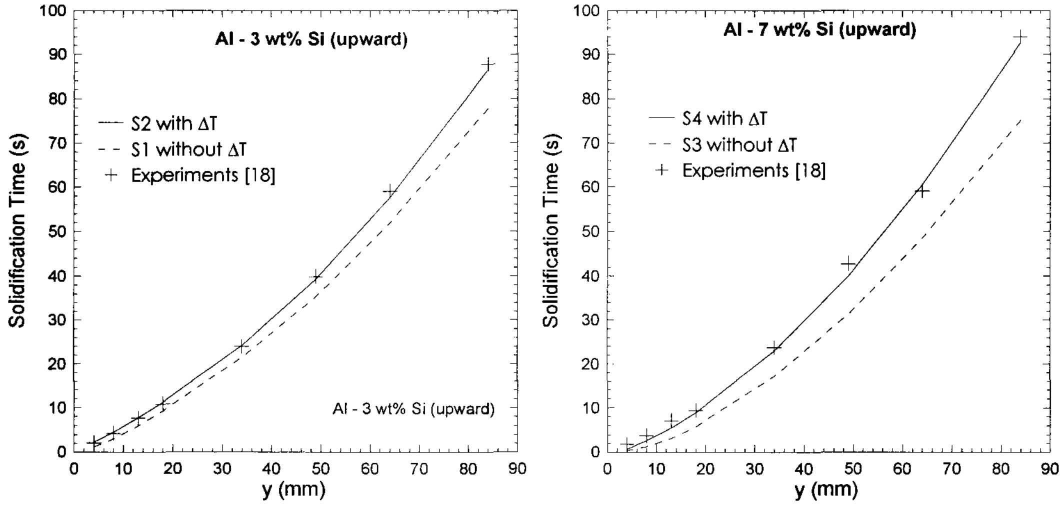

(a) (b)

Figure 9: Validation of mushy zone/liquid interface locations in simulations S2 and S4 with experiment results [18]. (a) validation of S2 along with results from S1 and (b) validation of S4 along with results from S3.

Spinelli et al [30] have carried out experiments on downward solidification with Al-5wt%Si and Al-7wt%Si alloys, respectively. The results from these experiments were used to validate simulations S6 and S8, respectively. Figure 10(a) and Figure 10(b) shows the validation of simulation S6 and S8, respectively. Also, shown in Figure 10(a) and Figure 10(b) are the solidification times for simulations S5 and S7, respectively. Figure 10 shows that simulations S6 and S8 (with ΔT) have better agreement with the experiment results. The maximum deviation of S6 and S8 from experiments at y=85 mm is 3.6% and 16%, respectively. The larger deviations from the experiments observed for the downward solidification in Figure 10 as compared with the upward solidification presented in Figure 9 may be due to the fact that in experiments [18, 30], the temperature gradient between the side wall of the container (right side of computing domain) and the liquid alloy inside increases with time in the experimental condition. In downward solidification, the fluid flow is more pronounced due to the natural convective currents induced by this temperature gradient in experiments, which results in a more significantly increased temperature gradient in the liquid side of mushy zone/liquid interface causing a smaller value of R and longer solidification time in downward solidification in experiments. Another reason for the marginal under prediction of solidification times in Figure 9 and Figure 10 may be due to the added latent heat of fusion of the eutectic phases which will result in an over prediction of R and an under-prediction of the solidification times. In Al-5wt%Si alloy, the total solidification times for experiment, S6 and S5 are 113 s, 109 s and 97 s, respectively. In Al-7wt%Si alloy, the total solidification times for experiment, S8 and S7 are 130 s, 108 s and 96 s, respectively.

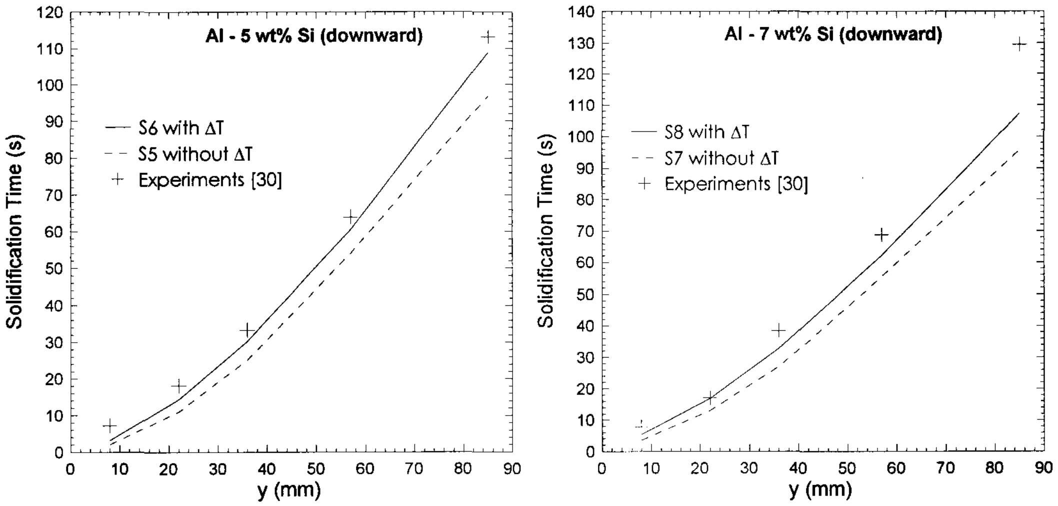

(a) (b)

Figure 10: Validation of mushy zone/liquid interface locations in simulations S6 and S8 with experiment results [30]. (a) validation of S6 along with results from S5 and (b) validation of S8 along with results from S7.

SUMMARY AND CONCLUSIONS

A new and more efficient algorithm for solidification simulation of binary alloys has been proposed and validated to include the effect of temperature undercooling of the liquid at the dendrite tip during solidification. The present algorithm treated the strong non-linearity caused by the phase transformation term in the energy equation by solving the concentration equation before solving the energy equation. Further, the energy equation was wholly used instead of the concentration equation to evaluate the liquid fraction inside the mushy zone. The transient temperature distribution in liquid, mushy zone and solid regions during solidification has been evaluated by the use of this new algorithm and the results have been validated by experiments. Solidification time which indicated the instantaneous location of the mushy zone/liquid interface had been evaluated and validated with experiments as well.

In all the above-mentioned simulation results, the effect of undercooling of the liquidus temperature prior to the solidification event has been successfully quantified. Simulations with the effect of undercooling were found to increase solidification time and be far more agreeable with the experiment results for solidification times than those without the inclusion of the undercooling term.

REFERENCES.

[1] JMatPro, 4.1 ed Guildford ,UK.: Sente Software Ltd.

[2] D. P. Sekulic, P. K. Galenko, M. D. Krivilyov, L. Walker, and F. Gao, "Dendritic growth in Al-Si alloys during brazing. Part 2: Computational modeling," *International Journal of Heat and Mass Transfer*, vol. 48, pp. 2385-2396, 2005.

[3] Factsage, 5.5 ed Madison, WI, USA.: Computherm LLC.

[4] M. Gunduz and J. D. Hunt, "The measurement of solid-liquid surface energies in the Al-Cu, Al-Si and Pb-Sn systems," *Acta Metallurgica*, vol. 33, pp. 1651-1672, 1985.

[5] C.-J. Ho and R. Viskanta, "Heat transfer during inward melting in a horizontal tube," *International Journal of Heat and Mass Transfer*, vol. 27, pp. 705-716, 1984.

[6] E. M. Sparrow, S. V. Patankar, and S. Ramadhyani, "Analysis of melting in the presence of natural convection in the melt region," *Journal of Heat Transfer, Transactions ASME*, vol. 99, pp. 520-526, 1977.

[7] L. S. Yao, "Natural convection effects in the continuous casting of a horizontal cylinder," *International Journal of Heat and Mass Transfer*, vol. 27, pp. 697-704, 1984.

[8] M. C. Flemings, *Solidification processing*. New York, NY.: McGraw-hill Book Co., 1974.

[9] W. D. Bennon and F. P. Incropera, "A continuum model for momentum, heat and species transport in binary solid – liquid phase change systems - I. Model formulation," *International Journal of Heat and Mass Transfer*, vol. 30, pp. 2161-2170, 1987.

[10] W. D. Bennon and F. P. Incropera, "A continuum model for momentum, heat and species transport in binary solid – liquid phase change systems - II. Application to solidification in a rectangular cavity," *International Journal of Heat and Mass Transfer*, vol. 30, pp. 2171-2178, October 1987.

[11] W. D. Bennon and F. P. Incropera, "Numerical analysis of binary solid – liquid phase change using a continuum model," *Numerical Heat Transfer*, vol. 13, pp. 277-296, 1988.

[12] S. D. Felicelli, J. C. Heinrich, and D. R. Poirier, "Simulation of freckles during vertical solidification of binary alloys," *Metallurgical Transactions B (Process Metallurgy)*, vol. 22, pp. 847-859, Dec. 1991.

[13] S. D. Felicelli, J. C. Heinrich, and D. R. Poirier, "Numerical models for dendritic solidification of binary alloys," *Numerical Heat Transfer, Part B: Fundamentals*, vol. 23, pp. 461-481, 1993.

[14] J. C. Heinrich and D. R. Poirier, "The effect of volume change during directional solidification of binary alloys," *Modeling and Simulation in Materials Science and Engineering*, vol. 12, pp. 881-899, Sep. 2004.

[15] E. McBride, J. C. Heinrich, and D. R. Poirier, "Numerical simulation of incompressible flow driven by density variations during phase change," *International Journal for Numerical Methods in Fluids*, vol. 31, pp. 787-800, Nov. 1999.

[16] R. G. Santos and M. L. N. M. Melo, "Permeability of interdendritic channels," *Materials Science & Engineering A (Structural Materials: Properties, Microstructure and Processing)*, vol. 391, pp. 151-158, Jan. 2005.

[17] V. R. Voller and C. Prakash, "Fixed grid numerical modeling methodology for convection - diffusion mushy region phase – change problems," *International Journal of Heat and Mass Transfer,* vol. 30, pp. 1709-1719, 1987.

[18] M. D. Peres, C. A. Siqueira, and A. Garcia, "Macrostructural and microstructural development in Al-Si alloys directionally solidified under unsteady-state conditions," *Journal of Alloys and Compounds,* vol. 381, pp. 168-181, November 3 2004.

[19] D. R. Poirier, "Permeability for flow of interdendritic liquid in columnar-dendritic alloys," *Metallurgical Transactions B (Process Metallurgy),* vol. 18B, pp. 245-255, 1987.

[20] D. Bouchard and J. S. Kirkaldy, "Prediction of dendrite arm spacings in unsteady- and steady-state heat flow of unidirectionally solidified binary alloys," *Metallurgical and Materials Transactions B (Process Metallurgy and Materials Processing Science),* vol. 28B, pp. 651-663, Aug. 1997.

[21] J. D. Hunt, "Solidification and casting of metals," *Proceedings of the International Conference on Solidification and Casting of Metals, The Metals Society, London,* pp. 3-9, 1979.

[22] P. Lehmanna, R. Moreaub, D. Camela, and R. Bolcatob, "A simple analysis of the effect of convection on the structure of the mushy zone in the case of horizontal Bridgman solidification. Comparison with experimental results," *Journal of Crystal Growth,* vol. 183, pp. 690-704, 1998.

[23] R. Trivedi, "Interdendritic spacing: part II. A. comparison of theory and experiment," *Metallurgical Transactions A (Physical Metallurgy and Materials Science),* vol. 15A, pp. 977-982, 1984.

[24] M. H. Burden and J. D. Hunt, "Cellular and dendritic growth. I," *Journal of Crystal Growth,* vol. 22, pp. 99-108, 1974.

[25] M. H. Burden and J. D. Hunt, "Cellular and dendritic growth. II," *Journal of Crystal Growth,* vol. 22, pp. 109-116, 1974.

[26] P. C. Carman, "Fluid flow through granular beds," *Trans. Inst. Chem. Engs.,* vol. 15, pp. 150-156, 1937.

[27] P. C. Carman, "The determination of the specific surface of powders " *I. J. Soc. Chem. Indus.,* vol. 57, pp. 225-234, 1938.

[28] S. Asai and I. Muchi, "Thearoetical analysis and model experiments of the formation mechanism of channel - type segregation," *Transactions of the Iron and Steel Institute of Japan,* vol. 18, pp. 290-298, 1978.

[29] P. Lehmann, R. Moreaub, D. Camela, and R. Bolcatob, "A simple analysis of the effect of convection on the structure of the mushy zone in the case of horizontal Bridgman solidification. Comparison with experimental results," *Journal of Crystal Growth,* vol. 183, pp. 690-704, 1998.

[30] J. E. Spinelli, M. D. Peres, and A. Garcia, "Thermosolutal convective effects on dendritic array spacings in downward transient directional solidification of Al-Si alloys," *Journal of Alloys and Compounds,* vol. 403, pp. 228-238, Novermber 2005.

[31] T. Magnusson and L. Arnberg, "Density and solidification shrinkage of hypoeutectic aluminum-silicon alloys," *Metallurgical and Materials Transactions A: Physical Metallurgy and Materials Science*, vol. 32, pp. 2605-2613, Oct. 2001.

[32] H. Wang, "Solidification Simulation of Binary Al-Si Alloys: Prediction of Primary Dendrite Arm Spacing with Macro-scale Simulations (~1mm Length Scale)," in *Department of Mechanical Engineering* McMaster University, Hamilton, Ontario, Canada, Ph. D. Thesis, 2009.

[33] S. V. Patankar, *Numerical heat transfer and fluid flow*. New York: McGraaw-Hill, 1980.

SOLIDIFICATION OF Al-Si ALLOYS WITH DENDRITE TIP UNDERCOOLING
PART 2: SOLIDIFICATION PARAMETERS

Hongda Wang[1,2], Mohamed S. Hamed[1], Sumanth Shankar[2,*]
[1]Thermal Processing Laboratory (TPL)
[2]Light Metal Casting Research Centre (LMCRC)
McMaster University, Hamilton, ON, Canada L8S 4L7

ABSTRACT

In Part1 of this two-part publication, a new and improved algorithm for solidification simulation of binary alloys with the capabilities of introducing the undercooling of the liquidus temperature prior to the solidification event of the primary phase had been proposed and validated with experiments. The effect of shrinkage and natural convection was considered in the cases of both upward and downward solidification. The Part 1 of this publication presented the details of the new algorithm approach and the validation of the transient temperature distribution and solidification time at mushy zone/liquid interface. In this Part 2 of the publication, the effect of undercooling of the liquidus temperature prior to the solidification event during upward and downward solidification of binary Al-Si hypoeutectic alloys on the fluid flow (velocity profile), G, R and λ_1 had been investigated and discussed. Consideration of undercooling was found to increase G and reduce R in both cases of upward and downward solidification. During upward solidification, undercooling had only insignificant effect on fluid flow and λ_1. However, during downward solidification, undercooling would significantly increase flow velocity and decrease λ_1. In upward solidification, the fluid flow was caused by the effect of solidification shrinkage alone. The primary dendrite arm spacing has been validated with results from uni-directional solidification experiments. It was found that better agreement could be obtained when undercooling was considered.

NOMENCLATURE

C_o	Average alloy composition (wt%);
D	Solute diffusivity coefficient of liquid (6.25 × 10^{-9} ($m^2 s^{-1}$)) [1];
G	Temperature gradient in liquid at the mushy zone/liquid interface (°C mm^{-1});
k	Average partition coefficient (0.116) [2];
m	The slope of liquidus line (– 6.675 (K $wt\%^{-1}$)) [2];
R	Velocity of mushy zone/liquid interface (mm s^{-1});
$\dot{T}$	Instantaneous tip cooling rate = G×R (°C s^{-1});
ΔT	Undercooling of T_{liq} (°C);
U	Flow velocity in the liquid of mushy zone/liquid interface (mm.s^{-1});
Γ	Gibbs-Thomson coefficient (1.97 × 10^{-7} (K m^{-1})) [3];

---

[*] Corresponding Author: shankar@mcmaster.ca , voice: (905) 512-1324

ϕ Liquid fraction;

λ_1^0 Primary arm spacing if no fluid flow effect is considered (µm);

λ_1 Primary arm spacing (µm);

INTRODUCTION

Presently, solidification simulations in the macro-scale (Control Volume, CV ~ 1mm) do not predict the microstructural features of the solidified alloy such as primary and secondary dendrite arm spacings, λ_1 and λ_2, respectively [4-11]. One of the main reasons for this is the lack of accuracy in predicting the transient temperature distribution and hence, the progressive locations of the mushy zone/liquid interface (solidification time). The new algorithm presented in the Part 1 of this two-part publication enables predictions of λ_1 because the transient temperature distribution and the solidification times have been accurately predicted and validated with experiments. The reasons are those the new approach included the effect of undercooling of the liquidus temperature prior to the solidification event, ΔT, and further optimized the materials properties as a function of temperature. Traditionally, the undercooling cannot be considered in solidification simulations of binary alloys because the order of magnitude of the diffusion coefficient of the solute in the liquid phase is four times less than that of the thermal diffusivity and hence, the simulation with ΔT could not be practically completed. In the new approach presented in Part 1, the liquid fraction ϕ in the mushy zone is evaluated by the energy equation with the heat transfer conditions which will enable successful completion of the simulation with the ΔT term. Further, the new simulation approach has been shown to be faster than the traditional one [7-10].

Since it has been shown in Part 1 that the new numerical algorithm is valid and accurate, it can predict the fluid flow velocities in the computing domain accurately as well which will enable a valid prediction of the transient temperature gradient, G and velocity R at the mushy zone/liquid interface during solidification. Evaluation of transient G and R will enable prediction of λ_1 which will be a valuable tool to predict the solidification microstructure from macro scale.

GOVERNING EQUATIONS

The governing equations presented in the Part 1 are valid for this part of the publication as well.

There are many theoretical and empirical equations to estimate λ_1 from the values of transient G and R of the mushy zone/liquid interface [12-22]. However, only one of the empirical and theoretical expressions, presented by Bouchard et al [13], to estimate λ_1 is for the unsteady solidification conditions which is typically observed in most uni-directional solidification processes. Equation (1) presents this expression to estimate λ_1 for unsteady solidification conditions.

$$\lambda_1^0 = a_1 \left(\frac{16 C_o^{\frac{1}{2}} G_o \varepsilon \Gamma D}{(1-k) m G R} \right)^{\frac{1}{2}} \tag{1}$$

The model in Equation (1) does not consider fluid flow induced by shrinkage or natural convection during solidification. Equation (2) presents the expression developed by Lehmann et al [23] to estimate λ_1 with the effect of fluid flow during solidification.

$$\lambda_1 = \lambda_1^0 \left(1 + \frac{U}{R} \right)^{-\frac{1}{2}} \tag{2}$$

In this study, Equation (1) coupled with Equation (2) was used to evaluate λ_1. Equation (3) presents the expression for ΔT as defined in Equation (1) in Part 1. The magnitude of undercooling in the present work is not a constant throughout the solidification process but is updated at every time step for each control volume (CV) in the domain.

$$\Delta T = (\frac{GD}{R}) + \frac{\left(-8mR(1-k)C_o\Gamma\right)^{\frac{1}{2}}}{D^{\frac{1}{2}}} \tag{3}$$

SIMULATIONS

Table 1 presents the list of simulations along with the individually assigned identification that was used in this study.

Table 1: Identification and details of the simulations carried out.

Simulation Identification	Type	C_o	ΔT
S1	Upward Solidification	Al-3wt%Si	0
S2			Equation (3)
S3		Al-7wt%Si	0
S4			Equation (3)
S5	Downward Solidification	Al-5wt%Si	0
S6			Equation (3)
S7		Al-7wt%Si	0
S8			Equation (3)

Al-3wt%Si and Al-7wt%Si alloys were used for upward solidification simulations; and Al-5wt% Si and Al-7wt%Si alloys were used for the downward solidification simulations. The schematics of the domain geometry and the boundary conditions for C_L and T are presented in Figure 3(a) and Figure 3(b) for upward and downward solidifications, respectively, in Part 1 of this publication. The velocities at the boundaries are presented in Figure 4(a) and Figure 4(b) for upward and downward solidifications, respectively, in Part 1 of this publication. Initial conditions are also identical as indicated in Part 1.

Results from uni-directional solidification experiments carried out by Peres et al [24] and Spinelli et al [25] were used to validate the results for λ_1 obtained from the simulations presented in Table 1, respectively.

RESULTS AND DISCUSSION

The results and discussions will be presented for the following topics.

- Effect of ΔT in the liquid on fluid flow.
- Effect of ΔT in the liquid on G.
- Effect of ΔT in the liquid on R.
- Effect of ΔT in the liquid on λ_1.

Effect of Undercooling on Fluid Flow – Case of Upward Solidification

Figure 1(a) to Figure 1(c) present the velocity profiles (m/s) for simulation S2 and Figure 1(d) to Figure 1(f) present that for simulation S1. In these two simulations (upward solidification) the positive density gradient is in the direction of the gravity vector (refer to Figure 3(a) in Part 1) and hence, there will be no natural convection of the liquid which is evident from fluid flow from top to bottom and the absence of circular flow. Since, only shrinkage affects the fluid flow velocities and shrinkage is almost identical in both simulations, S2 and S1, there is a marginal increase in velocity of S1 (without ΔT) as compared to that in S2 (with ΔT) due to the larger value of R in S1. A similar observation was made when simulation S4 was compared with S3 as well.

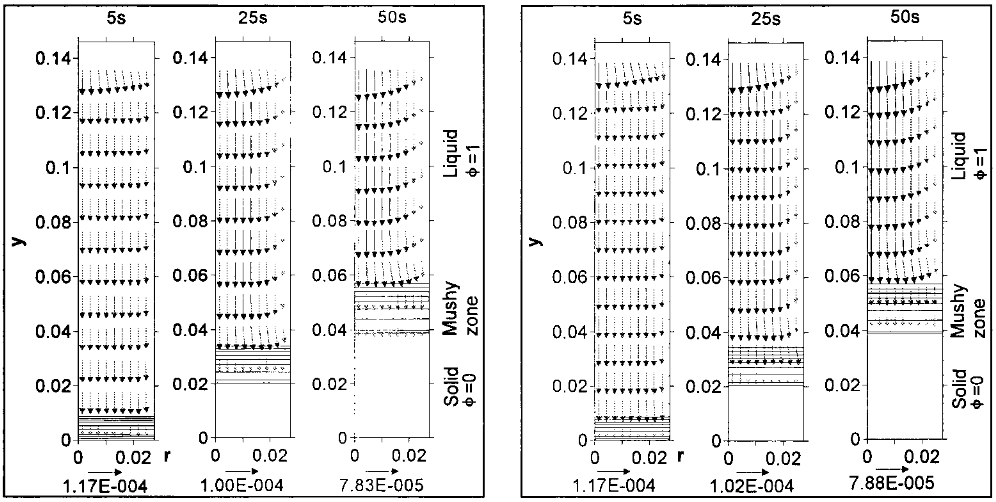

(a) (b) (c) (d) (e) (f)

Figure 1: Development of fluid flow velocities ($m.s^{-1}$) in (a) to (c) for solidification simulation S2 with effect of undercooling for t = 5s, 25s and 50s, respectively, and (d) to (f) for solidification simulation S1 without effect of undercooling for t = 5s, 25s and 50s, respectively. The magnitudes of maximum velocities are presented at the bottom of (a) to (f), respectively.

Effect of Undercooling on Fluid Flow – Case of Downward Solidification

The development of fluid flow with the effect of undercooling for simulation S6 is shown in Figure 2. Figure 2(a) to Figure 2(f) show snap shots of the velocity field in the computing domain at increasing solidification times of 5, 25, 50, 75, 100 and 110 s, respectively. Maximum magnitude of the velocity at each time is shown at the bottom of the respective snap shot figure. Figure 2 (f) shows typical domains found in the simulation results: *solid, mushy zone and liquid*. The solid lines inside the mushy zone in Figure 2 represent the constant ϕ lines from $\phi = 0.9$ to $\phi = 0.1$.

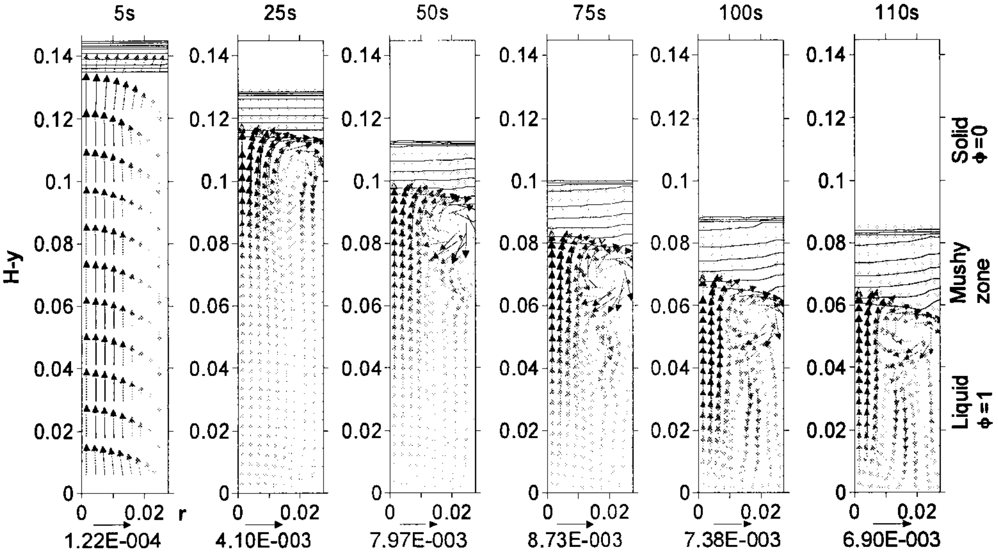

(a) (b) (c) (d) (e) (f)

Figure 2: Development of fluid flow velocity (m.s^{-1}) during solidification simulation S6 with effect of undercooling for t = (a)5s; (b)25s; (c)50s; (d)75s; (e)100s and (f) 110 s. The magnitudes of maximum velocities are presented at the bottom of (a) to (f), respectively.

Table 2 presents a summary of the results shown in Figure 2. Table 2 suggests that effect of shrinkage is dominant at the beginning of solidification due to the lack of natural convection. The effect of natural convection gradually begins to dominate and the effect of shrinkage on fluid flow velocity becomes negligible as solidification time increases. At the beginning of solidification, R is high and this induces an instantaneous flow field in the liquid which is primarily caused by the solidification shrinkage. However, the flow due to the density gradient in the liquid develops from an initial rest to subsequently dominate the fluid flow regime over the solidification shrinkage.

Higher velocities of fluid flow caused by natural convection will result in greater circular flow regions as seen in Figure 2. There are two mechanisms that affect strength of fluid flow due to natural convection. One of them is the density gradient caused by the temperature and solute concentration gradients in the liquid which is directly proportional to the fluid velocity and the other is the height of the liquid (space available for fluid flow) which is inversely proportional to fluid velocity. Between times t=5s and 75s, the effect of the density gradient greatly increases the fluid flow velocity due to natural convection. However, between t = 75s and 110s the effect of the reducing height of the liquid marginally decreases the fluid flow velocity due to natural convection. The maximum fluid flow velocity is always in the region close to r = 0 and is in the direction of heat extraction. Figure 2 and Table 2 also show that the length of the mushy zone is continuously increasing indicating an unsteady solidification condition at all times because of the continuously decreasing heat flux $\vec{q}$ at y =0 mm.

Table 2: Development of fluid flow for simulation S6.

Time (s)	Maximum Velocity (mm/s)	Flow due to Shrinkage	Flow due to Natural Convection	Height of the Mushy Zone (mm)
5	1.22×10^{-4}	Dominant flow from bottom to top	Small circular flow limited to mushy zone/liquid interface around r = 27.5 mm	13
25	4.1×10^{-3}	Small effect of shrinkage in liquid. Large effect of shrinkage in mushy zone.	Dominates the liquid. Small effect in mushy zone.	20
50	7.97×10^{-3}		Strengthens in liquid.	23
75	8.73×10^{-3}		Strengthens further in liquid.	24
100	7.38×10^{-3}		Weakens in liquid.	28
110	6.9×10^{-3}		Further weakens in liquid.	31

Maximum flow in the computing domain can always be observed at left top of the liquid region from Figure 2(b) to Figure 2(f) (centre of the solidifying cylinder). Fluid flow with higher temperature from liquid region is driven into mushy zone in this region. Therefore, solidification time will increase in this region and hence the constant liquid fraction lines are compressed along the y direction at the liquid/mushy zone interface (Figure 2(b) to Figure 2(f)). With the development of clockwise flow, direction of flow velocity at interface of liquid/mushy zone is primarily in the positive r direction. This flow pattern will create accumulation of enthalpy in the right top side of the liquid region (along the wall of the solidifying cylinder). As a result, solidification in this region is slowed down and the constant liquid fraction lines along the wall are also compressed as shown in Figure 2(d) to Figure 2(f).

The normalized iso - stream function lines with the effect of undercooling in simulation S6 are shown in Figure 3. Figure 3(a) to Figure 3(f) show snap shot of the normalized iso-streamlines in the computing domain at increasing solidification times of 5, 25, 50, 75, 100 and 110 s, respectively. Maximum magnitude of stream function is shown below each snap shot figure for the respective times. Similar to Figure 2, the top solid lines inside the mushy zone in Figure 3 represent the constant liquid fraction lines from $\phi = 0.9$ to $\phi = 0.1$. The strength of fluid flow can also be implied by the maximum magnitude of stream function. Maximum magnitude of stream function in Figure 3 changes from a lower value (Figure 2(a)) to a maximum value (Figure 2(d)) and back again to a lower value (Figure 2(f)), which indicates the strength of flow develops from weaker to stronger and back to weaker as the solidification proceeds. Arrows in the streamlines in Figure 3 illustrate the flow direction, which indicates that flow develops from bottom to top at t = 5s. Circular flow developed after t = 25s implies that the flow is dominated by natural convection. Clockwise cell can be observed for times between t = 25 and 75s. After t = 100s, a second flow cell is created at the right bottom side of the computing domain due to the higher velocity at t = 75s during the development of the fluid flow. A notable feature is the development and strengthening of a secondary circular flow starting from t = 75s as shown in Figure 2 and Figure 3.

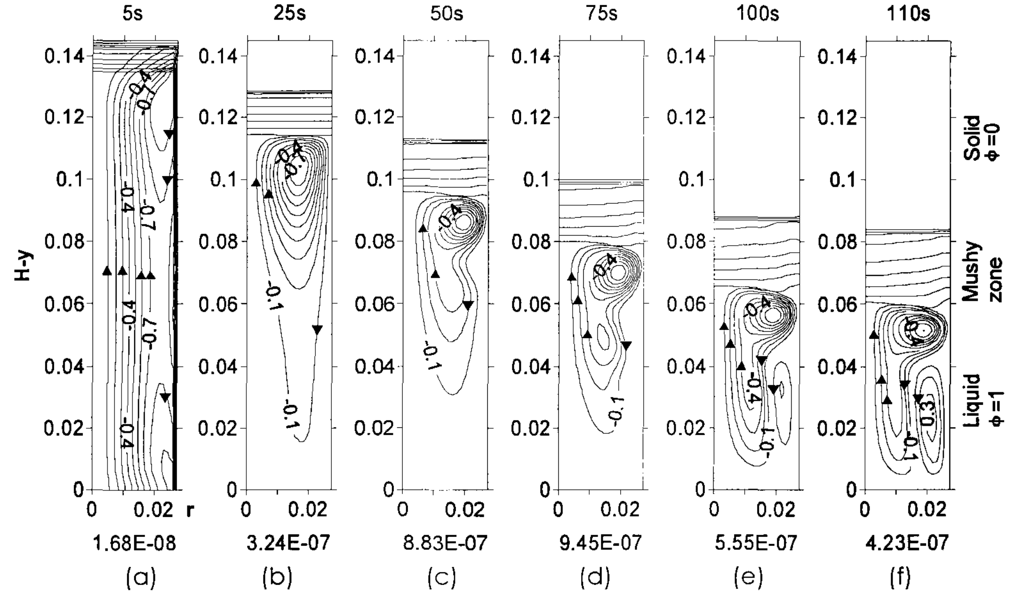

Figure 3: Development of contours of normalized stream function during solidification simulation S6 with effect of undercooling for t = (a)5s; (b)25s; (c)50s; (d)75s; (e)100s and (f) 110 s. The maximum magnitudes of stream function ($m^3.s^{-1}$) are presented at the bottom of (a) to (f), respectively.

Figure 4(a) to Figure 4(d) show the velocity distribution in both y and r directions at t =5s and t = 50s for simulation S6, respectively. As shown in Figure 4(a) and Figure 4(b) for velocities at t = 5s, the maximum magnitude of u_y is more than 10 times that of u_r, which indicates that the flow is dominated by shrinkage. Positive direction of u_y located at region close to right side of computing domain (wall of solidifying cylinder) implies that natural convection has already affected fluid flow even if it has not dominated the flow pattern at t = 5s. The flow in the middle of the solidifying cylinder in the y direction is nearly fully developed as indicated by the lack of variation in the magnitude of u_y and u_r at locations (H-y) = 0.04, 0.06 and 0.08 m in Figure 4 (a) and Figure 4(b), respectively. The higher variation in the magnitudes of velocities in Figure 4 (a) and Figure 4(b) at locations (H-y) = 0.01 and 0.113 m is due to the effect of the cavity end walls. In Figure 4(c) and Figure 4(d), the lack of significant variation between the maximum magnitudes of u_y and u_r at time t= 50 s show that the flow is circular and caused predominantly by natural convection. At t = 50s, the maximum velocity is located near the liquid/mushy zone interface at a location close to the left side of the computing domain.

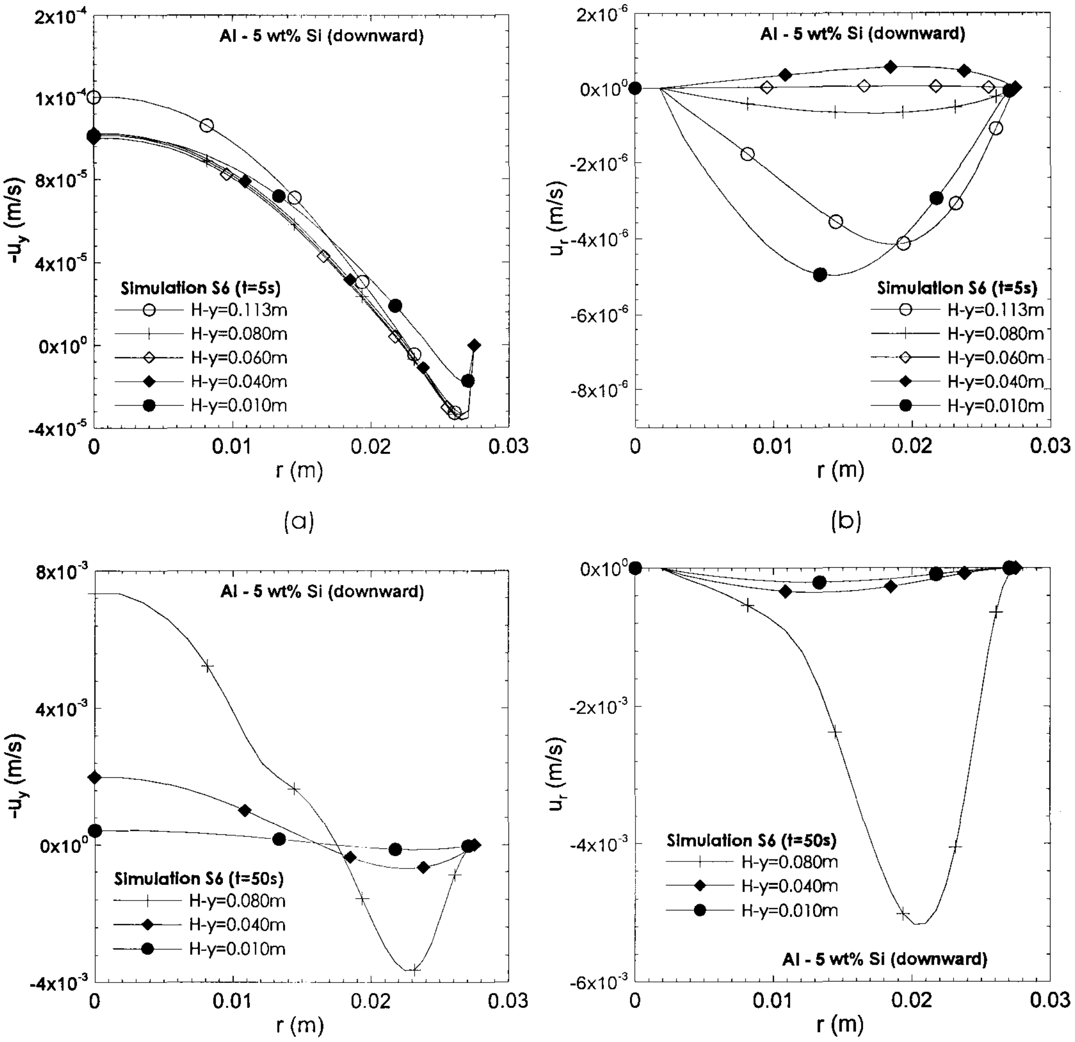

(a) (b)

(c) (d)

Figure 4: Flow velocity distribution at various locations of y during solidification simulation S6 with effect of undercooling. (a) u_y at t = 5s; (b) u_r at t = 5s; (c) u_y at t = 50s; (d) u_r at t = 50s.

Figure 5 shows the development of fluid flow of simulation S5 (no effect of ΔT on solidification). Comparing Figure 2 with Figure 5 shows that the nature of development of fluid flow dominated by shrinkage initially and subsequently dominated by natural convection are similar. However, the only difference is in the magnitude of the fluid flow velocities at the various time steps. Table 3 shows a comparison of the magnitude of fluid flow velocity between simulations S6 and S5.

Due to the absence of ΔT in S5, the temperature gradient in the liquid ahead of the mushy zone/liquid interface is always less than that in S6. Hence, the value of R in S5 is always greater than that in S6. In the beginning of solidification, the higher value of R will cause a larger effect of shrinkage on the fluid flow velocity as reflected by the higher magnitude of velocity at t=5 s in Figure 5 and Table 3. However, due to the lower temperature gradient in S5, the solute density gradient in the liquid is lower than that in S6 at t ≥ 25s, which will result in a lower fluid flow velocity due to natural convection in the liquid at any time in S5 as shown in Figure 5 and Table 3. This underestimation of fluid velocity due to natural convection in S5 as compared to S6 will greatly affect the evaluation of λ_1 as will be discussed in subsequent sections of this manuscript.

Table 3: Comparison of maximum fluid flow velocities between simulations S6 and S5.

Time (s)	**Maximum Velocity (m s^{-1})**	
	S6(with ΔT)	**S5(without ΔT)**
5	1.22×10^{-4}	1.55×10^{-4}
25	4.1×10^{-3}	2.43×10^{-3}
50	7.97×10^{-3}	5.93×10^{-3}
75	8.73×10^{-3}	6.68×10^{-3}
100	7.38×10^{-3}	5.73×10^{-3}

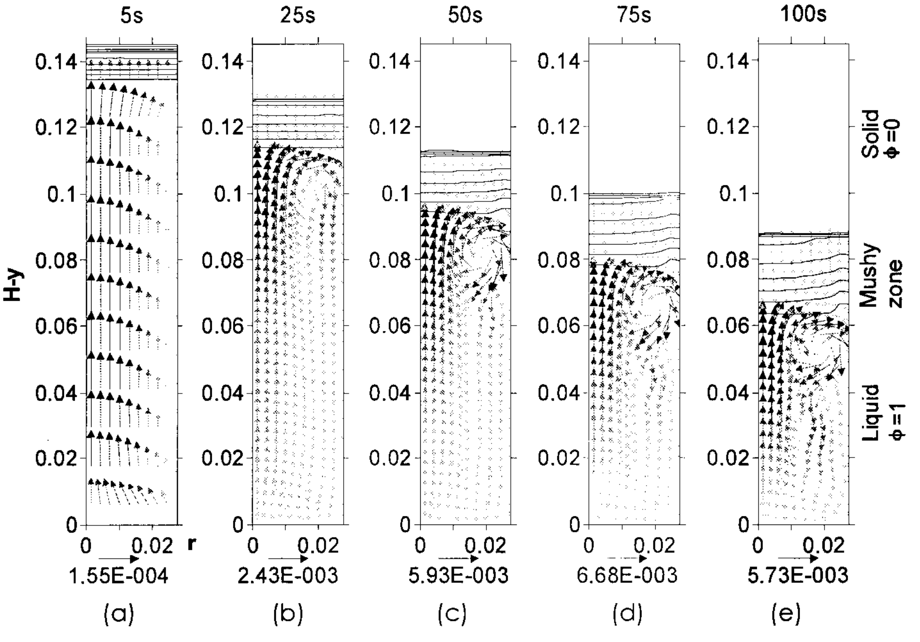

Figure 5: Development of fluid flow velocities (m.s^{-1}) during solidification simulation S5 without effect of ΔT for t = (a)5s; (b)25s; (c)50s; (d)75s; and (e)100s. The magnitudes of maximum velocities are presented at the bottom of (a) to (e), respectively.

The normalized iso - stream function lines without the effect of ΔT for simulation S5 are shown in Figure 6. Figure 6(a) to Figure 6(e) show snap shots of the normalized iso-streamlines in the computing domain at increasing solidification times of 5, 25, 50, 75, 100s, respectively. Maximum magnitude of stream function is shown below each snap shot figure for the respective times. The difference between the flow field shown in Figure 6 (without effect of

ΔT) and that shown in Figure 3 (with effect of ΔT) is best indicated by the difference in the maximum magnitude of the respective stream functions. As shown in Figure 6(a) and Figure 3(a), higher magnitude of stream function for simulation S5 implies stronger fluid flow at t = 5s. After initial stage of solidification, results from simulation S6 always have higher magnitude of maximum stream function due to the stronger buoyancy flow caused by higher density gradient in the liquid region with ΔT. The weaker fluid flow due to the negligence of the effect of ΔT in solidification (Figure 6) results in a significant delay in the development of the secondary circular flow cell in the liquid when compared to the simulation S6 with the effect of ΔT (Figure 3).

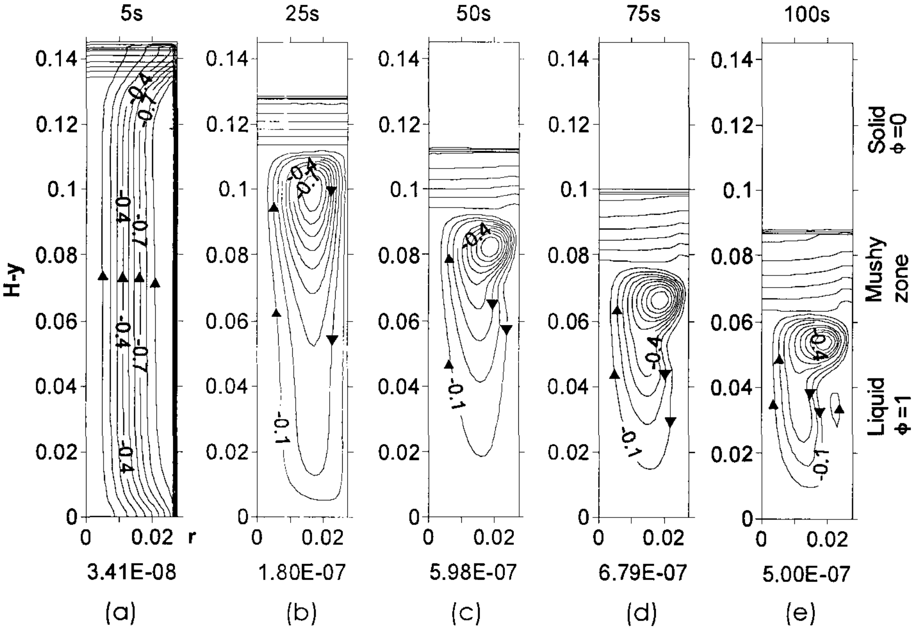

Figure 6: Development of contours of normalized stream function during solidification simulation S5 without effect of ΔT for t = (a)5s; (b)25s; (c)50s; (d)75s; and (e)100s. The magnitudes of maximum stream function ($m^3.s^{-1}$) are presented at the bottom of (a) to (e), respectively.

Figure 7(a) to Figure 7(d) show velocity distribution in both y and r directions at t =5s and t = 50s for simulation S5, respectively. Distribution of velocities in either r or y direction in Figure 7 is similar to the results shown in Figure 4. It is found that higher magnitudes of velocity could be obtained in simulation S5 at t = 5s. However, stronger fluid flow can be observed at t =50s in simulation S6.

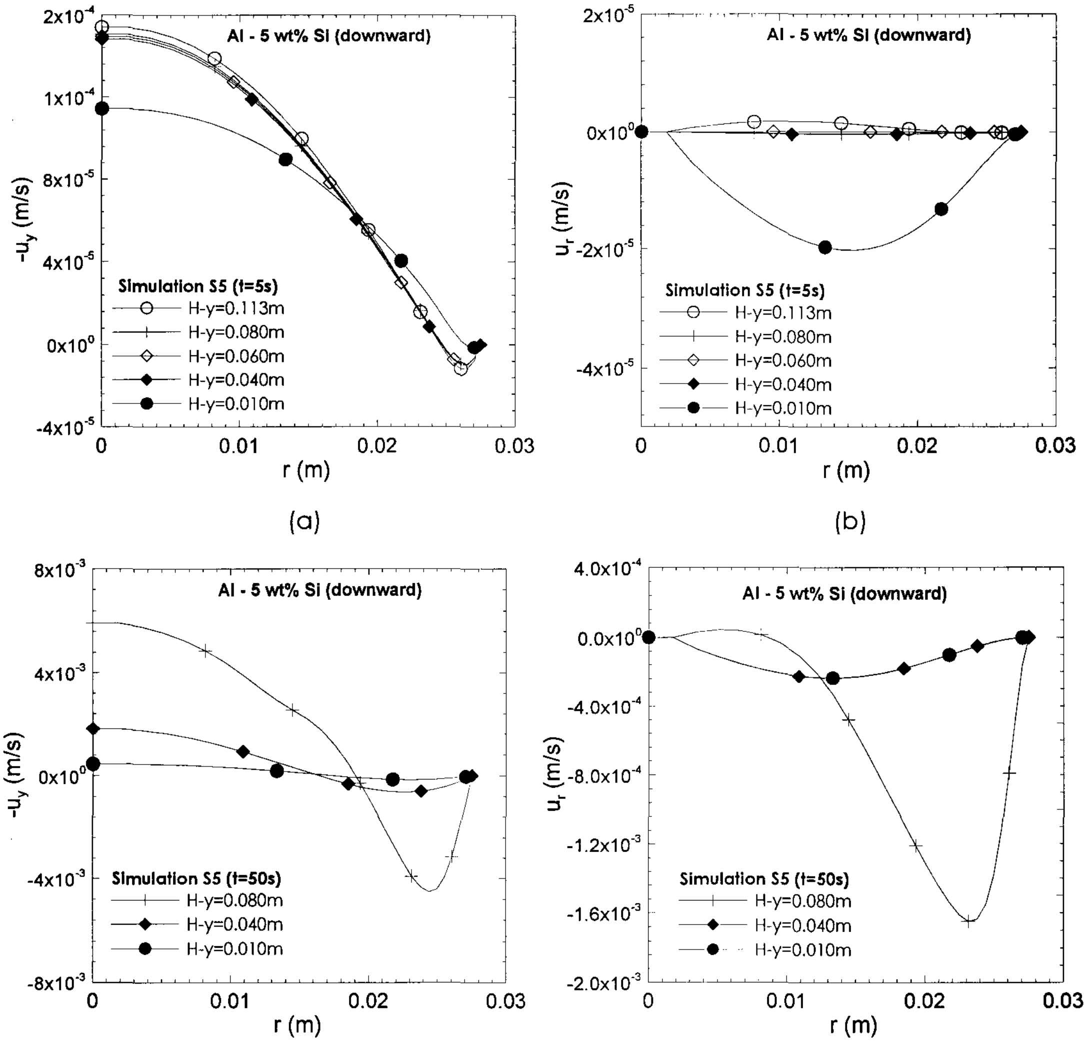

(a) (b)

(c) (d)

Figure 7: Flow velocity distribution at various locations of y during solidification simulation S5 without effect of ΔT. (a) u_y at t = 5s; (b) u_r at t = 5s; (c) u_y at t = 50s; (d) u_r at t = 50s.

Figure 8(a) to Figure 8(d) show the distribution of fluid flow velocity for simulation S8 and Figure 8(e) to Figure 8(h) show that for simulation S7. The comparison of velocity distributions between S8 and S7 is similar to that observed in S6 and S5. With the same line of reasoning as presented for S6 and S5, it can be observed that when ΔT is not considered during solidification (S7) the maximum velocity at the beginning of solidification is almost the same as that with ΔT (S8) (compare Figure 8(a) and Figure 8(e)) because fluid flow induced by shrinkage dominates over that induced by natural convection. However, at larger time intervals, the velocities of S7 are lower than that of S8 because the effect of natural convection is more on the fluid flow velocities due to ΔT (compare Figure 8(b) to (d) with Figure 8(f) to (h), respectively).

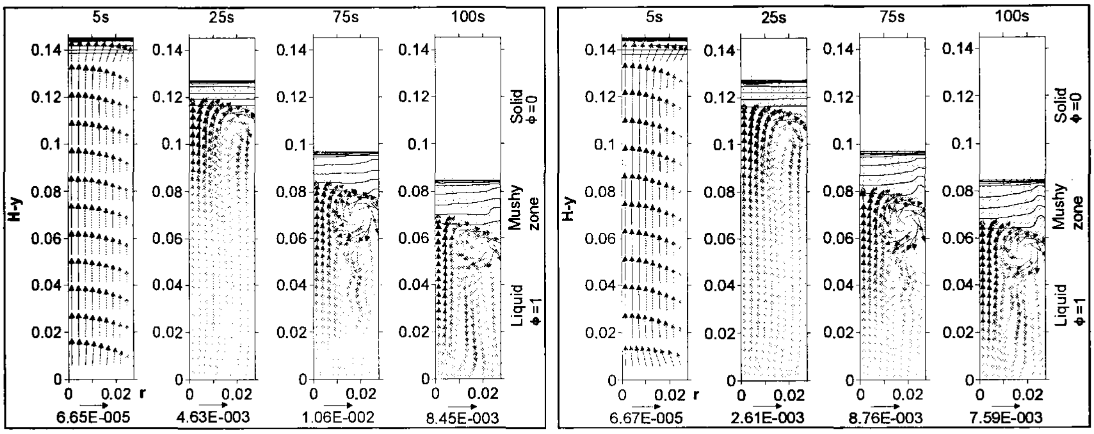

(a) (b) (c) (d) (e) (f) (g) (h)

Figure 8: Development of fluid flow velocities (m.s^{-1}) during solidification of Al-wt7%Si alloy. (a) to (d) are results for simulation S8 with effect of undercooling for t = 5s, 25s, 75s and 100s, respectively, and (e) to (h) are results for simulation S7 without the effect of undercooling for t = 5s, 25s, 75s and 100s, respectively. The magnitudes of maximum velocities are presented at the bottom of (a) to (h), respectively.

Effect of Undercooling on G

Figure 9 shows the distribution of the temperature gradient, G in the liquid ahead of the mushy zone/liquid interface. There are two main reasons for the decrease in the value of G with increasing solidification time: one is the decrease in the heat flux at the heat extraction boundary with time and the other is the decrease in the bulk temperature of liquid with time. Figure 9 (a) and Figure 9(b) are the results for simulations Al-3wt%Si (S1 and S2) and Al-7wt%Si (S3 and S4) alloys, respectively; and Figure 9(c) and Figure 9(d) are for Al-5wt%Si (S5 and S6) and Al-7wt%Si (S7 and S8) alloys, respectively. Since, the temperature of the mushy zone/liquid interface will be lower when we consider the undercooling, ΔT, the value of G is higher for the solidification simulations with the effect of ΔT included (S2, S4, S6 and S8) than that in those without the effect of ΔT (S1, S3, S5 and S7) for the respective alloys. In Figure 9(a) and Figure 9(b) (upward solidification), at the beginning of solidification, at low values of y in both alloys, a larger value of R will result in a larger value of ΔT (as given by Equation (3)) and hence, a higher value of G. In Figure 9(c) and Figure 9(d) (downward solidification), there seem to be three distinct regions from the beginning to end of solidification. These regions are marked by line segments AB, BC and CD in all the curves in Figure 9(c) and Figure 9(d). Table 4 presents the four locations A, B, C and D of the mushy zone/liquid interface, solidification times, maximum fluid flow velocity, variation of fluid flow velocity from previous location and the temperature gradient, G in the liquid at the mushy zone/liquid interface at each location.

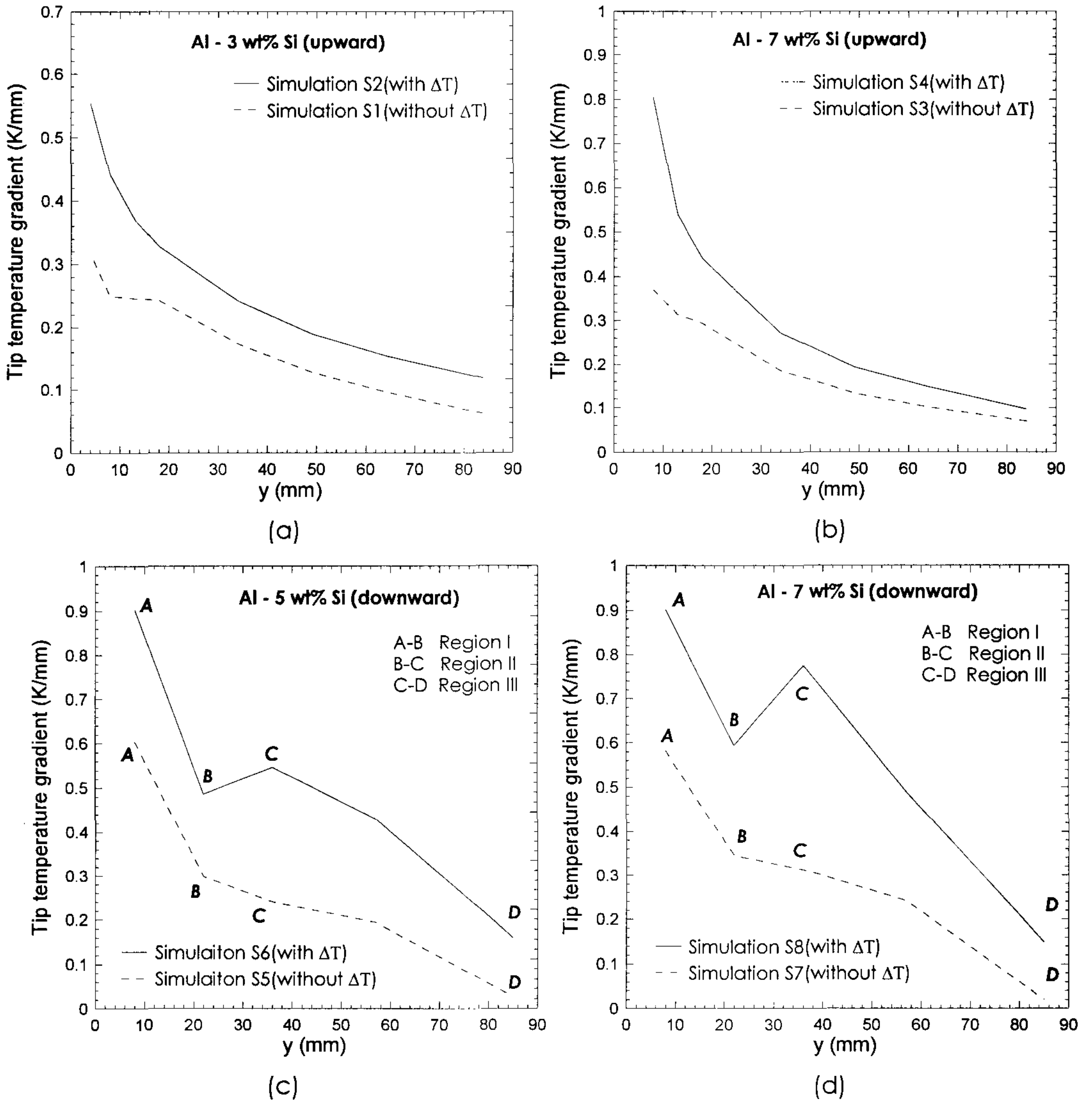

Figure 9: Effect of the undercooling on tip temperature gradient during solidification. (a) 3% upward; (b) 7% upward; (c) 5% downward; (d) 7% downward.

As discussed in the previous section on the effect of ΔT on fluid flow during downward solidification (refer to Figure 2 to Figure 8 and Table 4), the fluid flow in the initial stages of solidification as defined by line segment AB is dominated by shrinkage. Between points A and B, the decrease in G is only due to the decrease in the heat extraction rate between these locations. Between points B and C, the strong positive density gradient develops against the direction of the gravity vector and causes a significant increase in the fluid flow velocity due to natural convection. In simulation S5 (no ΔT) the change in the velocity between B and C is 557% and that in S6 (with ΔT) is much higher at 1109% because the consideration of ΔT will enhance the fluid flow velocities due to larger density gradients. This significant increase in velocity between B and C in both S5 and S6 will cause a reduction in the magnitude of the gradient of G (Figure 9(c) and Table 4). In S6, the velocity change is so drastic due to added effect of ΔT and there is an increase in the value of G between locations B and C. The same argument can be made for the change in G between locations B and C for simulations S7 and S8 as well (Figure 9d and Table 4).

Table 4: Locations A, B, C and D shown in Figure 9(c) and Figure 9(d) along with the solidification parameters at each location.

Simulation	**ΔT**	**Interface Location y (mm)**	**Solidification Time (s)**	**Maximum Fluid Flow Velocity (mm.s^{-1})**	**Variation in Maximum Velocity**	**G (K.mm^{-1})**
S5 (Al-5wt%Si)	0	8(A)	2	0.16	none	0.6
		22(B)	11	0.37	131%	0.3
		36(C)	25	2.43	557%	0.24
		85(D)	97	5.95	145%	0.03
S6 (Al-5wt%Si)	Equation (3)	8(A)	3.2	0.16	none	0.9
		22(B)	14.4	0.47	194%	0.49
		36(C)	30.3	5.68	1109%	0.55
		85(D)	108.9	6.95	22%	0.16
S7 (Al-7wt%Si)	0	8(A)	3.6	0.07	none	0.58
		22(B)	13	0.68	871%	0.34
		36(C)	27	3.03	346%	0.31
		85(D)	95.6	7.65	152%	0.02
S8 (Al-7wt%Si)	Equation (3)	8(A)	5.4	0.07	none	0.9
		22(B)	16.8	0.99	1314%	0.6
		36(C)	32.8	10	910%	0.77
		85(D)	107.3	8.35	-17%	0.15

Effect of Undercooling on R

Figure 10 shows the distribution of the solidification velocity, R at r = 0 and various location of y = 0 to 84 mm in the computing domain (refer to Figure 3 in Part I). The value of R was estimated by the velocity of the mushy zone/liquid interface during solidification. Figure 10 shows the value of the velocity of the mushy zone/liquid interface (ϕ~0.999) velocity, R. Figure 10(a) to Figure 10(d) show the results for solidification simulation for Al-3wt% (upward), Al-7wt%Si (upward), Al-5wt%Si (downward) and Al-7wt%Si (downward), respectively. Figure 10 shows that for all the simulations transient value of R decreases with increasing distance from the heat extraction interface because the magnitude of heat flux at the heat extraction boundary and the computing domain decreases with time as the volume of the solid phase increases.

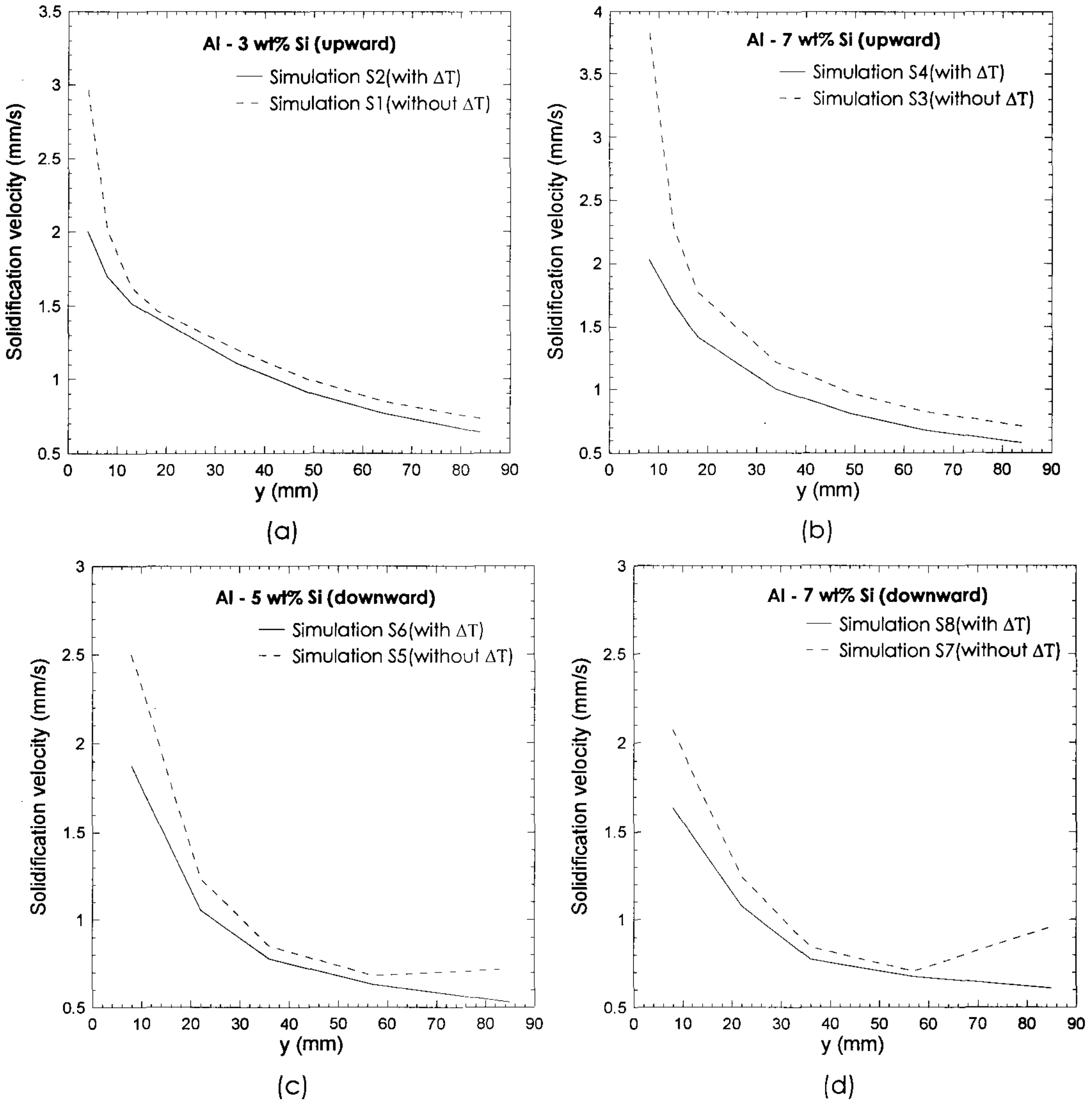

(a) (b)

(c) (d)

Figure 10: Effect of the undercooling on transient velocity (mm.s^{-1}) of the mushy zone/liquid interface during uni-directional solidification for simulation (a) S1 and S2; (b) S3 and S4; (c) S5 and S6; and (d) S7 and S8.

In all results shown in Figure 10, the value of R evaluated with the effect of ΔT is always lower than that without the effect of ΔT because the introduction of ΔT will require a lower temperature for the solidification than the T_{liq} which will cause a delay in the solidification event. The value of R is high at the beginning of solidification for all the simulations in Figure 10. Higher value of R will introduce higher ΔT which will require longer solidification times. Hence, the effect of undercooling on R is more pronounced at the earlier stages of solidification. In Figure 10 from (a) to (d), the maximum deviation in the estimated value of R at 8 mm from the heat extraction interface are 18%, 89%, 33% and 26%, respectively. In Figure 10(c) and Figure 10(d), the value of R for simulations S5 and S7 (no ΔT) increase towards the end of solidification of the computing domain because, without the effect of ΔT, the value of G will decrease towards the end of solidification and the pronounced fluid flow (downward solidification) will further enhance the rate of decrease of G and result in an increase in R (between y =58 mm to y=84 mm). Without the strong fluid flow induced by natural convection (upward solidification) in S1 and S3 (Figure 10(a) and Figure 10(b)), the value of G will not decrease enough to cause an increase in R. If one considers the effect of ΔT during solidification as in simulations S6 and S8 in Figure 10(c) and Figure 10(d), the value of G will be greater than those without the effect of ΔT, as shown in Figure 9(c) and Figure 9(d), and will not decrease so low to as to increase the value of R.

Effect of Undercooling on the Estimation of λ_1

Figure 11(a) and Figure 11(b) show the distribution of the primary dendrite arm spacing, λ_1 as a function of cooling rate (G.R) of the liquid at the mushy zone/liquid interface. It can be observed that there is no significant change in the value of (G.R) between the simulations with the effect of ΔT (simulations S2 and S4) and that without (S1 and S3), respectively because the effect of ΔT will increase the value of G but simultaneously decrease the value of R and hence the product (G.R) will remain fairly unchanged. Also shown in Figure 11(a) and Figure 11(b) are the values of λ_1 from the experiments in upward solidification from Peres et al [24]. It can be seen that simulations S1 to S4 predict the respective values of λ_1 with a reasonable accuracy. There is a slight under-prediction of the value of λ_1 because of a combination of two reasons: the model (Equations (1) and (2)) itself is semi-empirical for an unsteady state solidification process and hence may tend to over-predict or the cooling rates of the mushy zone/liquid interfaces were measured after the liquidus temperature was recorded by the thermocouples in the experiment [24] and the magnitude of this value will be higher than the actual cooling rate at the mushy zone/liquid interface and will result in an over-prediction of (G.R) in the experiments, as shown in Figure 11(a) and Figure 11(b). If the value of (G.R) is being over-predicted by the experiment results, then, the value of λ_1 should be under-predicted (Equation (1)) as it is shown as function of location (Figure 12(a)) for simulations S1 and S2. In Figure 12(a), the value of (G.R) at any specific location (refer to Figure 3 in Part 1) will be higher when the effect of ΔT is considered than that without the effect. Hence, the value of λ_1 obtained at any specific location will be lower in simulations with the effect of ΔT than in those without the effect. Hence in Figure 12(a), the simulation S2 (withΔT) predicts the value of λ_1 more accurately than that by S1 (without ΔT).

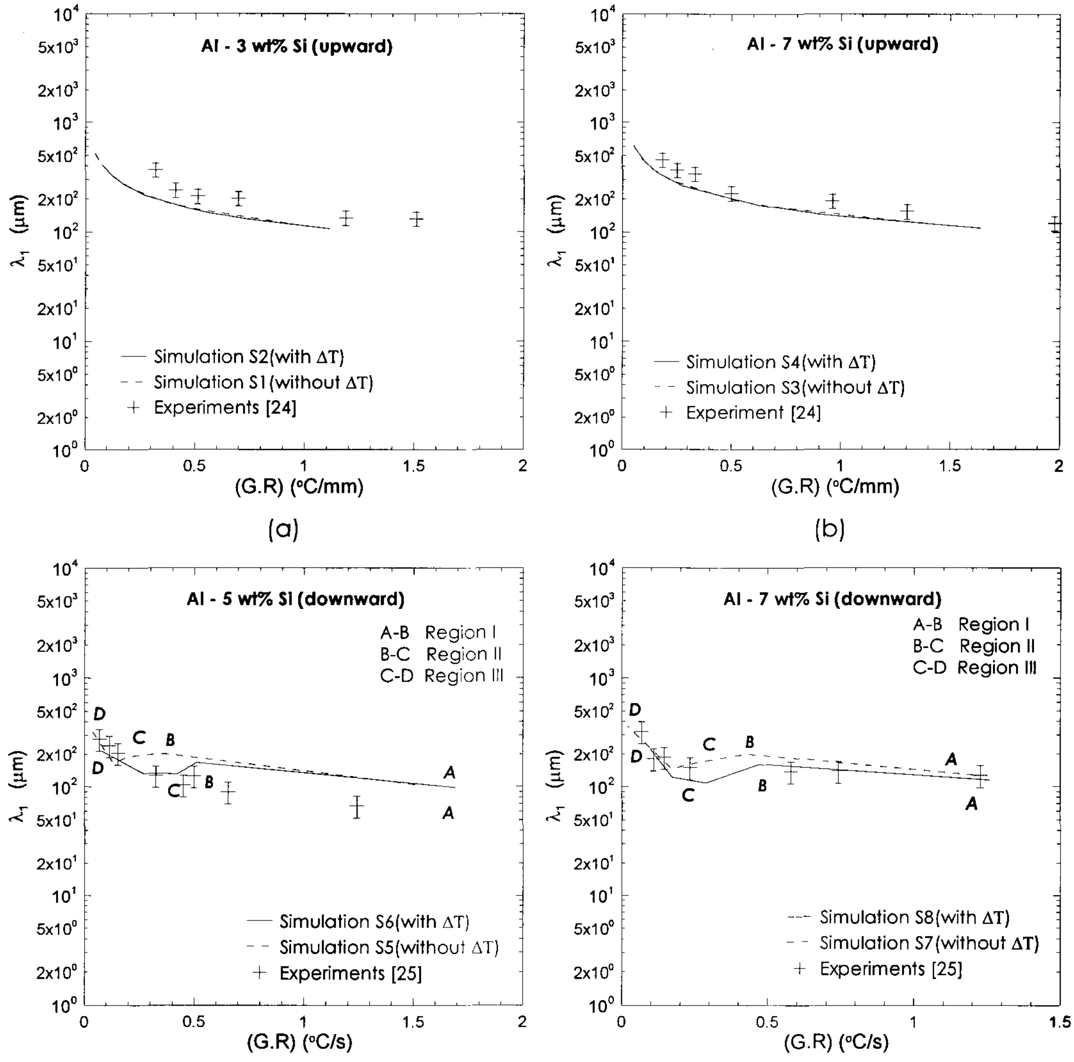

(a) (b)

(c) (d)

Figure 11: Effect of the undercooling on primary arm spacing during solidification. (a) 3% upward; (b) 7% upward; (c) 5% downward; (d) 7% downward.

Figure 11(c) and Figure 11(d) show the distribution of λ_1 as a function of (G.R) for the cases of downward solidification in simulations S5 to S8. As discussed previously about the effect of ΔT on G in the downward solidification, there are three distinct regions wherein the magnitude of the value of gradient of G decreases between the first and second regions (fluid flow dominated by the emergence of density gradient causing significant increase in fluid flow velocities than that caused by shrinkage in the first region) and again increases between the second and third regions. The trend of λ_1 will also follow the trend of G in these three regions as in Figure 11(c) and Figure 11(d). The value of λ_1 increases (G decreases) in the first region between points A and B, then, λ_1 decreases when the magnitude of gradient of G decreases in the second region between points B and C and subsequently when the fluid flow velocities due to density gradient is stabilized in the third region, the value of λ_1 again increases between points C and D in both simulations with and without the effect of ΔT. However, the effect of undercooling, ΔT, on the magnitude of the fluid flow velocities in the three regions will have a greater effect on the changes in the value of G in the three regions and hence a greater effect on the value of λ_1 as well in these regions (refer to Equation (2)). Figure 11(c) and Figure 11(d) also show that the λ_1 estimated in the experiments by Spinelli et al [25] seem to be closer to the values predicted by the simulations with the effect of ΔT included.

The values of λ_1 in the first region in alloy Al-5wt%Si (simulations S5 and S6) between points A and B seem to be under-estimated by the experiments and this may be due to various errors in the experiment evaluation of the cooling rate at the mushy zone/liquid interface and λ_1 caused by the high value of R in this region. Further, the decrease in λ_1 between points B and C can be observed from the experiment results as predicted by the simulations in Figure 11(c)[25]. Experiments will have to be carried out to obtain more data points in this region to validate the simulation results. Figure 12(a) and Figure 12(b) show the distribution of the value of λ_1 as a function of location (refer to Figure 3 in Part1) for Al-3wt%Si upward and Al-5wt%Si downward solidification, respectively. These show a better prediction of the λ_1 by the simulation with the effect of ΔT than the one without. The anomalous behaviour of the trend in λ_1 can also be observed in the second region between points B and C in Figure 12(b). It is due to the development of the higher fluid flow velocities caused by the emergence of the density gradients causing natural convection in the computing domain.

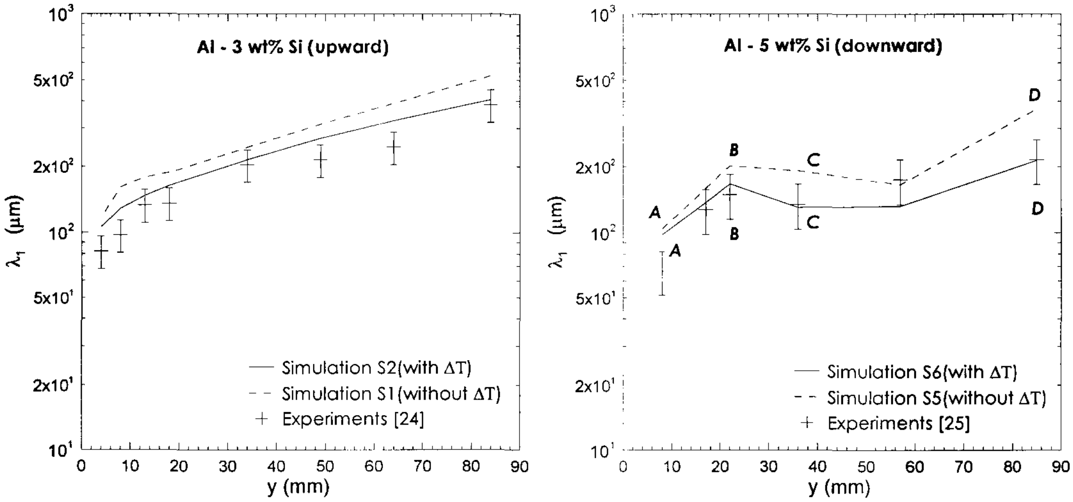

(a) (b)

Figure 12: λ_1 distribution at r = 0 mm and y ranged from 8mm to 84mm for simulations (a) S1 and S2; (b) S5 and S6.

SUMMARY AND CONCLUSIONS

Part 1 of this two-part publication presented a more efficient and valid numerical algorithm for simulation of solidification of binary alloys. In part 2, this algorithm was used to evaluate solidification parameters, such as fluid flow, G, R and λ_1 of Al-Si hypoeutectic alloys in both upward and downward solidification modes. The main conclusions of this part of the publication are presented below:

- The effect of undercooling, ΔT has a significant effect on the velocity of the fluid flow in the computing domain only in the downward solidification and there is no significant effect in the upward solidification mode because the positive density gradient is against the direction of the gravity vector in the former causes significant increase in velocities of the fluid flow due to natural convection.
- The effect of ΔT is pronounced on the distribution of the temperature gradient of the liquid at mushy zone/liquid interface, G during both upward and downward solidification modes.
- The effect of ΔT is pronounced on the distribution of the velocity of the mushy zone/liquid interface, R during both upward and downward solidification modes. The effect of ΔT is more pronounced at higher values of R and reduces with decreasing R because ΔT is high at higher values of R as a result of increased heat extraction during initial stages of solidification.
- The effect of ΔT is pronounced on the primary dendrite arm spacing in the downward solidification mode but not significant in the upward solidification mode.
- There are three distinct regions in the downward solidification mode because of significant changes in the velocity in these regions. In the first region, the fluid flow is mostly dominated by shrinkage due to solidification and coupled with the effect of undercooling, ΔT, there is a decrease in the value of G, decrease in the value of R and increase in the value of λ_1. In the second region, the emergence of the positive density against the direction of the gravity vector causes a significant increase in the flow velocity of the liquid coupled with the effect of ΔT result in a significant increase in value of G, slight decrease in the value of R and a significant decrease in the value of λ_1. In the third region, the stabilization of the flow velocity coupled with the continuous heat extraction and the effect of ΔT result in a decrease in G, decrease in R and increase in λ_1.

A viable numerical model has been proposed to include the effect of undercooling, ΔT of the liquidus temperature in numerical solidification simulations of binary alloys. Results presented in this two-part publication show that a viable numerical method is feasible to include the effect of undercooling of liquidus temperature prior to the solidification of the primary phase and that the effect of this undercooling cannot be ignored in solidification simulations of binary alloys.

REFERENCES

[1] D. P. Sekulic, P. K. Galenko, M. D. Krivilyov, L. Walker, and F. Gao, "Dendritic growth in Al–Si alloys during brazing. Part 2: Computational modeling," *International Journal of Heat and Mass Transfer,* vol. 48, pp. 2385-2396, 2005.

[2] Factsage, 5.5 ed Madison, WI, USA.: Computherm LLC.

[3] M. Gunduz and J. D. Hunt, "The measurement of solid-liquid surface energies in the Al-Cu, Al-Si and Pb-Sn systems," *Acta Metallurgica,* vol. 33, pp. 1651-1672, 1985.

[4] W. D. Bennon and F. P. Incropera, "A continuum model for momentum, heat and species transport in binary solid – liquid phase change systems - I. Model formulation," *International Journal of Heat and Mass Transfer,* vol. 30, pp. 2161-2170, 1987.

[5] W. D. Bennon and F. P. Incropera, "A continuum model for momentum, heat and species transport in binary solid – liquid phase change systems - II. Application to solidification in a rectangular cavity," *International Journal of Heat and Mass Transfer,* vol. 30, pp. 2171-2178, October 1987.

[6] W. D. Bennon and F. P. Incropera, "Numerical analysis of binary solid – liquid phase change using a continuum model," *Numerical Heat Transfer,* vol. 13, pp. 277-296, 1988.

[7] S. D. Felicelli, J. C. Heinrich, and D. R. Poirier, "Simulation of freckles during vertical solidification of binary alloys," *Metallurgical Transactions B (Process Metallurgy),* vol. 22, pp. 847-859, Dec. 1991.

[8] S. D. Felicelli, J. C. Heinrich, and D. R. Poirier, "Numerical models for dendritic solidification of binary alloys," *Numerical Heat Transfer, Part B: Fundamentals,* vol. 23, pp. 461-481, 1993.

[9] J. C. Heinrich and D. R. Poirier, "The effect of volume change during directional solidification of binary alloys," *Modeling and Simulation in Materials Science and Engineering,* vol. 12, pp. 881-899, Sep. 2004.

[10] E. McBride, J. C. Heinrich, and D. R. Poirier, "Numerical simulation of incompressible flow driven by density variations during phase change," *International Journal for Numerical Methods in Fluids,* vol. 31, pp. 787-800, Nov. 1999.

[11] V. R. Voller and C. Prakash, "Fixed grid numerical modeling methodology for convection - diffusion mushy region phase – change problems," *International Journal of Heat and Mass Transfer,* vol. 30, pp. 1709-1719, 1987.

[12] J. A. E. Bell and W. C. Winegard, "Dendrite Spacing in Tin-Lead Alloys," *J. Inst. Met.,* vol. 93, pp. 357-359, 1963.

[13] D. Bouchard and J. S. Kirkaldy, "Prediction of dendrite arm spacings in unsteady- and steady-state heat flow of unidirectionally solidified binary alloys," *Metallurgical and Materials Transactions B (Process Metallurgy and Materials Processing Science),* vol. 28B, pp. 651-663, Aug. 1997.

[14] A. Geying and L. Lixin, "Dendrite spacing in unidirectionally solidified Al-Cu alloy," *Journal of Crystal Growth,* vol. 80, pp. 383-392, 1987.

[15] J. D. Hunt, "Solidification and casting of metals," *Proceedings of the International Conference on Solidification and Casting of Metals, The Metals Society, London,* pp. 3-9, 1979.

[16] J. D. Hunt and S.-Z. Lu, "Numerical modeling of cellular/dendritic array growth: spacing and structure predictions," *Metallurgical and Materials Transactions A: Physical Metallurgy and Materials Science,* vol. 27A, pp. 611-623, Mar. 1996.

[17] W. Kurz and D. J. Fisher, "Dendritic growth and limit of stability tip radius and spacing," *Acta Metall.,* vol. 29, pp. 11-20, 1981.

[18] J. T. Mason, J. D. Verhoeven, and R. Trivedi, "Primary dendrite spacing. I. Experimental studies," *Journal of Crystal Growth,* vol. 49, pp. 516-524, Oct. 1982.

[19] D. G. McCartney and J. D. Hunt, "Measurements of cell and primary dendrite arm spacings in directionally solidified aluminium alloys," *Acta Metallurgica,* vol. 29, pp. 1851-1863, Nov. 1981.

[20] Y. Miyata, T. Suzuki, and J. I. Uno, "Cellular and dendritic growth I. Experiment," *Metallurgical Transactions A (Physical Metallurgy and Materials Science),* vol. 16A, pp. 1799-1805, 1985.

[21] K. Somboonsuk and R. Trivedi, "Interdendritic spacing. I. Experimental studies," *Metallurgical Transactions A (Physical Metallurgy and Materials Science),* vol. 15A, pp. 967-975, 1984.

[22] R. Trivedi, "Interdendritic spacing: part II. A. comparison of theory and experiment," *Metallurgical Transactions A (Physical Metallurgy and Materials Science),* vol. 15A, pp. 977-982, 1984.

[23] P. Lehmann, R. Moreaub, D. Camela, and R. Bolcatob, "A simple analysis of the effect of convection on the structure of the mushy zone in the case of horizontal Bridgman solidification. Comparison with experimental results," *Journal of Crystal Growth,* vol. 183, pp. 690-704, 1998.

[24] M. D. Peres, C. A. Siqueira, and A. Garcia, "Macrostructural and microstructural development in Al-Si alloys directionally solidified under unsteady-state conditions," *Journal of Alloys and Compounds,* vol. 381, pp. 168-181, November 3 2004.

[25] J. E. Spinelli, M. D. Peres, and A. Garcia, "Thermosolutal convective effects on dendritic array spacings in downward transient directional solidification of Al-Si alloys," *Journal of Alloys and Compounds,* vol. 403, pp. 228-238, Novermber 2005.

OPTIMIZATION OF MATERIAL PROPERTIES IN SOLIDIFICATION SIMULATION OF Al-Si BINARY ALLOY

Hongda Wang[1,2], Sumanth Shankar[1], Mohamed S. Hamed[2,*]
[1]Light Metal Casting Research Centre (LMCRC)
[2]Thermal Processing Laboratory (TPL)
McMaster University, Hamilton, ON, Canada L8S 4L7

ABSTRACT

The challenges in the numerical simulation of the solidification of binary alloys are not only in the complexity of the algorithms themselves, but also in the validity of the data used to define the material properties of the various phases to facilitate the validation of the simulation results by experiments. The effect of material properties on the numerical simulations was investigated in the present study where in the Al- 3 wt% Si hypoeutectic binary alloy was solidified such that the solidification front travelled against the gravity vector (upward solidification). The effect of shrinkage was not considered in the simulation because fluid flow due to shrinkage had negligible effect on the solidification parameters in the upward solidification mode. Energy and concentration equations were solved by using the finite-volume method and coupled with local equilibrium assumptions inside mushy zone between temperature and liquid concentration to evaluate liquid fraction. Effect of specific heat of solid and thermal conductivity of solid on transient temperature distribution and solidification time at mushy zone/liquid interface was investigated. Further, the effect of density of solid, solute diffusivity coefficient of liquid on solidification time was studied as well. It was found that certain properties such as specific heat and thermal conductivity could not be assumed constant in the solid phase. However, most properties in the liquid phase could be assumed constant. These properties have been enumerated and quantified. Numerical simulations have been carried out with a new algorithm that was developed to include the effect of undercooling of the liquid temperature prior to the solidification event. Numerical results for transient temperature distribution and solidification time at the mushy zone/liquid interface using the optimum set of material properties were validated by experiments.

NOMENCLATURE

c_{ps}	Specific heat of solid as a function of temperature (J Kg^{-1} K^{-1}) [1];
c_{pl}	Specific heat of liquid (J Kg^{-1} K^{-1}) [1];
C_L	Liquid concentration (wt%);
C_o	Average alloy composition (wt%);

---

* Corresponding Author: hamedm@mcmaster.ca , voice: (905) 525-9140 X 26113

C_s	Solid concentration (wt%);
D	Solute diffusivity coefficient of liquid (6.25 × 10^{-9} ($m^2 s^{-1}$)) [2];
G	Temperature gradient in liquid at the liquid-mushy zone interface (K mm^{-1});
k	Average partition coefficient (0.116) [3];
K_s	Thermal conductivity of solid as a function of temperature (W m^{-1} K^{-1}) [1];
K_l	Thermal conductivity of liquid (W m^{-1} K^{-1}) [1];
L	Latent heat of fusion (J Kg^{-1}) [3];
m	The slope of liquidus line (– 6.675 (K $wt\%^{-1}$)) [3];
R	Velocity of liquid-mushy zone interface (mm s^{-1});
t	Time (s);
T	Temperature (°C);
T_{liq}	Liquidus temperature (°C) [3];
T_{ini}	Initial temperature of liquid (°C);
T_m	Melting temperature of pure aluminum (660 °C) [3];
T_{eut}	Eutectic temperature (578.6 °C) [3];
$T_{ambient}$	Temperature of cooling water (°C);
ΔT	Undercooling of T_{liq} (°C);
ρ_l	Liquid density (Kg m^{-3}) [1];
ρ_s	Solid density as a function of temperature (Kg m^{-3}) [1];

INTRODUCTION

Aluminum (Al) alloys are finding newer applications everyday due to its attractively high strength to weight ratio, which enables production of low weight parts with high mechanical strength. An increased demand of the use of Al alloys in a variety of applications ranging from common household products to the technologically challenging automotive and aerospace components has warranted a more thorough understanding of their solidification characteristics. [4]

In our earlier work [4], we have presented a new numerical algorithm which enables the inclusion of the undercooling of liquidus temperature prior to the solidification event, ΔT in the solidification simulation. Further, this algorithm also enables a more robust formulation for the evaluation of the liquid fraction in the mushy zone (region where liquid and solid phases co-exist during solidification of binary alloys) and further saves nearly half the computing cost.

The numerical algorithm forms an important component in the success of the solidification simulation. Another critical component is the data for material properties applied for the liquid and solid phases used in the simulation. All solidification simulations carried out thus far in this field have used constant specific value for each of the material properties in the solid and liquid phases, respectively. A few examples of the material properties discussed herein are thermal conductivity, specific heat capacity, density and mass diffusivity of the solute atoms in both the solid and liquid phases, respectively.

In this study, simulations were carried out to evaluate the effect of considering these material properties as constants on the resultant solidification parameters such as transient temperature distribution during solidification and solidification times (location of the liquid-mushy zone interface during solidification). The simulation was setup to duplicate the experiment conditions of [5] wherein upward solidification (velocity of liquid/mushy zone interface is against the direction of the gravity vector) of Al-3wt% Si alloy was carried out. The fluid flow in this case was wholly caused by solidification shrinkage and had negligible effect on the solidification parameters [6] and hence was not considered in the simulation. It was found that material properties in the liquid phase showed insignificant variation and hence these properties can be assumed as constant. However, material properties in the solid phase have significant variation as a function of temperature and most of these properties should not be assumed constant for successful solidification simulation of binary alloys. The Al-3wt%Si alloy was used as an example system in this study.

BACKGROUND

Voller et al [7] proposed a numerical algorithm based on the single enthalpy formulation for simulating solidification of binary alloys. Material properties of the solid and liquid phases were assumed identical to each other. No validation was reported from experiments.

Bennon et al [8-10] proposed a numerical algorithm to simulate NH_4CL-H_2O alloy solidification using uniform forms of the concentration and energy equations in all three zones (solid, liquid and mushy). The energy and the concentration equations were solved independently. Material properties, such as specific heat, thermal conductivity and density, were assumed to be constant for both liquid and solid phase in [9, 10].

Felicelli et al [11, 12] proposed a numerical algorithm for simulating solidification of binary alloys. Similar to the algorithm by Bennon et al [8-10], both the concentration and energy equations were considered. The energy equation in the mushy zone was treated differently by substituting the concentration equation into the energy equation. Solute diffusivity inside the solid phase was assumed to be absent. Felicelli et. al. [12] reported numerical results of their algorithm by simulating solidification of binary NH_4CL-H_2O and Pb-Sn alloys. Thermal properties such as specific heat capacity and thermal conductivity of NH_4CL-H_2O, were assumed constant for solid and liquid phases alike. Thermal properties of Pb-Sn were assumed identical for liquid and solid phases as well. This algorithm [11] was further developed by Mcbride et.al. [13], considering density variations between solid and liquid phases (shrinkage). Thermal diffusivity and thermal conductivity, however, were assumed identical for all phases. Heinrich and Poirier [14] corrected flow velocities during solidification at eutectic temperature. Thermal properties were assumed constant for both solid and liquid phases, individually. All the above mentioned numerical methods [7-14] for alloy solidification were focusing on improving the numerical algorithm and were not critical about the effect of the variation of material properties on the results of the solidification simulations.

The new algorithm proposed by Wang et al [4] included the effect of undercooling of the liquidus temperature prior to the solidification event, ΔT in the numerical simulation. This was possible by evaluating the liquid fraction, ϕ, by solving the energy equation in the entire mushy zone. This method also circumvented the instability problem posed by the phase transformation term in the energy equation by solving the concentration equation prior to the energy equation [4]. Materials properties for the Al-3wt% Si in solid phase were obtained as a function of temperature from the commercial thermodynamic simulation software, JMatPro™ [1] which evaluates properties from fundamentals and experiment results.

DOMAIN DEFINITION

The computing domain was that of upward solidification (velocity of liquid-mushy zone interface is against the direction of gravity vector) wherein an Al-3 wt%Si alloy with an initial superheat temperature of 2 °C above the liquidus temperature of 642 °C was assumed in a cylindrical container as shown in Figure 1. Figure 1 also shows the boundary conditions in the computing domain. The cylinder diameter and height were 55 mm and 145 mm, respectively. During upward solidification simulation, the density of the liquid at the bottom is greater than that at the top [4], hence, no natural convection will occur during solidification. In order to accentuate the effect of material thermo-physical properties, the effect of shrinkage was also neglected as it had no significant effect on the results of solidification [4]. Therefore, the present solidification process is diffusion dominated wherein the heat would be diffused only from the bottom, and uni-directional solidification would occur from the bottom to top. The effect of ΔT was considered in all the simulation [4] in this study unless otherwise mentioned.

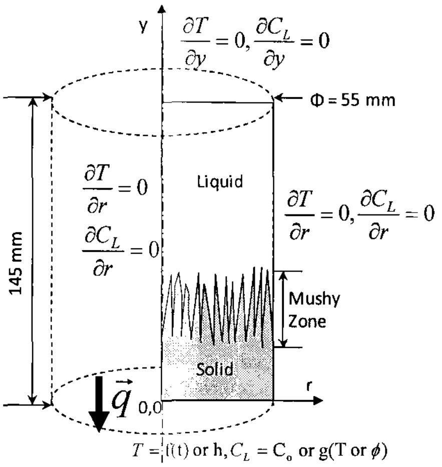

Figure 1: Boundary conditions for T and C_L and geometry of model problem.

Governing Equations

The governing equations for the simulation conditions shown in Figure 1 are presented in this section. The energy equation is presented in Equation (1) and the concentration equation in Equation (2).

$$\overbrace{\frac{\partial((\phi\rho_l c_{pl}+(1-\phi)\rho_s c_{ps})T)}{\partial t}}^{\text{Transient Term}}+\overbrace{\rho_s L\frac{\partial\phi}{\partial t}}^{\text{Phase Transformation Term}} = \underbrace{\frac{1}{r}\frac{\partial}{\partial r}\left(r(\phi K_l+(1-\phi)K_s)\frac{\partial T}{\partial r}\right)+\frac{\partial}{\partial y}\left((\phi K_l+(1-\phi)K_s)\frac{\partial T}{\partial y}\right)}_{\text{Diffusion Term}} \quad (1)$$

$$\overbrace{\frac{\partial(\phi\rho_l C_L+(1-\phi)\rho_s C_S)}{\partial t}}^{\text{Transient Term}} = -\rho_l(\underbrace{\beta C_L\frac{\partial\phi}{\partial t}}_{\substack{\text{Source Term}\\ \text{from Shrinkage}}}\underbrace{-D(\frac{1}{r}\frac{\partial}{\partial r}(\phi r\frac{\partial C_L}{\partial r}))-D\frac{\partial}{\partial y}(\phi\frac{\partial C_L}{\partial y})}_{\text{Diffusion Term}}) \quad (2)$$

Temperature of a CV in the mushy zone was determined by Equation (3) wherein local equilibrium conditions were assumed [15].

$$T = T_m + mC_L \quad (3)$$

The average solute concentration of the solid phase in a CV was evaluated by Equation (4).

$$C_S = \frac{1}{1-\phi}\int_{\phi}^{1} kC_L\,d\phi \quad (4)$$

The undercooling can be estimated by the model presented in Burden et al [16, 17] and given in Equation (5):

$$\Delta T = (\frac{GD}{R}) + \frac{\left(-8mR(1-k)C_o\Gamma\right)^{\frac{1}{2}}}{D^{\frac{1}{2}}} \quad (5)$$

The magnitude of undercooling in the present work is not a constant throughout the solidification process but is updated at every time step for each control volume (CV) in the domain.

Initial Conditions

T_{ini} = 644 °C.

$C_L = C_o$ = 0.03 mass fraction Si (Al-3wt%Si)

$C_S = C_L \times k$

ϕ = 1

Boundary Conditions

Location (mm)	**T**	**C_L**
y=0	*f(t)* was determined by experiment conditions [5] and correlated by equation (6)	$C_L = \begin{cases} C_o & T > T_{liq} - \Delta T \\ g(\phi) & T = T_{liq} - \Delta T \quad g(\phi) \text{ defined by Equation (2)} \\ g(T) & T < T_{liq} - \Delta T \quad g(T) \text{ defined by Equation (3)} \end{cases}$
y=145	$\frac{\partial T}{\partial y} = 0$	$\frac{\partial C_L}{\partial y} = 0$
r=0	$\frac{\partial T}{\partial r} = 0$	$\frac{\partial C_L}{\partial r} = 0$
r=27.5	$\frac{\partial T}{\partial r} = 0$	$\frac{\partial C_L}{\partial r} = 0$

Function f(t) was applied as boundary condition:

$$f(t) = \begin{cases} -12 \times t + 644 & (t \le 10s) \\ 637.44 - 63.08 \times \ln(t) + 198.96/\ln(t) - 8.30 \times \ln(t)^2 - 115.26/\ln(t)^2 + 0.89 \times \ln(t)^3 & (t > 10s) \end{cases} \qquad (6)$$

In the governing equations, the partition ratio, k is treated as a constant by assuming linear functions for the liquidus and solidus lines, respectively. No diffusion of solute in the solid phase was assumed because the diffusion coefficient of solute in solid is more than four orders of magnitude less than that in liquid. Therefore, average solute concentration in the solid for each CV was obtained by Equation (4).

Material Properties

Table 1 shows the extremities (maximum and minimum) of the values of material properties in the experiment conditions [5] along with the percentage variation between the maximum and minimum values. All the properties listed in Table 1 were obtained from JMatPro™[1].

Table 1: Thermo-physical properties for Al – wt 3 % Si from JMatPro™[1].

Phase	**Property**	**$T=T_{ini}$**	**$T=T_{liq}$**	**$T=T_{eut}$**	**$T=T_{ambient}$**	**Variation (%)**
Liquid	K_l ($W.m^{-1} K^{-1}$)	86	n/a	84	n/a	2.6
	c_{pl} ($J.kg^{-1} K^{-1}$)	1169	n/a	1168	n/a	0.05
	ρ_l ($kg.m^{-3}$)	2406	n/a	2428	n/a	0.9
Solid	K_s ($W.m^{-1} K^{-1}$)	n/a	170	n/a	225	24.4
	c_{ps} ($J.kg^{-1} K^{-1}$)	n/a	1211	n/a	896	26.0
	ρ_s ($kg.m^{-3}$)	n/a	2571	n/a	2687	4.3

As reported in Table 1, variation of the properties, such as density, specific heat and thermal conductivity for liquid is relatively small (<3%). Therefore, the properties for liquid phase were assumed to be constant in the present study. Table 1 shows that the properties of the solid phase have a significant variation. Hence, these properties were assumed to be function of temperature for the solidification simulation that was validated by experiment results [5] (Simulation SA). Further a variety of simulations with identical model problem, governing equations, and boundary and initial conditions were carried out with various combinations of material properties in the solid phase so as to identify the effect of the individual properties on the results of the simulation such as transient temperature distribution and solidification time.

Table 2 shows various simulations that were carried out with different combinations of material properties. The material properties of the liquid phase were assumed equal to the average between the maximum and minimum values for each property shown in Table 1. The two phase mushy zone was treated as liquid and solid phases separately and the material properties of the respective phases were assumed as mentioned above.

Table 2: Identification and details of the simulations carried out.

Simulation Identification	**Material Properties**	**Comments**	**ΔT**
SA	f(T) obtained from JmatPro™[1].	For validation by experiments [5].	ΔT is calculated from Equation (5)
S1	$K_s = 225$ (W.m^{-1} K^{-1})	Study effect of K_s	
S2	$K_s = 170$ (W.m^{-1} K^{-1})		
S3	c_{ps}=1211 (J.kg^{-1} K^{-1})	Study effect of c_{ps}	
S4	c_{ps}=896 (J.kg^{-1} K^{-1})		
S5	ρ_s=2687 (kg.m^{-3})	Study effect of ρ_s	
S6	ρ_s=2571 (kg.m^{-3})		
S7	D=6.25×10^{-8} (m^2 s^{-1})	Study effect of D	
S8	D=6.25×10^{-10} (m^2 s^{-1})		
S9	D=6.25×10^{-8} (m^2 s^{-1})		$\Delta T = 0$
S10	D=6.25×10^{-10} (m^2 s^{-1})		

In Table 2, simulation SA was carried out with the optimum values of material properties of the solid and liquid phases to enable validation by experiment results [5]. Simulation S1 to S2, S3 to S4, S5 to S6 and S7 to S10 were carried out to evaluate the effect of K_s, c_{ps}, ρ_s and D, respectively. When one of the solid properties in simulations S1 to S6 was assumed constant, the other material properties of the solid were assumed function of temperature. All the properties of the solid phase were assumed to be linear function of temperature between the maximum and minimum values shown in Table 1. The value of the diffusion coefficient of the solute in the liquid phase was obtained from Sekulic et al [2] as $D = 6.25 \times 10^{-9}$ m^2.s^{-1}. Simulations S7 to S10 were carried out to evaluate the effect of changing the value of D by two orders of magnitude for cases with and without the effect of ΔT. Simulations without the effect of undercooling were carried out only when the effect of D was evaluated because, in simulations S1 to S6 (with ΔT), the effect of the respective material properties on the solidification results did not show an appreciable change when ΔT was not considered.

NUMERICAL PROCEDURE

Figure 2 shows the flow chart outlining the details of the numerical procedure used in the solidification simulation. A detailed explanation of this procedure was presented in Wang et al [4].

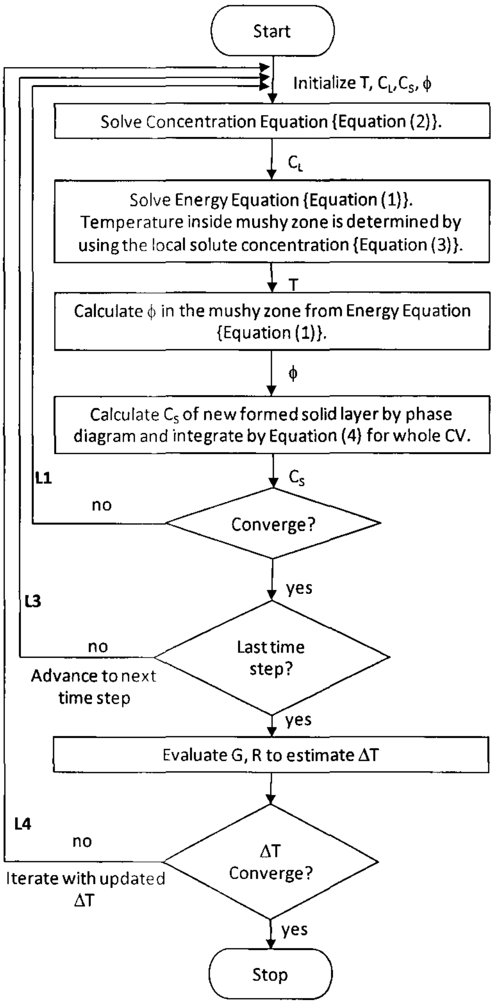

Figure 2: Numerical procedure for solidification simulation of binary alloys without any fluid flow during solidification.

RESULTS AND DISCUSSION

The results and discussion of the effects of the material properties on the transient temperature distribution and solidification time (location of liquid-mushy zone interface) will be presented on the following topics:

- Validation of the numerical model.
- Effect of K_s
- Effect of c_{ps}
- Effect of ρ_s
- Effect of D

Validation of the Numerical Model

Figure 3(a) and Figure 3(b) show the validation of the transient temperature distribution and solidification time (location of liquid-mushy zone interface with time during solidification), respectively. Figure 3 shows that there is good agreement between the results of the numerical simulation SA and the experiments [5]. Figure 3(a) shows that the agreement between simulation SA and the experiment is better at the beginning of the solidification and the simulation slightly over-predicts the transient temperature towards the final stages of solidification. One viable reason for this may be the loss of uni-directionality in the heat transfer mode in the experiments towards the final stages of solidification, which was assumed in the simulation to exist during the entire solidification process. In Figure 3(b) the gradient of the curve presents the value of the liquid-mushy zone interface velocity, R at any given location, y at r=0.

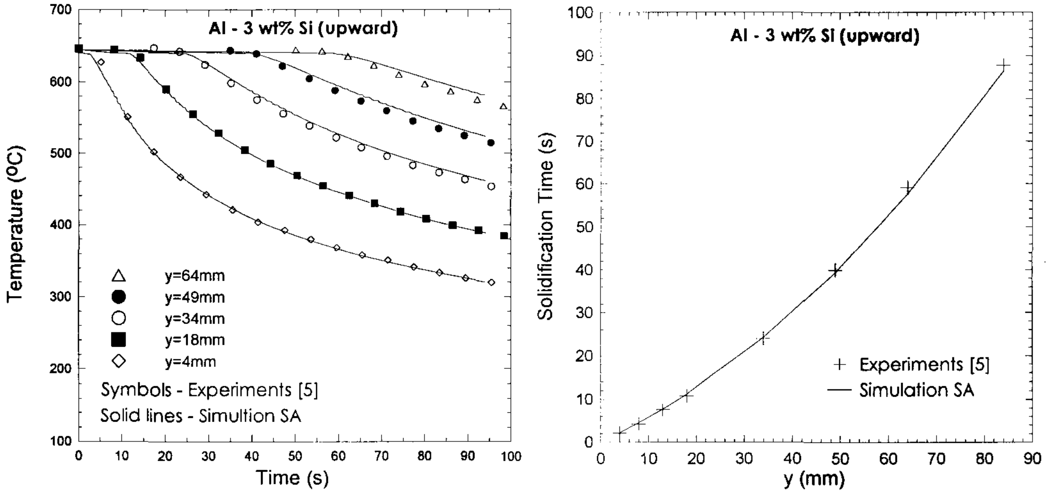

(a) (b)

Figure 3: Validation of simulation SA by experiment results [5]. (a) Transient temperature distributions at r = 0mm and y = 4, 18, 34, 49, and 64mm away from heat extraction interface. (b) Solidification time determined by the location of the liquid-mushy zone interface at the centre of the cylinder (r = 0).

Effect of K_s

Figure 4 (a) and Figure 4(b) show the effect of the two extreme values of K_s (minimum (S2) and maximum (S1)) as shown in Table 1 and Table 2 on the transient temperature distribution and the solidification time, respectively. It is evident from Figure 4 that the magnitude of K_s has a significant impact on the numerical results. The maximum value of K_s resulted in a higher heat flux through the solid phase and hence increased the velocity of the liquid-mushy zone interface, R resulting in increase of the cooling rate at the interface, (G.R). Hence, the use of the maximum value of k_s shows a progressively lower transient temperature at any given time (Figure 4 (a)) and decreases the solidification time (Figure 4 (b)) when compared to the case of using the minimum value. The maximum value of K_s results in a 20% decrease in total solidification time, at y=84 mm, as compared to the minimum value of k_s.

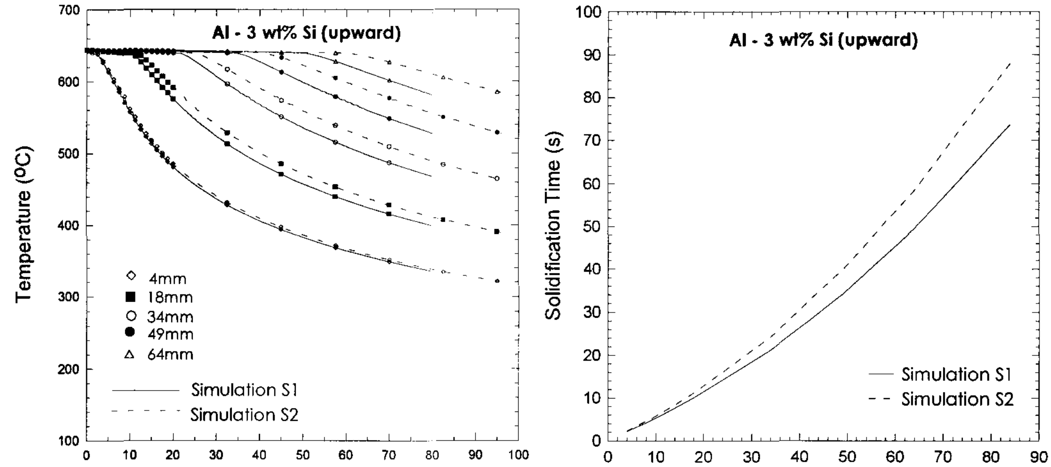

(a) (b)

Figure 4: Effect of the value of thermal conductivity of solid phase, K_s on transient temperature distribution and on solidification time for S1 (Maximum K_s) and S2 (Minimum K_s). (a) transient temperature distributions at r = 0 for various locations: y = 4, 18, 34, 49, 64 mm and (b) Solidification time determined by the location of the liquid-mushy zone interface at the centre of the cylinder (r = 0).

Effect of c_{ps}

Figure 5(a) and Figure 5(b) show the effect of the two extreme values of c_{ps} (minimum (S4) and maximum (S3)) as shown in Table 1 and Table 2 on the transient temperature distribution and the solidification time, respectively. Simulation carried out with the maximum value of c_{ps} (S3) shows lower transient temperatures at any given time (Figure 5(a)) and lower value of solidification time at any given location (Figure 5(b)). The solidification time predicted using the higher value of c_{ps} is lower because the high specific heat of the solid phase increases the heat energy absorption by solid phase and hence, increases the value of R and cooling rate (G.R). The higher value of R results in a larger volume of the solid and the mushy zone as shown in Figure 6(a). However, the temperatures at the top and bottom boundaries of the mushy zone are similar for both simulations S3 (maximum c_{ps}, Figure 6(a)) and S4 (minimum c_{ps}, Figure 6 (b)) and hence, the temperature gradient in the solid phase in S3 is lower than that in S4 resulting in a lower value of temperature in S3 at any given location and time as compared to S4. For example, in Figures 6(a) and 6(b) for a specific location marked by y=a and r=12 mm, the temperature in simulation S3 is lower than that in S4. The effect of c_{ps} on the results shows that it is imperative that c_{ps} be considered as function of temperature and not just a constant.

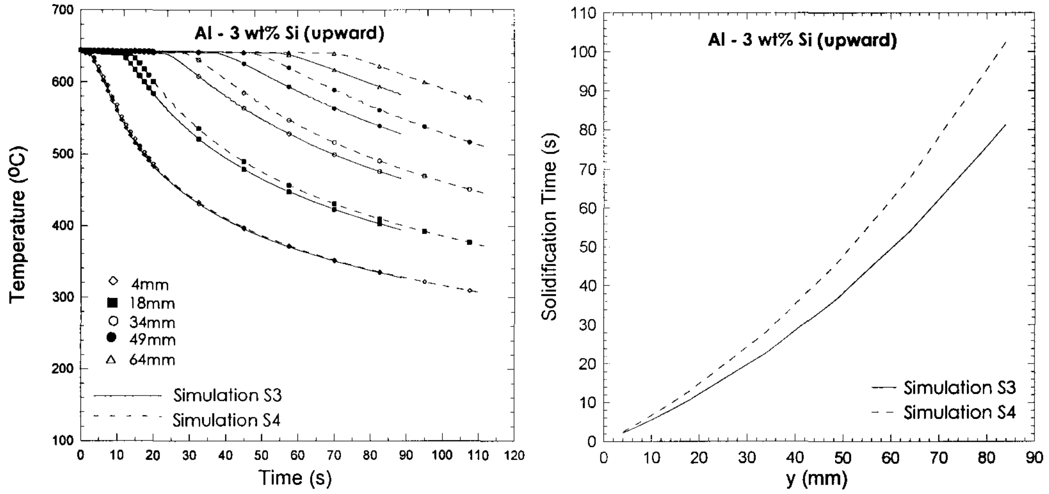

(a) (b)

Figure 5: Results for simulation S3 (maximum C_{PS}) and S4 (minimum C_{PS}. (a) transient temperature distributions at r = 0 for various locations: y = 4, 18, 34, 49, 64 mm shown in Figure 1 and (b) Solidification time determined by the location of the liquid-mushy zone interface at the centre of the cylinder (r = 0).

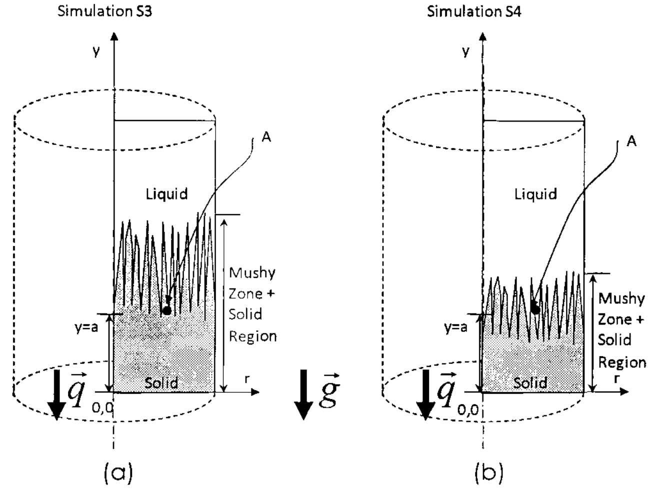

Figure 6: Snapshot of the solidifying domain showing the effect of specific heat of the solid, c_{ps} on the volumes of the solidifying phases. (a) c_{ps} = 1211 (J.kg^{-1} K^{-1}) (simulation S3) and (b) c_{ps} = 896 (J.kg^{-1} K^{-1}) (simulation S4).

Effect of ρ_s

Figure 7 shows the effect of using the maximum (simulation S5) and minimum (simulation S6) values of density of the solid phase on the solidification time. Since the maximum value of ρ_s is only 4.3 % greater than the minimum value (Table 1) there is no appreciable difference in the solidification time. Figure 7 shows only a 1% decrease in the solidification time in S5 as compared to S6.

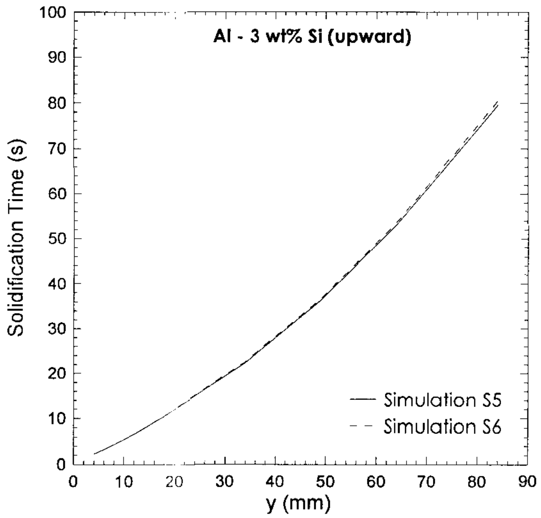

Figure 7: Effect of maximum (S5) and minimum (S6) values of density of the solid phase on the solidification time at r = 0.

The variation of density of the liquid phase is about 0.9 % as shown in Table 1 and 4.3% in the solid phase. Since the variation in the solid phase shows an insignificant change of 1% in the solidification time (Figure 7), the value of density of the solid and the liquid phases can be assumed constant in binary Al-Si alloy solidification simulations. The same line of reasoning can be extended to assuming the values of K_l and C_{pl} as constants for the liquid phase because the maximum variation in their values is 2.6% and 0.05 %, respectively and hence, no significant variation in solidification time would be observed by changing these values as function of temperature during solidification simulations of Al-Si binary alloys.

Effect of D

Figure 8(a) shows solidification time for simulations S7 and S8 and Figure 8(b) shows that for simulations S9 and S10. When the effect of undercooling [4], was considered in simulations S7 and S8 along with two order of magnitude difference between the values of D in S7 and S8, respectively, only a 10% variation in the solidification time was observed (Figure 8(a)). Hence, it can be safe to assume a constant value of the solute mass diffusivity, D in the liquid phase for binary Al-Si alloy solidifications. When the effect of ΔT [4] was not considered in simulations S9 and S10, the two orders of magnitude difference between the maximum (S9) and minimum (S10) value of D did not show any appreciable variation in the solidification time, as shown in Figure 8(b).

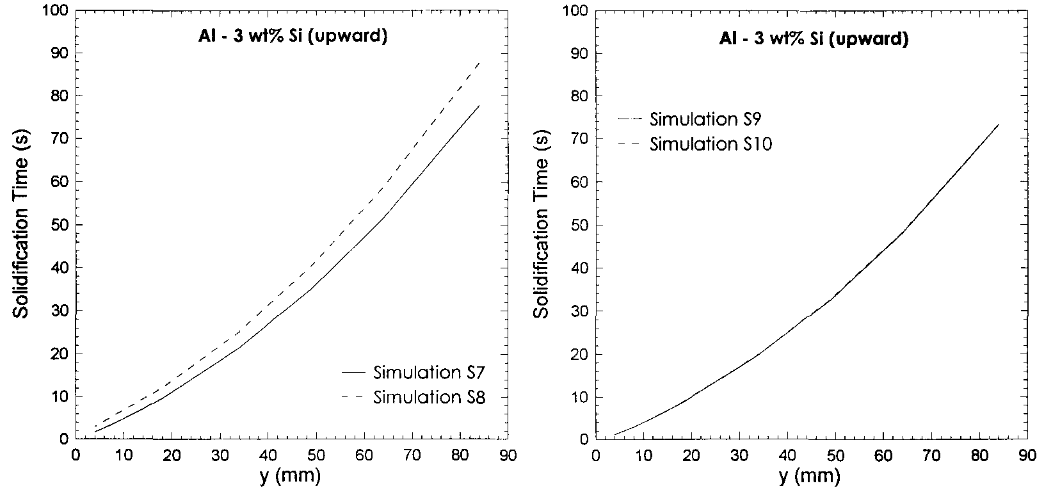

(a) (b)

Figure 8: Solidification time for the liquid/mushy zone interface at the centre of cylinder for 100 times variation in solute diffusivity of liquid (Table 1) (S7 and S9 are for greater D; S8 and S10 are for smaller D). (a) Results with consideration of ΔT (b) Results without ΔT.

Figure 9(a) and Figure 9(b) show a schematic of a binary alloy phase diagram and two adjacent control volumes, CV_1 and CV_2, respectively, where CV_1 is closer to the heat extraction boundary.

Due to the effect of ΔT (simulations S7 and S8) the temperature in CV_1 will have to reach a value of (T_{liq}-ΔT) before the onset of the solidification event of the primary phase. The temperature of CV_2 will be slightly greater than that CV_1. When the solidification event occurs in CV_1, the concentration of the liquid ahead of the liquid-mushy zone interface, C_{L1} will be greater than the average concentration of the alloy, C_o and the concentration of the liquid in CV_2 will also be greater than C_o, but, C_{L2} will be less than C_{L1}. With a higher value of the diffusion coefficient, D (S7), the value of C_{L2} will reach the equilibrium value of C_L* faster than that with a lower value of D (S8) and hence in Figure 8(a), solidification time for simulation S7 is lower than that in S8.

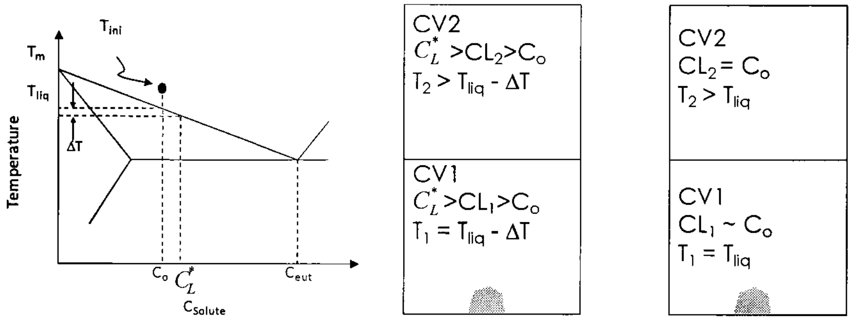

(a) (b) (c)

Figure 9: Schematic of (a) phase diagram of Al-Si alloy; (b) diffusion of solute in CVs during solidification with consideration of undercooling and (c) without undercooling.

Figure 9(c) shows the two control volumes CV1 and CV2 in simulations S9 and S10 without the effect of ΔT [4]. The solidification event will occur in CV_1 when the temperature of the liquid reaches the liquidus temperature, T_{liq} and the liquid concentration (C_{L1}) of CV_1 will be almost equal to the average concentration of the alloy, C_o. The liquid concentration (C_{L2}) of CV_2 will be equal to C_o. Hence, there will no appreciable diffusion of the solute phase from CV_1 to CV_2. As a result, a variation in the value of D between simulations S9 and S10 did not have any effect on the solidification time.

Hence, for a valid solidification simulation of binary Al-Si alloys, the effect of undercooling of the liquidus temperature prior to the solidification event must be considered and the value of the diffusion coefficient of the solute in the liquid phase can be assumed constant.

SUMMARY AND CONCLUSIONS

During the solidification simulation of binary Al-Si alloys, the thermo-physical properties of the liquid and solid phases could be safely assumed as constant when the variation between the maximum and minimum values of each such property is less than 5%. If the variation is greater than 5%, it is best to consider the properties as function of temperature. For the solidification simulation of the Al-3wt%Si alloy, all material properties of the liquid phase and the density of the solid phase could be assumed constant, however, the thermal conductivity and specific heat of the solid phase must be considered as function of temperature for a valid simulation. It is also recommended that the effect of undercooling of liquidus temperature prior to the solidification event of the primary phase should be considered during solidification simulation of binary alloys. Diffusivity of solute in liquid has a marginal effect on solidification time when undercooling was considered.

REFERENCES

[1] JMatPro, 4.1 ed Guildford ,UK.: Sente Software Ltd.

[2] D. P. Sekulic, P. K. Galenko, M. D. Krivilyov, L. Walker, and F. Gao, "Dendritic growth in Al-Si alloys during brazing. Part 2: Computational modeling," *International Journal of Heat and Mass Transfer,* vol. 48, pp. 2385-2396, 2005.

[3] Factsage, 5.5 ed Madison, WI, USA.: Computherm LLC.

[4] H. Wang, "Solidification Simulation of Binary Al-Si Alloys: Prediction of Primary Dendrite Arm Spacing with Macro-scale Simulations (~1mm Length Scale)," in *Department of Mechanical Engineering, McMaster University,* Hamilton, Ontario, Canada, Publication A, Ph. D. Thesis, 2009.

[5] M. D. Peres, C. A. Siqueira, and A. Garcia, "Macrostructural and microstructural development in Al-Si alloys directionally solidified under unsteady-state conditions," *Journal of Alloys and Compounds,* vol. 381, pp. 168-181, November 3 2004.

[6] H. Wang, "Solidification Simulation of Binary Al-Si Alloys: Prediction of Primary Dendrite Arm Spacing with Macro-Scale Simulations (~1mm Length Scale)," in *Department of Mechanical Engineering, McMaster University,* Hamilton, Ontario, Canada, Publication D, Ph. D. Thesis, 2009.

[7] V. R. Voller and C. Prakash, "Fixed grid numerical modeling methodology for convection - diffusion mushy region phase – change problems," *International Journal of Heat and Mass Transfer,* vol. 30, pp. 1709-1719, 1987.

[8] W. D. Bennon and F. P. Incropera, "A continuum model for momentum, heat and species transport in binary solid – liquid phase change systems - I. Model formulation," *International Journal of Heat and Mass Transfer,* vol. 30, pp. 2161-2170, 1987.

[9] W. D. Bennon and F. P. Incropera, "A continuum model for momentum, heat and species transport in binary solid – liquid phase change systems - II. Application to solidification in a rectangular cavity," *International Journal of Heat and Mass Transfer,* vol. 30, pp. 2171-2178, October 1987.

[10] W. D. Bennon and F. P. Incropera, "Numerical analysis of binary solid – liquid phase change using a continuum model," *Numerical Heat Transfer,* vol. 13, pp. 277-296, 1988.

[11] S. D. Felicelli, J. C. Heinrich, and D. R. Poirier, "Simulation of freckles during vertical solidification of binary alloys," *Metallurgical Transactions B (Process Metallurgy),* vol. 22, pp. 847-859, Dec. 1991.

[12] S. D. Felicelli, J. C. Heinrich, and D. R. Poirier, "Numerical models for dendritic solidification of binary alloys," *Numerical Heat Transfer, Part B: Fundamentals,* vol. 23, pp. 461-481, 1993.

[13] E. McBride, J. C. Heinrich, and D. R. Poirier, "Numerical simulation of incompressible flow driven by density variations during phase change," *International Journal for Numerical Methods in Fluids,* vol. 31, pp. 787-800, Nov. 1999.

[14] J. C. Heinrich and D. R. Poirier, "The effect of volume change during directional solidification of binary alloys," *Modeling and Simulation in Materials Science and Engineering,* vol. 12, pp. 881-899, Sep. 2004.

[15] M. C. Flemings, *Solidification processing.* New York, NY.: McGraw-hill Book Co., 1974.

[16] M. H. Burden and J. D. Hunt, "Cellular and dendritic growth. I," *Journal of Crystal Growth*, vol. 22, pp. 99-108, 1974.

[17] M. H. Burden and J. D. Hunt, "Cellular and dendritic growth. II," *Journal of Crystal Growth*, vol. 22, pp. 109-116, 1974.

EFFECT OF SHRINKAGE ON PRIMARY DENDRITE ARM SPACING DURING BINARY Al-Si ALLOY SOLIDIFICATION

Hongda Wang[1,2], Sumanth Shankar[1], Mohamed S. Hamed[2,*]
[1]Light Metal Casting Research Centre (LMCRC)
[2]Thermal Processing Laboratory (TPL)
McMaster University, Hamilton, ON, Canada L8S 4L7

ABSTRACT

Upward and downward directional solidification of hypoeutectic Al-Si alloys were numerically simulated inside a cylindrical container. Energy, concentration, momentum and continuity equations were solved by using the finite-volume method. Temperature and liquid concentrations inside the mushy zone were coupled by local equilibrium assumptions. Energy equation was applied to determine liquid fraction inside the mushy zone while considering the temperature undercooling at the solidifying dendrite/liquid interface. Momentum and continuity equations were coupled by the SIMPLE algorithm. Flow velocity distribution at various times, G, R, λ_1 and solidification time at mushy zone/liquid interface during solidification were predicted. The effect of shrinkage during solidification on these solidification parameters has been quantified. Transient temperature distribution, solidification time for the mushy zone/liquid interface and λ_1 were validated by laboratory experiments. It was found that better agreement could be achieved when the fluid flow due to solidification shrinkage was considered. Considering shrinkage in upward solidification was found to have an insignificant effect on solidification parameters, such as G, R and λ_1; whereas, in the downward solidification, fluid flow due to shrinkage had a significant effect on these solidification parameters. Considering shrinkage during downward solidification resulted in a smaller R, stronger fluid flow and increased solidification time at mushy zone/liquid interface. Further, flow pattern was significantly altered when solidification shrinkage was considered in the simulation. The effect of shrinkage on G and λ_1 was more complicated and strongly depended on the instantaneous location of the mushy zone/liquid interface in the computational domain.

NOMENCLATURE

c_{ps}	Specific heat of solid as a function of temperature (J Kg^{-1} K^{-1}) [1];
c_{pl}	Specific heat of liquid (J Kg^{-1} K^{-1}) [1];
C_L	Liquid concentration (wt%);
C_o	Average alloy composition (wt%);
C_S	Solid concentration (wt%);

---

[*] Corresponding Author: hamedm@mcmaster.ca , voice: (905) 525-9140 X 26113

D	Solute diffusivity coefficient of liquid (6.25×10^{-9} ($m^2 s^{-1}$)) [2];
G	Temperature gradient in liquid at the mushy zone/liquid interface (^oC mm^{-1});
k	Average partition coefficient (0.116) [3];
K_s	Thermal conductivity of solid as a function of temperature (W m^{-1} K^{-1}) [1];
K_l	Thermal conductivity of liquid (W m^{-1} K^{-1}) [1];
L	Latent heat of fusion (J Kg^{-1}) [3];
m	The slope of liquidus line (– 6.675 (K $wt\%^{-1}$)) [3];
p	Pressure(Pa);
R	Velocity of mushy zone/liquid interface (mm s^{-1});
t	Time (s);
T	Temperature (^oC);
T_{liq}	Liquidus temperature (^oC) [3];
T_{ini}	Initial temperature of liquid (^oC);
T_m	Melting temperature of pure aluminum (660 ^oC) [3];
T_{eut}	Eutectic temperature (578.6 ^oC) [3];
$\dot{T}$	Instantaneous tip cooling rate = G×R (^oC s^{-1});
ΔT	Undercooling of T_{liq} (^oC);
U_r	Velocity in r direction ($mm.s^{-1}$);
U_y	Velocity in y direction ($mm.s^{-1}$);
U	Flow velocity in the liquid of mushy zone/liquid interface ($mm.s^{-1}$);
β	Contraction ratio $\left[\beta = \frac{\rho_s - \rho_l}{\rho_l}\right]$ (volumetric shrinkage during solidification) [1];
β_C	Solute expansion coefficient (-4.26×10^{-4} (K^{-1})) [1];
β_T	Thermal expansion coefficient (1.39×10^{-4} (K^{-1})) [1];
Γ	Gibbs-Thomson coefficient (1.97×10^{-7} (K m^{-1})) [4];
ϕ	Liquid fraction;
ρ_l	Liquid density (Kg m^{-3}) [1];
ρ_s	Solid density (Kg m^{-3}) [1];
μ	Dynamic viscosity 1.3×10^{-3} (Pa s) [1];
λ_1^0	Primary arm spacing if no fluid flow effect is considered (μm);
λ_1	Primary arm spacing (μm);

THERMO-PHYSICAL MATERIAL PROPERTIES

Properties	Al-3wt%Si	Al-5wt%Si	Al-7wt%Si
K_s	228.08 – 0.061055×T	226.01-0.077488×T	223.93-0.093920×T
K_l	85.476	84.568	83.661
C_{ps}	887.23+0.50227×T	883.54+0.50227×T	879.85+0.50227×T
C_{pl}	1168.9	1163.7	1158.6
ρ_s	2627.9	2621.6	2614.5
ρ_l	2415.0	2422.8	2430.6
L	4.05×10^5	4.25×10^5	4.45×10^5

INTRODUCTION

Shrinkage and natural convection are two main mechanisms that could induce fluid flow during solidification. In upward solidification, the positive density gradient is in the direction of the gravity vector and hence, no fluid flow is induced by natural convection, whereas, the positive density gradient is against the direction of the gravity vector in downward solidification and there will be significant fluid flow induced by natural convection. However, in both modes of solidification, shrinkage induces fluid flow.

Various algorithms have been proposed to simulate solidification of binary alloys based on the volume averaging theory [5-8]. Numerical models used in these algorithms focused primarily on the development of fluid flow during solidification in the whole computational domain. The density of solid was assumed equal to that of the liquid phase. Therefore, the effect of shrinkage was absent. Some of these algorithms were further developed [9-12] with consideration of density variation between liquid and solid phases. However, these studies [9-12] combined the fluid flow caused by shrinkage and natural convection and did not differentiate between them. A few investigations have focused on only the effect of shrinkage on the fluid flow, however, there have been no correlation between the fluid flow caused by shrinkage and the primary dendrite arm spacing. To enable such as correlation, this study has carried out solidification simulations in the macro-scale control volume(CV) (~ 1mm) with optimized thermo-physical material properties, accounting for the effect of undercooling of liquidus temperature prior to the solidification event, ΔT, employing appropriate models to predict λ_1, and considering the effect of fluid flow due to shrinkage.

Xu et al [13] were amongst the earliest researchers who considered different density values for the solid and liquid phases (shrinkage) and evaluated fluid flow patterns in the computing domain during solidification. They found that there is a significant increase in the pressure drop inside the mushy zone (region where solid and liquid phases co-exist) when compared to that in the liquid phase. Hence, it was conjectured that inside the mushy zone, fluid flow induced by shrinkage was dominant over that induced by natural convection.

Chiang et al [14] investigated the effect of shrinkage on the solidification of 1% Cr - steel alloy in a rectangular cavity with a riser on the top away from the heat extraction boundary. All sides of the cavity were insulated, except the chilled bottom. Numerical results with shrinkage were compared with pure diffusion case (without any fluid flow). It was reported that considering solidification shrinkage resulted in higher temperatures close to the heat extraction boundary and lower temperatures closer to the top of the riser. Chiang et al [15] also investigated the combined effect of natural convection and shrinkage on fluid flow during solidification of 1 % Cr – steel alloy. It was reported that the effect of shrinkage on the temperature field was very small. However, no quantitative temperature field was reported. The direction of circular fluid flow was reversed when the effect of shrinkage was coupled with that of natural convection when compared to the flow induced by natural convection alone. Shrinkage dominated fluid flow at the beginning of solidification until the effect of natural convection was pronounced on the fluid flow. At the final stages of solidification, shrinkage dominated fluid flow again. Maximum velocities occurred in the period wherein the flow was dominated by natural convection. The fluid flow inside the mushy zone was wholly dominated by shrinkage at all times.

Krane et al [16] investigated effect of shrinkage on the redistribution of solute for Pb–19.2wt%Sn and Pb-6.5wt%Sn alloys during solidification inside a horizontal cavity. Three cooling rates were considered by varying the heat transfer coefficient at the heat extraction boundary between 10^2 and 10^4 $W.m^{-2}.K^{-1}$. It was concluded that there was no significant effect on the macro-segregation of the solute atoms due to varied effect of shrinkage on flow velocities.

Although most of the numerical simulations carried out after 1993 [2, 11, 12, 16-20] considered both natural convection and shrinkage induced fluid flow during solidification, most arguments presented the fluid flow and macro-segregation of the solute and no in-depth analysis of the individual effect of shrinkage and natural convection on the critical solidification parameters such as temperature gradient of liquid at the mushy zone/liquid interface, G, velocity of the interface, R, transient temperature distribution during solidification, solidification time (location of mushy zone/liquid interface) and primary dendrite arm spacing were carried out. The aim of this study is to carry out this in-depth analysis considering Al-3wt%Si (upward solidification) and Al-5wt% Si (downward solidification) alloys. The solidification simulations in this study were validated by experiment results reported in [21, 22].

THE COMPUTATIONAL DOMAIN

Figure 1 and Figure 2 show schematics of the computational domain with the boundary conditions for T and C_L, u_r and u_y, respectively. Figure 1(a) and Figure 2(a) are schematics for the case of upward solidification and Figure 1(b) and Figure 2(b) are schematics for the case of downward solidification modes.

Al–3wt%Si and Al-5wt%Si alloy melts with a marginal superheat temperature was considered inside a cylindrical geometry for upward and downward solidification, respectively. All dimensions and boundary conditions used here are similar to those reported in the experimental study [21, 22]. The geometry considered in this study is a cylinder with a diameter of 55 mm and height of 145 mm. As shown in Figure 1, the computing domain is a two-dimensional cross-section of the geometry and owing to symmetry only one half of the cylinder was used as the computing domain. Figure 1 also shows the direction of heat extraction, $\vec{q}$ and the gravity vector, $\vec{g}$.

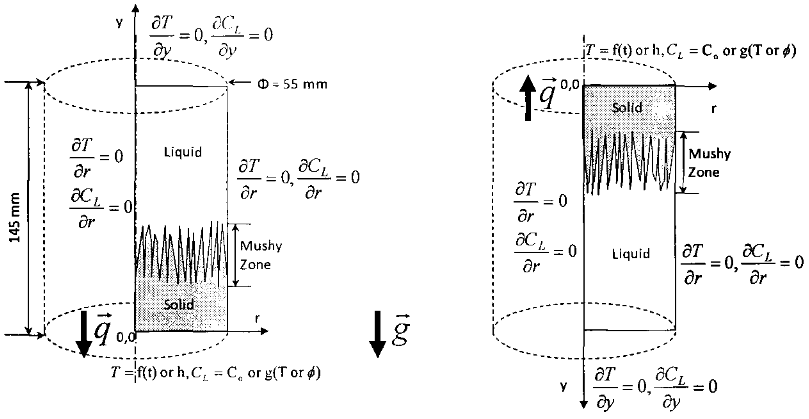

(a) (b)

Figure 1: Model problem and boundary conditions (thermal and liquid concentration) for (a) upward solidification and (b) downward solidification.

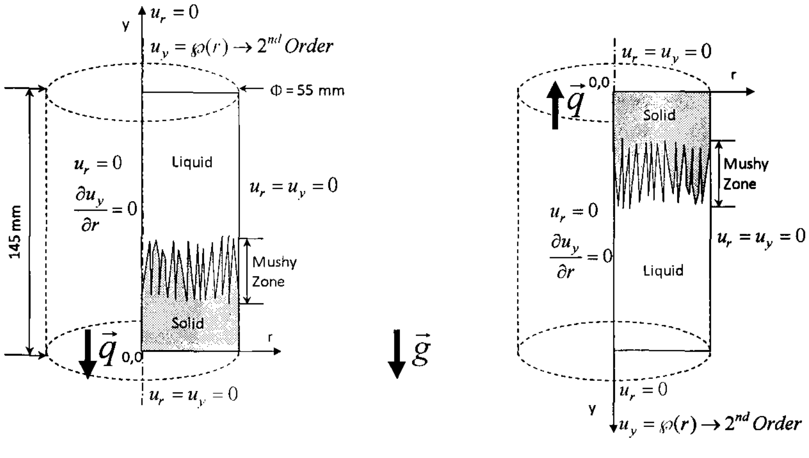

(a) (b)

Figure 2: Velocities at the boundaries of the computing domains presented in Figure 1. (a) upward solidification and (b) downward solidification.

THE Governing Equations

The governing equations of the solidification process of the model problem shown in Figure 1 are presented in this section. The energy equation is presented in Equation (1) and the concentration equation in Equation (2).

$$\overbrace{\frac{\partial((\phi\rho_l c_{pl}+(1-\phi)\rho_s c_{ps})T)}{\partial t}}^{\text{Transient Term}}+\overbrace{\rho_l c_{pl} u_r \frac{\partial T}{\partial r}+\rho_l c_{pl} u_y \frac{\partial T}{\partial y}}^{\text{Convection Term}}+\overbrace{\rho_s L\frac{\partial \phi}{\partial t}}^{\text{Phase Transformation Term}}$$

$$=\underbrace{\frac{1}{r}\frac{\partial}{\partial r}(r(\phi K_l+(1-\phi)K_s)\frac{\partial T}{\partial r})+\frac{\partial}{\partial y}((\phi K_l+(1-\phi)K_s)\frac{\partial T}{\partial y})}_{\text{Diffusion Term}} \tag{1}$$

$$\overbrace{\frac{\partial(\phi\rho_l C_L+(1-\phi)\rho_s C_S)}{\partial t}}^{\text{Transient Term}}+\overbrace{\rho_l u_r\frac{\partial C_L}{\partial r}+\rho_l u_y\frac{\partial C_L}{\partial y}}^{\text{Convection Terms}}$$

$$=-\rho_l[\underbrace{\beta C_L\frac{\partial\phi}{\partial t}}_{\substack{\text{Source Term}\\ \text{from Shrinkage}}}-\underbrace{D(\frac{1}{r}\frac{\partial}{\partial r}(\phi r\frac{\partial C_L}{\partial r}))-D\frac{\partial}{\partial y}(\phi\frac{\partial C_L}{\partial y})}_{\text{Diffusion Term}}] \tag{2}$$

Temperature of a CV in the mushy zone was determined by Equation (3) wherein local equilibrium conditions were assumed [23].

$$T=T_m+mC_L \tag{3}$$

If the phenomenon of re-melting of solid did not occur, the average solute concentration of the solid phase in a CV was evaluated by Equation (4).

$$C_S=\frac{1}{1-\phi}\int_\phi^1 kC_L d\phi \tag{4}$$

Re-melting is the phenomenon that the already solidified solid phase is melted inside CV during solidification procedure. This may occur because the convective current with higher temperature is flowed into this CV. If re-melting of solid occurs, Cs must be taken from the history of Cs during solidification [6]. During solidification procedure as solid phase inside CV keeps on growing (no re-melting), the magnitude of Cs has to be recorded with the decreasing of ϕ from the first piece of solid at the beginning of solidification according to equation (4). As re-melting occurs, Cs need to be obtained from the recorded history according to the different ϕ instead of directly applying equation (4).

Mass conservation is presented in Equation (5).

$$\frac{1}{r}\frac{\partial(ru_r)}{\partial r}+\frac{\partial u_y}{\partial y}=\beta\frac{\partial\phi}{\partial t} \tag{5}$$

The momentum equations in the r and y directions as defined in Figure 1 are presented in Equations (6) and (7), respectively.

$$\rho_l \frac{\partial u_r}{\partial t} + \rho_l \frac{u_r}{\phi} \frac{\partial u_r}{\partial r} + \rho_l \frac{u_y}{\phi} \frac{\partial u_r}{\partial y} + \rho_l \frac{\beta}{\phi} \frac{\partial \phi}{\partial t} u_r$$

$$= -\phi \frac{\partial p}{\partial r} + \frac{1}{r} \frac{\partial (r 2\mu \frac{\partial u_r}{\partial r})}{\partial r} - \frac{2\mu u_r}{r^2} + \frac{\partial (\mu \frac{\partial u_y}{\partial r} + \mu \partial \frac{\partial u_r}{\partial y})}{\partial y} + \mu \frac{\beta}{3} \frac{\partial (\frac{\partial \phi}{\partial t})}{\partial r} - \frac{\mu \phi u_r}{k_n} \tag{6}$$

$$\rho_l \frac{\partial u_y}{\partial t} + \rho_l \frac{u_r}{\phi} \frac{\partial u_y}{\partial r} + \rho_l \frac{u_y}{\phi} \frac{\partial u_y}{\partial y} + \rho_l \frac{\beta}{\phi} \frac{\partial \phi}{\partial t} u_y$$

$$= -\phi \frac{\partial p}{\partial y} + \frac{1}{r} \frac{\partial [r(\mu \frac{\partial u_y}{\partial r} + \mu \partial \frac{\partial u_r}{\partial y})]}{\partial r} + \frac{\partial (2\mu \frac{\partial u_y}{\partial y})}{\partial y} + \mu \frac{\beta}{3} \frac{\partial (\frac{\partial \phi}{\partial t})}{\partial y} - \frac{\mu \phi u_y}{k_p} + \rho_l^* \phi g_y \tag{7}$$

Where ρ_l^* is applied with Boussinesq assumption: $\rho_l^* = \rho_l \left(\beta_T (T - T_{ini}) - \beta_c (C_L - C_o) \right)$

The undercooling is estimated by the model proposed by Burden et al [24, 25] and is given in Equation (8).

$$\Delta T = (\frac{GD}{R}) + \frac{\left(-8mR(1-k)C_o \Gamma \right)^{\frac{1}{2}}}{D^{\frac{1}{2}}} \tag{8}$$

The magnitude of undercooling in the present work is not a constant throughout the solidification process but is updated at every time step for each CV in the domain.

A simplified version of the Kozeny – Carman model [26, 27] is used to define the permeability of the mushy zone as a function of the liquid fraction, which is the one proposed by Asai et al [28] and presented here in Equation (9). The morphology of the dendrites in Equation (9) is assumed to be conical with a large height to base diameter ratio and the magnitude of permeability in the direction normal to dendrite growth, K_n is assumed identical to the parallel direction, K_p.

$$K_p = K_n = \frac{1}{5\left(\frac{6}{\lambda_1} \right)^2} \frac{\phi^3}{(1-\phi)^2} \tag{9}$$

Bouchard et al [29] proposed an expression, presented in Equation (10), for the primary dendrite arm spacing from both theoretical and empirical assessments of unsteady solidification conditions. Lehmann et al [30] proposed a theoretical expression, presented in Equation (11), to evaluate primary dendrite arm spacing as function of the fluid flow velocity in the mushy zone.

$$\lambda_1^0 = a_1 \left(\frac{16 C_o^{\frac{1}{2}} G_o \varepsilon \Gamma D}{(1-k) m G R} \right)^{\frac{1}{2}} \tag{10}$$

$$\lambda_1 = \lambda_1^0 \left(1 + \frac{U}{R} \right)^{-\frac{1}{2}} \tag{11}$$

In Equation (10), $G_o\varepsilon$ is a characteristic parameter (≈ 360 K.mm^{-1}) [29] and the coefficient a_1 = 250 for Al-Si hypoeutectic alloys, [22].

The governing equations (1) to (9) are solved in the macro simulations. Results of the macro simulations include transient temperature distribution can then be applied to calculate the solidification time, G and R. The values of G, R and U (fluid flow velocity at the top of the mushy zone) are then used as input parameters for the estimation of λ_1 using equations (10) and (11). This is the procedure used here to investigate the effect of the fluid flow determined at the macro level on G, R and λ_1.

Initial Conditions

Table 1 shows the initial conditions for the composition, temperature, velocity, liquid fraction and primary arm spacing in the computational domain shown in Figure 1 and Figure 2.

Table 1: Initial conditions for the solidification simulations.

C_o	T_{ini} (°C)	U_r(m.s^{-1})	u_y(m.s^{-1})	ϕ	λ_1(μm)
Al-3wt%Si (Upward)	644.0	0	0	1	300
Al-7wt%Si (Downward)	620.3	0	0	1	300
Al-5wt%Si (Downward)	633.7	0	0	1	300

Boundary Conditions

Boundary conditions for T, C_L, u_r, u_y are shown in Figure 1 and Figure 2, respectively.

The function f(t), shown in Figure 1(a), at y = 0 for Al-3wt%Si upward solidification was determined by the correlation equation from experimental work, Peres et al [21], as shown in equation (12):

$$f(t) = \begin{cases} -12 \times t + 644 \ (t \le 10s) \\ 637.44 - 63.08 \times \ln(t) + 198.96/\ln(t) - 8.30 \times \ln(t)^2 - 115.26/\ln(t)^2 + 0.89 \times \ln(t)^3 \ (t > 10s) \end{cases} \tag{12}$$

Thermal boundary condition for Al-5wt%Si downward solidification at y = 0 is: h = 2400 (W m^{-2} K^{-1}) [22]. For Al-7wt%Si downward solidification, thermal boundary condition at y = 0 is defined as transient temperature distribution f(t) by correlation equation (13) from experimental work Spinelli et al [22], as shown in Figure 1(b):

$$\begin{aligned} f(t) = {} & 620.35 - 9.89\times t + 9.32\times 10^{-2}\times t^{2} + 4.00\times 10^{-3}\times t^{3} - 1.60\times 10^{-4}\times t^{4} + 2.68\times 10^{-6}\times t^{5} - 2.50\times 10^{-8}\times t^{6} \\ & + 1.43\times 10^{-10}\times t^{7} - 4.90\times 10^{-13}\times t^{8} + 9.10\times 10^{-16}\times t^{9} - 7.20\times 10^{-19}\times t^{10} \end{aligned} \tag{13}$$

Boundary conditions for C_L at y = 0 in either upward or downward solidification is defined by equation (14):

$$C_L = \begin{cases} C_o & T > T_{liq} - \Delta T \\ g(\phi) & T = T_{liq} - \Delta T \quad g(\phi) \text{ defined by Equation (2)} \\ g(T) & T < T_{liq} - \Delta T \quad g(T) \text{ defined by Equation (3)} \end{cases} \tag{14}$$

The velocities at the boundaries of the computing domain presented in Figure 1 are shown in Figure 2. In Figure 2, the velocity, $u_y(r)$ at y = 145mm is adopted a second order (parabolic) function of r, as discussed in Wang [31]. $u_y(r)$ is defined by equation (15):

$$u_y(r) = u_{max}\left\{1 - \left(\frac{r}{R}\right)^2\right\} \tag{15}$$

where u_{max} is the maximum velocity at r = 0 and evaluated by the shrinkage observed during solidification. Volume flow rate (VFR) due to shrinkage at y = 145mm is calculated at each time step during simulation and is given in equation (16):

$$VFR = \int_0^H \int_0^{Ri} 2\pi \cdot r\left(\frac{1}{r}\frac{\partial(ru_r)}{\partial r} + \frac{\partial u_y}{\partial y}\right)\cdot dr \cdot dy \tag{16}$$

Ri and H are the radius and height of computing domain, respectively. With values of VFR after each time step, u_{max} could be evaluated and subsequently, the boundary condition could

NUMERICAL PROCEDURE

Table 2 presents the identification and details of the simulations carried out in this study. Figure 3 shows the flow chart outlining the numerical algorithm used in the present solidification simulations. A detailed explanation of this procedure is presented in Wang et al [32].

Table 2: Identification and details of the simulations carried out.

Simulation Identification	Solidification Mode	C_o	Shrinkage
S1	Downward	Al-7wt%Si	Yes
S2	Upward	Al-3wt%Si	Yes
S3	Upward	Al-3wt%Si	No
S4	Downward	Al-5wt%Si	Yes
S5	Downward	Al-5wt%Si	No

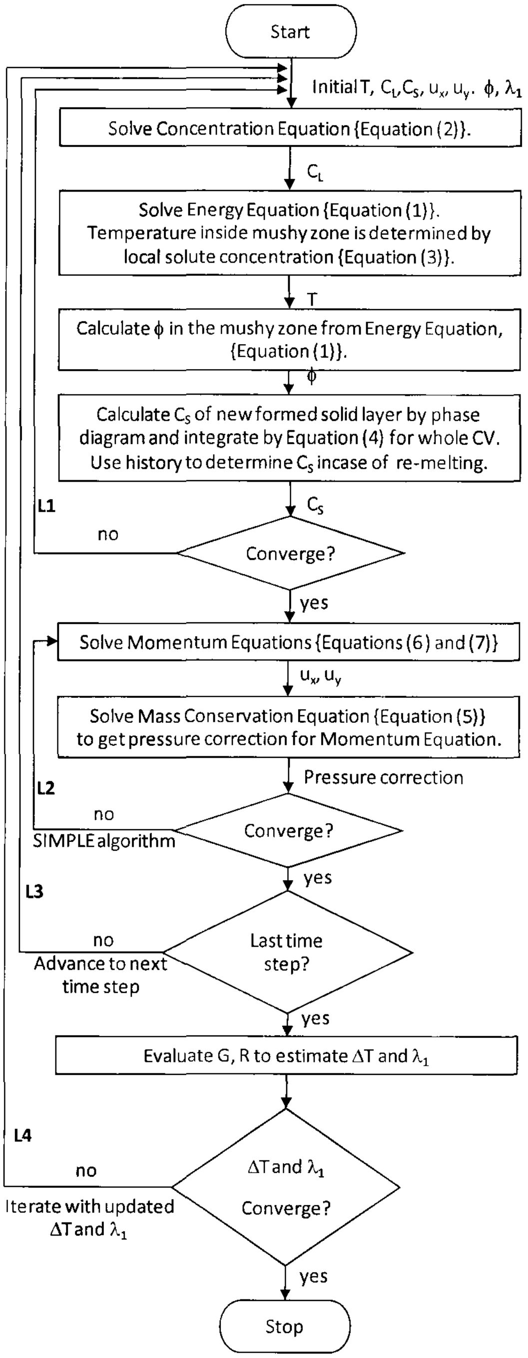

Figure 3: Flow chart of the present numerical algorithm.

RESULTS AND DISCUSSION

The results and discussion will be presented in the following sections:

- Validation of transient temperature distribution by experiments
- Effect of shrinkage on fluid flow
- Effect of shrinkage on solidification time
- Effect of shrinkage on G
- Effect of shrinkage on R
- Effect of shrinkage on λ_1

Validation of Transient Temperature Distribution by Experiments

The experiment results by Peres et al [21] obtained during upward solidification of Al-3wt%Si alloy were used for validation of the transient temperature distribution predicted by the present algorithm in simulation S2. The experiment results by Spinelli et al [22] was used to validate results of the downward solidification simulation S1 for Al-7wt%Si alloy. Figure 4(a) shows transient temperature distributions at r=0 for various locations of y = 4, 18, 34, 49 and 64 mm form the heat extraction boundary for the upward solidification of Al-3wt%Si alloy; and Figure 4(b) shows that for the downward solidification at r = 0 and various locations of y = 8, 22, 36 and 57 mm from the heat extraction boundary. Results presented in Figure 4 show good agreement in both cases.

Further validation of the numerical results has been carried out by comparing solidification time predicted by the upward and downward solidification simulations, which is presented in the subsequent section discussing the effect of shrinkage on solidification time.

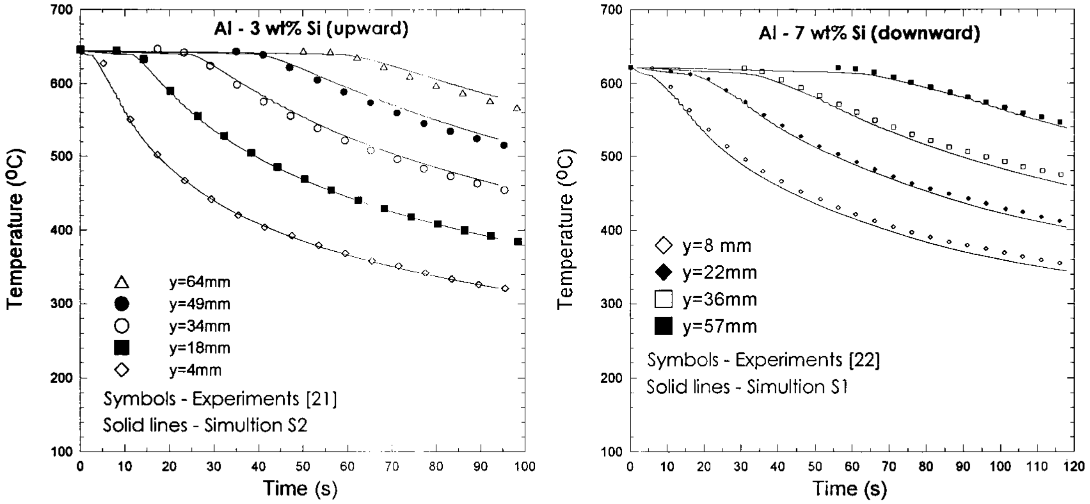

(a) (b)

Figure 4: Validation of transient temperature distributions for simulations S2 and S1 at r = 0 with experiment data by (a) Peres et al [21] for upward solidification (simulation S2) and (b) Spinelli et al [22] for downward solidification (simulation S1).

Effect of Shrinkage on Fluid Flow

Since there is no fluid flow in the case of upward solidification without shrinkage (simulation S3), there is no reason to carry out any comparison for the fluid flow between simulations S3 and S2 (Al-3wt%Si upward solidification with effect of shrinkage).

Figure 5 shows the development of the flow field in simulations S5 (Al-5wt%Si without effect of shrinkage) and S4 (Al-5wt%Si with effect of shrinkage). In Figure 5, the time and maximum velocity are presented at the top and bottom of each snap shot, respectively. Locations of the three solidification zones: *solid, mushy zone and liquid* are also shown. The black lines shown in the mushy zone represent constant liquid fraction lines.

In Figure 5(a), during the initial stages of solidification at time t= 5s, fluid flow is dominated by shrinkage, which is indicated by the vertical upward direction of the flow. At t = 25s, fluid flow is now driven by natural convection due to the positive density gradient against the direction of gravity, which is evident by the development of circular flow regime in the domain. This circular flow caused by natural convection dominates over flow caused by shrinkage and continues to strengthen until about t= 75s. Towards the end of solidification, the space of the liquid phase is small enough to reduce the strength of the flow caused by natural convection.

Figure 5(b) shows numerical results for the case with no shrinkage. In the initial period of solidification at t = 5s, there is no visible fluid flow developed in the domain. After time t = 5s the positive density gradient against the direction of gravity induces a circular fluid flow due to natural convection. AT t = 25s, there are two circular regimes developed in the domain and the one closer to the mushy zone is stronger because of the greater density gradient located here. Flow rotating direction is anticlockwise without the effect of shrinkage. This is because the fluid at the center of the cylinder tends to flow down due to the longer distance away from the side wall of cylinder with non-slip boundary conditions. Subsequently, at t = 75s, the stronger circular flow regime dominates over the weaker one and occupies the whole domain.

The main difference between simulations S4 and S5 is shown in Table 3.

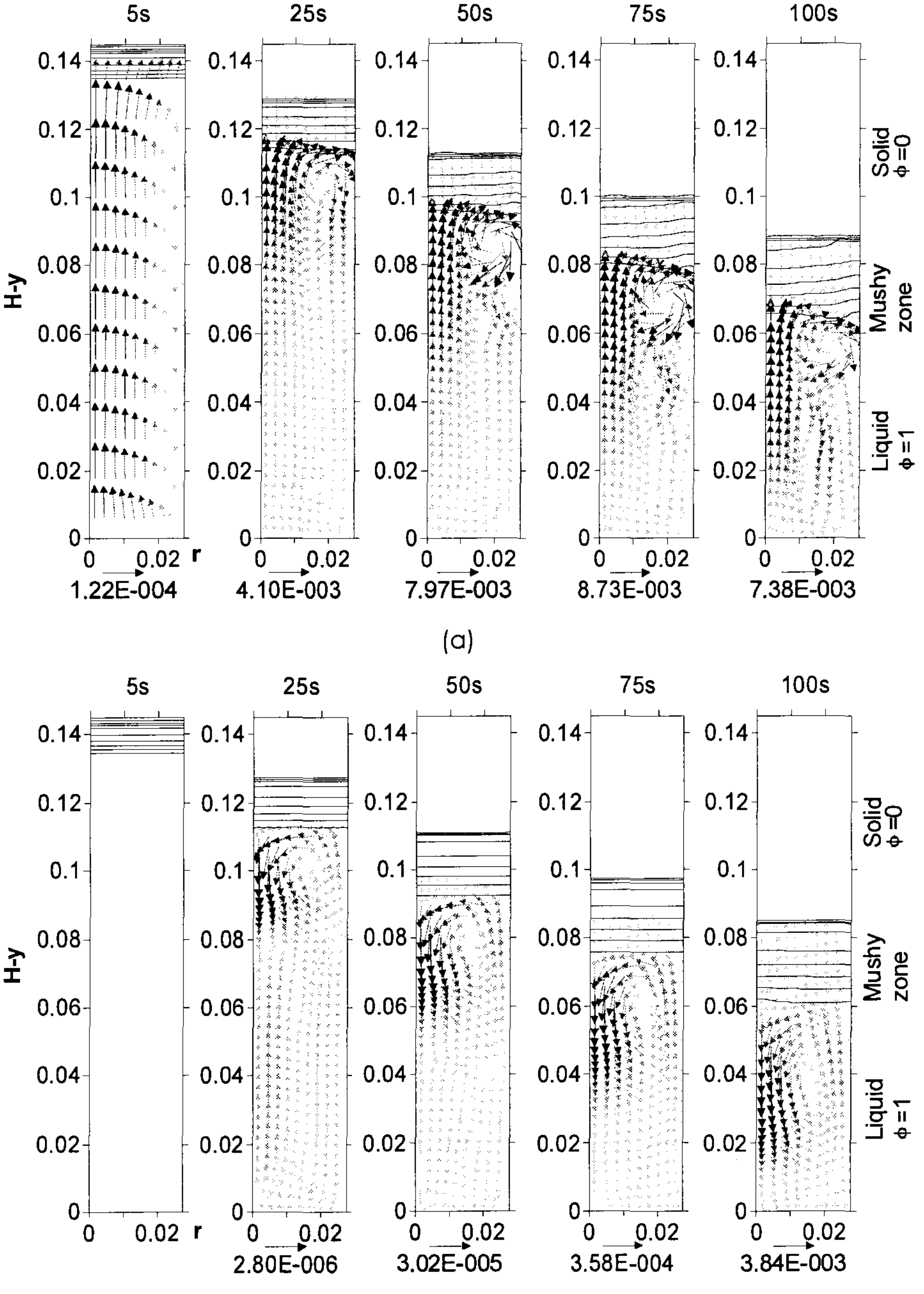

(a)

(b)

Figure 5: Development of fluid flow during simulations of Al-5wt%Si downward solidification. (a) with shrinkage (simulation S4) (b) without shrinkage (simulation S5). The maximum magnitudes of flow velocity (m.s^{-1}) are presented at the bottom of each snapshot.

Figure 5 and Table 3 show that the velocity of the fluid flow for the simulation considering shrinkage (S4) is higher than that without shrinkage (S5). Also, in simulation S5 without the effect of shrinkage there are two circular flow regimes that develop during the initial and middle stages of solidification and one of them being much stronger than the other will dominate the entire domain in the final stages of solidification.

Table 3: Main differences in flow velocities between simulations S4 and S5 for downward solidification of Al-5wt%Si alloy shown in Figure 5.

Simulation	**Time (s)**	**Maximum Velocity ($mm.s^{-1}$)**	**Direction of Circular Flow Field.**
S4 With Shrinkage	5	0.122	Against direction of Gravity Vector
	25	4.10	Clockwise flow
	50	7.97	
	75	8.73	
	100	7.38	
S5 No Shrinkage	5	~0	No flow
	25	0.0028	Anti-Clockwise (stronger) and Clockwise (weaker)
	50	0.0302	Anti-Clockwise (stronger) and Clockwise (weaker)
	75	0.358	Anti-Clockwise Flow
	100	3.84	Anti-Clockwise Flow

The presence of shrinkage determines and affects the direction of the fluid flow during the initial stages of solidification and dictates the direction of the flow caused by natural convection. The stronger flow regime due to natural convection in simulation S5 (without shrinkage) is in the anti-clockwise direction which is opposite to that observed in S4 (with shrinkage), since flow induced by natural convection tends to go down in the direction of gravity at the middle of the domain ($r = 0$).

The flow velocity inside the mushy zone is significantly higher when shrinkage was considered because the effect of shrinkage is more pronounced inside the mushy zone. The flow induced by natural convection can hardly penetrate into the mushy zone because of the significantly higher pressure drop inside the mushy zone as compared to that in the liquid phase region [13].

The maximum flow velocity was always observed at the left top of the liquid region (centre of the solidifying cylinder) in simulation S4 for $t \geq 25s$ (Figure 5(a)). Fluid flow with higher temperatures from liquid region is driven into the mushy zone at this region. Therefore, solidification time increases and constant liquid fraction lines get closer to each other in this region. Further, with development of clockwise flow, direction of flow velocity at the liquid/mushy zone interface is predominantly in the positive r direction. This flow pattern creates accumulation of enthalpy in the right top side of the liquid region (at the wall of the solidifying cylinder). As a result, solidification in this region is delayed and the constant liquid fraction lines get closer to each other in this region, as shown in Figure 5(a) at t ≥ 50s. In Figure 5(b), due to the anticlockwise flow, accumulation of enthalpy occurs in the left top region of liquid side (centre of the solidifying cylinder), where the constant liquid fraction lines get closer at t ≥ 75s. However, at the right side of the liquid/mushy zone interface, liquid with high temperature is driven into the mushy zone, but the velocity at this region is low and hence there is no significant delay in solidification and hence, no significant compression of the constant liquid fraction lines, as shown in Figure 5(b). In conclusion, comparison of the results of simulations S4 and S5 shows that there is a significant variation in the magnitude and direction of flow velocity, significant variation in the development of the constant liquid fraction lines and solidification time.

The iso - normalized stream function lines at various solidification times are shown in Figure 6(a) and Figure 6(b) for simulations S4 and S5, respectively. Maximum magnitude of stream function (m^3/s) is shown below each snap shot. The solid black lines inside the computing domain represent the constant liquid fraction lines from $\phi = 0.9$ to $\phi = 0.1$. The maximum magnitude of stream function indicates the change in the strength of the flow field from weaker to stronger and back to weaker as solidification proceeds. One can easily note that there are significant variation in the magnitude and direction of the stream function with and without the effect of shrinkage during solidification. When the effect of shrinkage is ignored, fluid flow is significantly weaker and the pattern of circulation is significantly altered.

Figure 7 shows distribution of u_y and u_r as function of r at various locations of y at t = 50s for simulations S4 and S5. The maximum value of u_y is always higher than that of u_r in both cases. The maximum magnitude of velocity obtained in simulation S4 is higher than that in simulation S5, which indicates that shrinkage strengthened the fluid flow in addition to significantly altering the flow pattern.

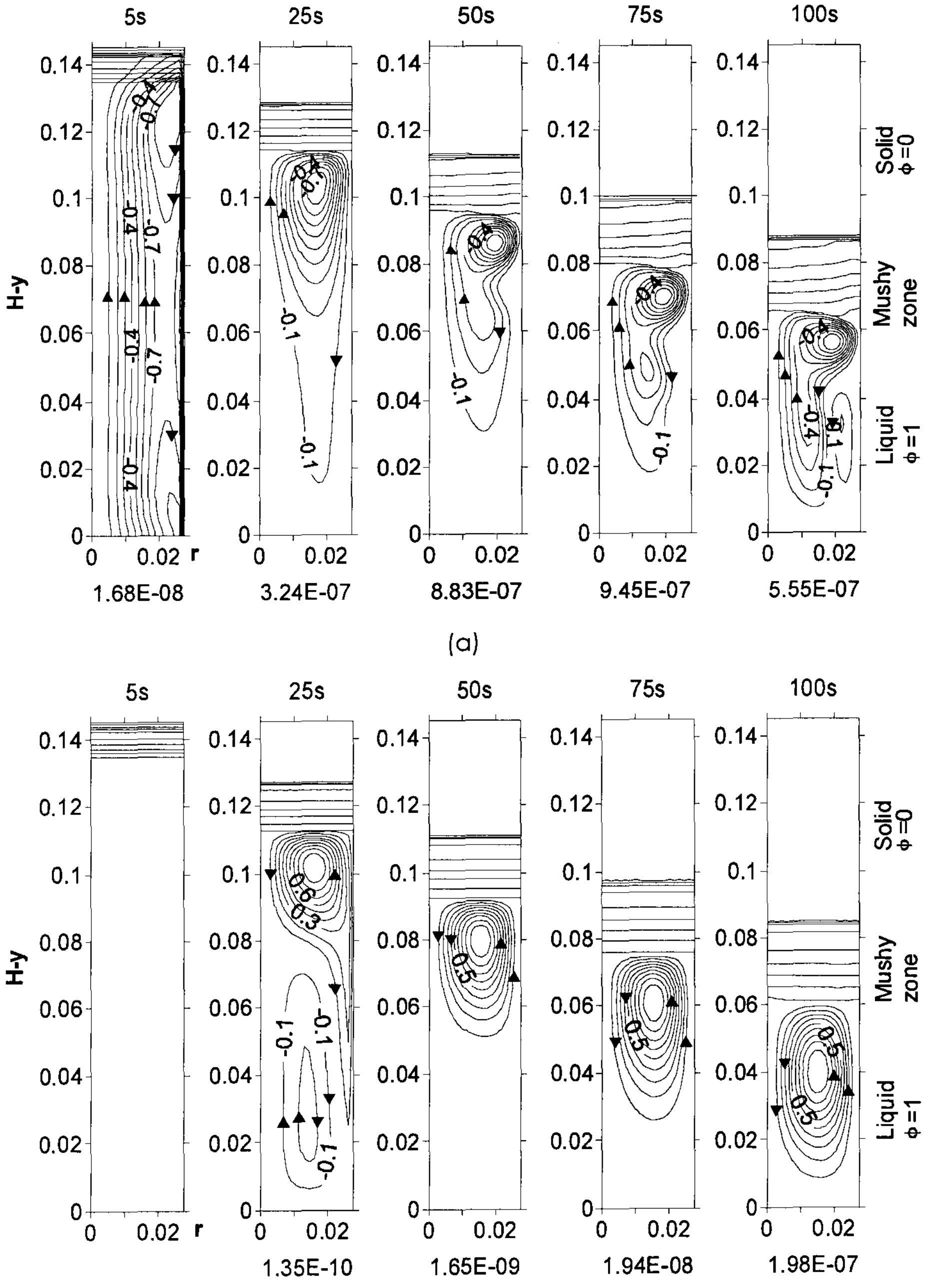

Figure 6: Normalized iso stream function lines during Al-5wt%Si downward solidification. (a) with shrinkage (Simulation S4) (b) without shrinkage (Simulation S5). The maximum magnitudes of stream function (m^3/s) are presented at the bottom of each snapshot, respectively.

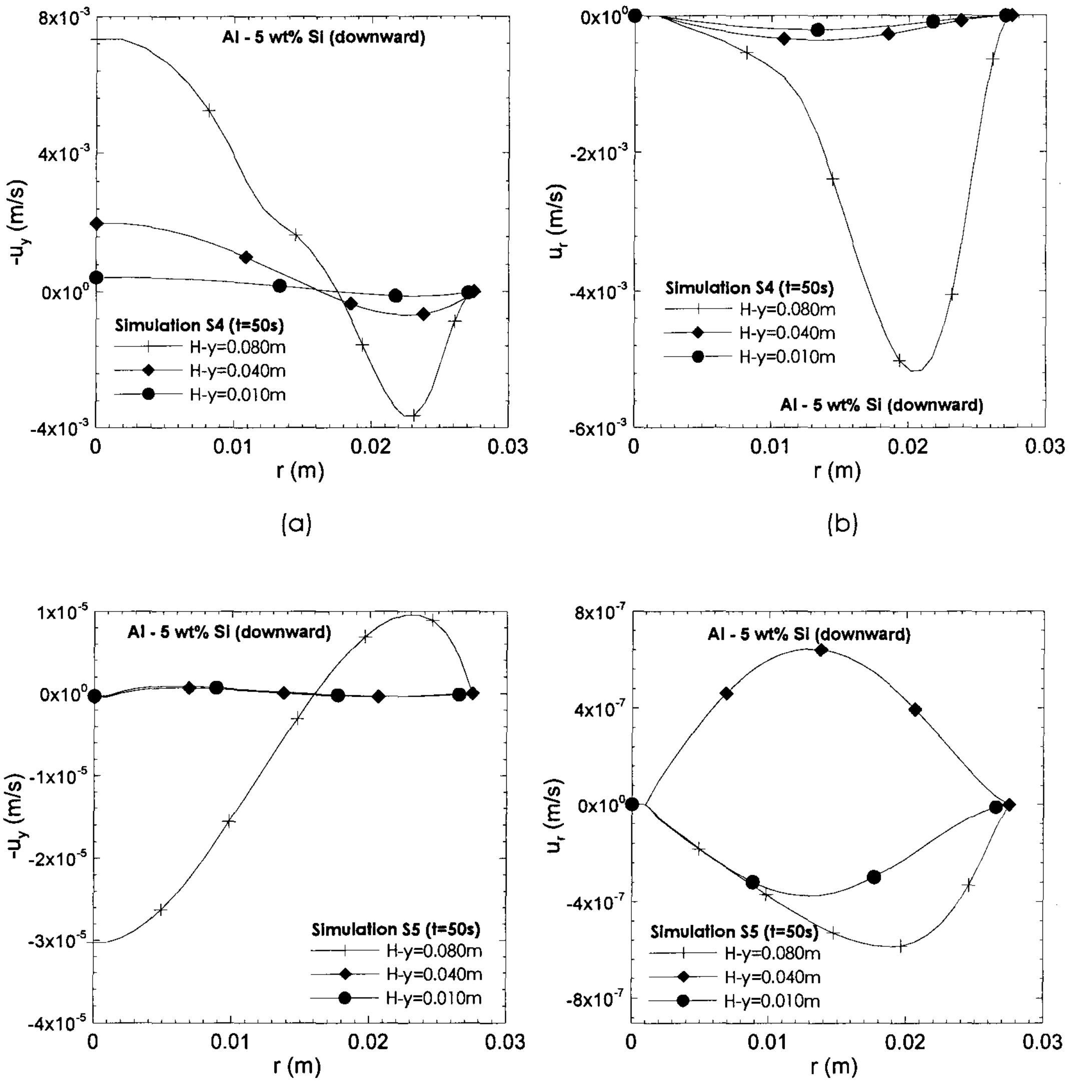

(a) (b)

(c) (d)

Figure 7: Flow velocity distribution at various locations of y during Al-5%wtSi downward solidification. (a) u_y at t = 50s for simulation S4 (with shrinkage); (b) u_r at t = 50s for simulation S4 (with shrinkage); (c) u_y at t = 50s for simulation S5 (without shrinkage); (d) u_r at t = 50s for simulation S5 (without shrinkage).

Effect of Shrinkage on Solidification Time

Figure 8 shows the effect of shrinkage on the solidification time (location of mushy zone/liquid interface with time). Figure 8 also shows the solidification time obtained from experiments [21, 22] for Al-3wt%Si (upward solidification) and Al-5wt%Si (downward solidification), respectively. In both cases of upward (Al-3wt%Si alloy) and downward (Al-5wt%Si alloy) solidification, considering shrinkage resulted in a better agreement with the experiment results.

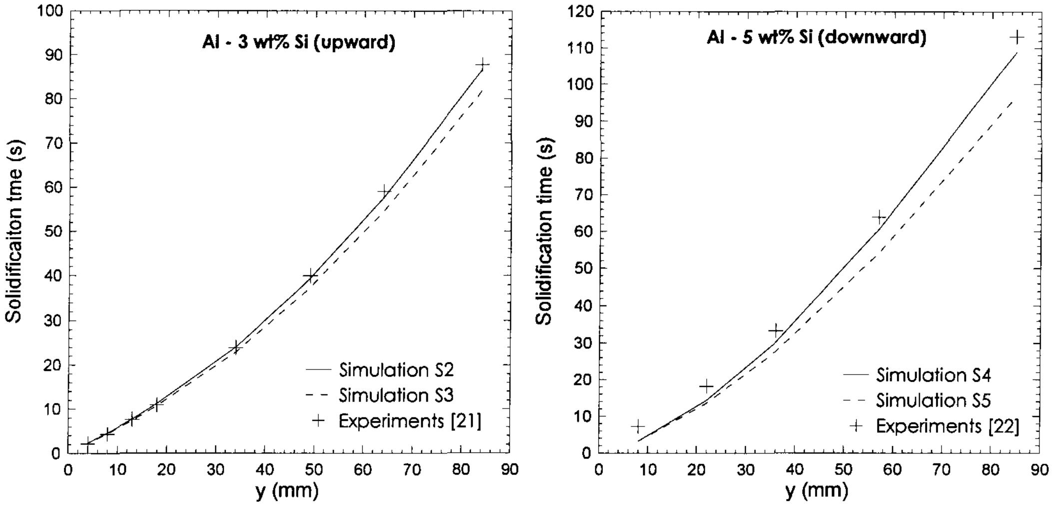

(a) (b)

Figure 8: Validation of solidification time for mushy zone/liquid interface locations with experiments [21, 22] (a) validation of S2 (with shrinkage) along with results from S3 (without shrinkage) and (b) validation of S4 (with shrinkage) along with results from S5 (without shrinkage).

In Figure 8, when shrinkage is considered, more high temperature liquid is entering the CV bringing in more heat into the CV and delaying solidification process. The fluid flow in the downward solidification mode (Figure 8(b)) is stronger than that in the upward solidification (Figure 8(a)) and hence, the delay in the solidification time of S4 compared with S5 is higher than the delay when S2 is compared with S3.

Effect of Shrinkage on R

Figure 9 shows the effect of shrinkage on the solidification velocity of the mushy zone/liquid interface, R. Figure 9(a) shows results of upward solidification of Al-3wt%Si alloy with shrinkage (S2) and without shrinkage (S3). Figure 9(b) shows similar results for downward solidification of Al-5wt%Si alloy. It is evident that simulations which considers shrinkage show lower values of R at all locations. Because shrinkage causes more liquid to enter the CV and hence, it delays the solidification process and reduces R. The value of R decreases more in the simulation with effect of shrinkage in the case of downward solidification (Figure 9(b)) when compared to the upward solidification (Figure 9(a)) because of the stronger fluid flow that occurs in downward solidification.

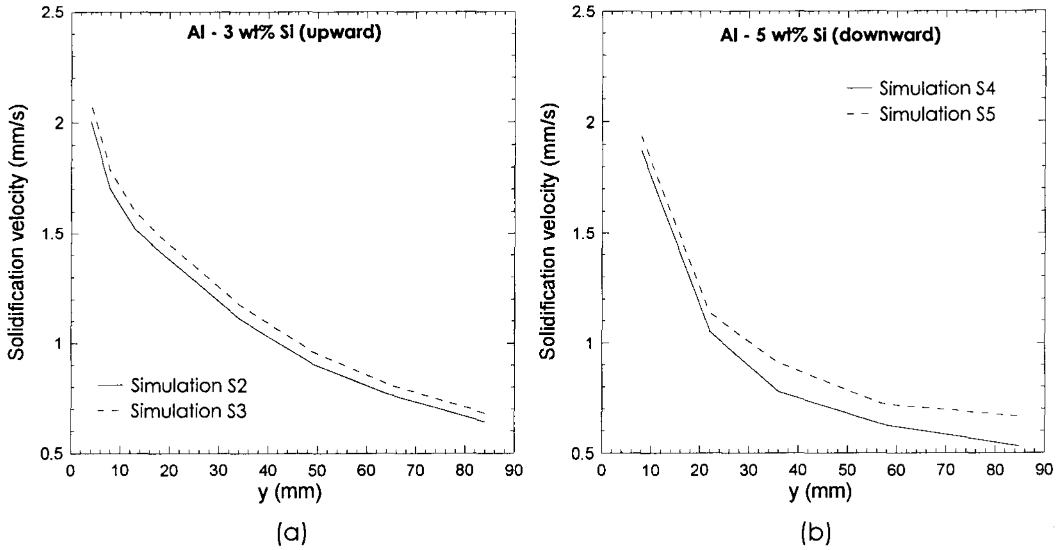

(a) (b)

Figure 9: Effect of shrinkage on solidification velocity, R (mm.s^{-1}) of the mushy zone/liquid interface during solidification simulations (a) S2 (with shrinkage) and S3 (without shrinkage); (b) S4 (with shrinkage) and S5 (without shrinkage).

Effect on Shrinkage on G

Figure 10 shows the effect of shrinkage on the temperature gradient prior the liquid at the mushy zone/liquid interface, G in the case of upward solidification of Al-3wt%Si alloy and downward solidification of Al-5wt%Si alloy, respectively. Results in Figure 10(a) indicate that the effect of shrinkage in the case of upward solidification has no discernible effect on the value of G because there is no significant fluid flow caused by shrinkage and there is no natural convection because the positive density gradient is in the direction of gravity.

In Figure 10(b) there are three distinct regions marked by points A, B, C and D. The times at which the mushy zone/liquid interface exists at these locations (solidification times) are also indicated in Figure 10(b) for simulation S4. Segment AB has no difference in the value of G because fluid flow is only due to shrinkage in simulation S4 and no discernible fluid flow in S5. Hence, there is no discernible difference in G in segment AB between times t_A = 3.2 s and t_B = 14.4 s. In the region marked by segment BC, fluid flow due to natural convection develops in both S4 and S5. However, fluid flow due to natural convection in S4 is significantly stronger (higher velocities) than that in S5, as shown in Figure 5 and Table 3. Furthermore, in S4, the high flow velocity fluid in the centre tends to flow into the mushy zone/liquid interface as compared to the high velocity fluid tending to flow away from the mushy zone/liquid interface (Figure 5 and Table 3). The flow in S4 brings in more volume of hotter liquid into the mushy zone/liquid interface when compared to that in S5 and hence, the temperature gradient in S4 increases in the region marked by segment BC in Figure 10(b) and changes the value of G moderately in S4. In the region marked by segment CD, the stronger fluid flow due to natural convection in S4 equalizes the temperatures between liquid at the mushy zone/liquid interface and the bulk liquid faster than that in S5 where the fluid flow due to natural convection is weaker. Hence, in segment CD of Figure 10(b) the decrease in the value of G is greater for S4 (with shrinkage) than that for S5 (no shrinkage).

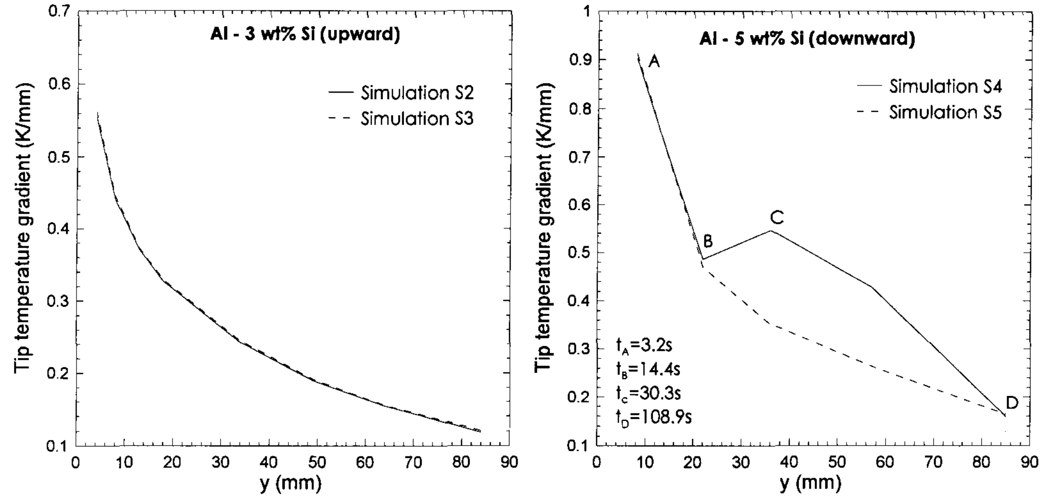

(a) (b)

Figure 10: Effect of shrinkage on the temperature gradient in front of the solidification even, G (K.s^{-1}) during solidification simulations (a) S2 (with shrinkage) and S3 (without shrinkage); (b) S4 (with shrinkage) and S5 (without shrinkage).

Effect of Shrinkage on λ_1

Figure 11 shows the effect of shrinkage during upward solidification of Al-3wt%Si alloy on the primary arm spacing as function of the instantaneous cooling rate (G.R) (°C/s) and the location y (mm). Also shown in Figure 11 are the primary dendrite arm spacing from experiments [21]. Figure 11(a) shows that there is no discernible difference with the effect of shrinkage during upward solidification because of the absence of any significant fluid flow due to shrinkage and absence of any fluid flow due to natural convection. Figure 9(a) shows that the value of R between simulations S2 and S3 has a maximum of 6% variation when shrinkage was considered and Figure 10(a) shows no discernible variation in the value of G when shrinkage was considered. The values of λ_1 calculated using results of simulations S2 and S3 are lower than the values measured by experiments. One of the reasons for this is that in the experiments [21] the instantaneous cooling rate was measured immediately after the liquidus temperature which will over-predict the value of the cooling rate and hence the simulations in Figure 11(a) seem to under-predict the values of λ_1. In Figure 11(b), the values of λ_1 from S2 and S3 are shown along with the experiment values [21] as function of y. The values of λ_1 obtained from the simulations S2 and S3 are in good agreement with the values obtained at the various respective locations in the experiments.

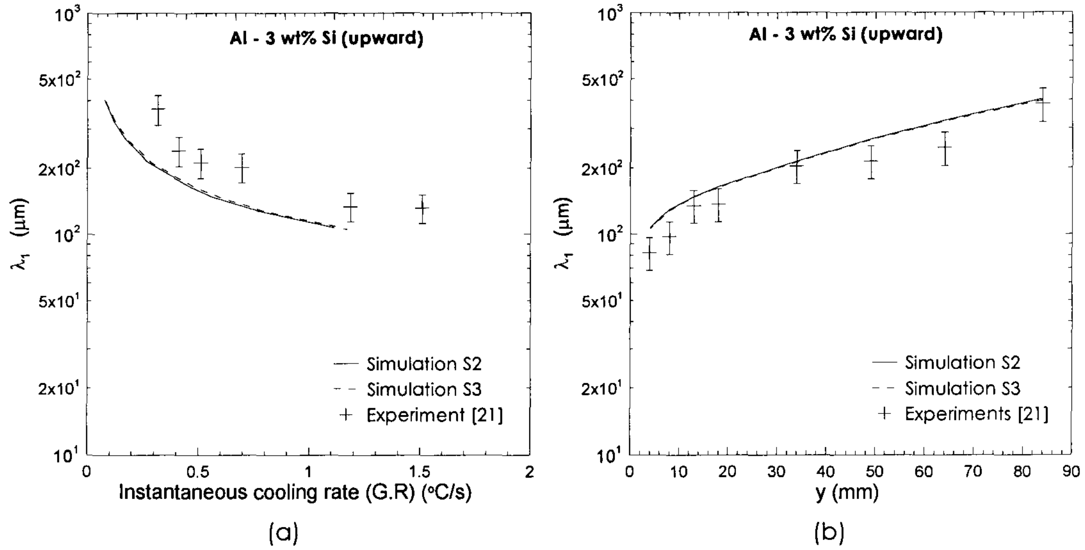

Figure 11: Effect of shrinkage on primary dendrite arm spacing during Al-3wt%Si upward solidification for cases S2 (with shrinkage) and S3 (without shrinkage). (a) As function of instantaneous cooling rate at the mushy zone/liquid interface, (G.R), (°C/s) and (b) As function of y (mm).

Figure 12 shows the values of λ_1 calculated from simulations S4 and S5 for the downward solidification of Al-5wt%Si alloy along with results of λ_1 from experiments [22] as function of the instantaneous cooling rate of the liquid at the mushy zone/liquid interface (G.R) (°C/s) and as function of y (mm). Figure 12 shows three distinct regions marked by points A, B, C and D. As discussed in the previous section on the effect of shrinkage on G, segment AB marks the region where fluid flow in the liquid is mostly dominated by shrinkage. Segment BC marks the region wherein natural convection develops a stronger fluid flow and segment CD marks the region where fluid flow developed by natural convection gets weaker. In Figure 12(a), the values of λ_1, evaluated by simulation S4, will increase as a function of (G.R) in segment AB because the value of G and R both decrease without any significant fluid flow in the domain causing an increase in λ_1, as suggested by Equations (10) and (11). Similarly, Figure 12(b) shows that the values of λ_1 in segment AB increase with y because the value of (G.R) decreases with y. Segment BC marks the region where the value of G increases significantly (simulation S4) with the effect of shrinkage (Figure 10(b)). In simulation S5, without the effect of shrinkage, the value of G continues to decrease at a slower rate than in segment AB. Hence in segment BC, the value of λ_1 evaluated from simulation S4 (with shrinkage) will decrease as function of (G.R) and y, while it will increase with a slower rate than in segment AB for the case with no shrinkage (S5). In segment CD, the value of G again decreases as function of y (Figure 10(b)). The decrease in G is faster in S4 than that in S5. Hence, in segment CD, the value of λ_1 will increase faster for S4 than that in S5 as a function of (G.R) and y.

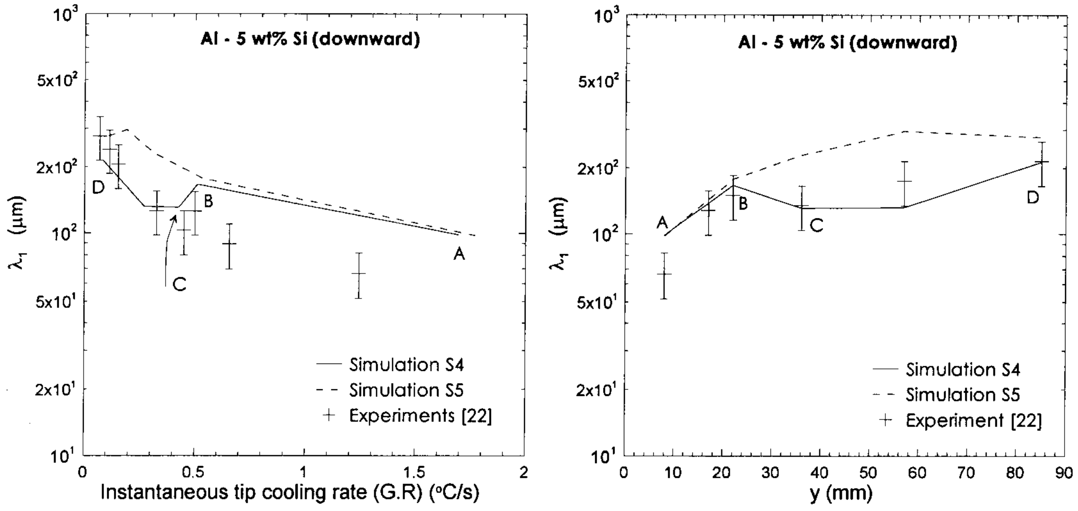

(a) (b)

Figure 12: Effect of shrinkage on the primary dendrite arm spacing during Al-5wt%Si downward solidification for cases S4 (with shrinkage) and S5 (without shrinkage). (a) As function of instantaneous cooling rate at the mushy zone/liquid interface, (G.R), (°C/s) and (b) As function of y (mm).

Figure 12(b) shows that there is a good agreement between results of simulation S4 (with shrinkage) and the experiment results for λ_1 [22]. The agreement is to the extent that the three regions marked by segments AB, BC and CD are clearly defined by both the experiments and the simulation alike. Simulation S5 could not define the three regions clearly because of the weaker fluid flow due to the absence of shrinkage. In Figure 12(b) there is a deviation of the experiment results for λ_1 as function of instantaneous cooling rate (G.R) at higher values of (G.R) (beginning of the solidification process). Such deviation is expected because the experimental [22] evaluation of the cooling rate is tedious due to high values of R experienced during the initial stages of downward solidification (refer to Figure 9).

SUMMARY AND CONCLUSIONS

Upward solidification of Al-3wt%Si alloy and downward solidification of Al-5wt%Si and Al-7wt%Si alloys were numerically simulated. Numerical results of transient temperature distribution, solidification time at the mushy zone/liquid interface and primary arm spacing were validated by experiments [21, 22]. Fluid flow due to solidification shrinkage was considered for both the upward and downward solidification modes. Further, flow velocity distribution, G, and R were quantified.

This study showed that considering the fluid flow caused by solidification shrinkage does not have a significant effect on the solidification parameters such as G, R, solidification time and λ_1 during the upward solidification mode. However, it is critical to consider the effect of shrinkage during solidification simulation of the downward and horizontal solidification processes, wherein the effect of density gradient in the liquid phase induces natural convection phenomenon causing strong fluid flow fields in the solidifying domain.

Considering the effect of fluid flow caused by shrinkage in the downward solidification increases the magnitude of the velocity of fluid flow and reverses the direction of the flow field, thereby resulting in smaller primary dendrite arm spacing, λ_1. Further, when the fluid flow changed from shrinkage dominated to natural convection dominated during the solidification process, the flow velocity dramatically increased in a short interval, thereby causing the value of λ_1 to abnormally and significantly decrease during this short time interval. This abnormal reversal in the trend of λ_1 was not observed when fluid flow caused by solidification shrinkage was not considered in the simulations. Considering shrinkage in the solidification simulation decreases the liquid/mushy zone interface velocity for both upward and downward solidification simulations and has a significant effect on the temperature gradient in the liquid at the liquid/mushy zone interface during the downward solidification mode, but has a negligible effect on this temperature gradient during the upward solidification mode. Further, fluid flow due to shrinkage significantly changes the location and contours of the constant liquid fraction lines developed in the mushy zone during solidification.

REFERENCES

[1] JMatPro, 4.1 ed Guildford ,UK.: Sente Software Ltd.

[2] D. P. Sekulic, P. K. Galenko, M. D. Krivilyov, L. Walker, and F. Gao, "Dendritic growth in Al-Si alloys during brazing. Part 2: Computational modeling," *International Journal of Heat and Mass Transfer*, vol. 48, pp. 2385-2396, 2005.

[3] Factsage, 5.5 ed Madison, WI, USA.: Computherm LLC.

[4] M. Gunduz and J. D. Hunt, "The measurement of solid-liquid surface energies in the Al-Cu, Al-Si and Pb-Sn systems," *Acta Metallurgica*, vol. 33, pp. 1651-1672, 1985.

[5] W. D. Bennon and F. P. Incropera, "A continuum model for momentum, heat and species transport in binary solid – liquid phase change systems - I. Model formulation," *International Journal of Heat and Mass Transfer*, vol. 30, pp. 2161-2170, 1987.

[6] S. D. Felicelli, J. C. Heinrich, and D. R. Poirier, "Simulation of freckles during vertical solidification of binary alloys," *Metallurgical Transactions B (Process Metallurgy)*, vol. 22, pp. 847-859, Dec. 1991.

[7] V. R. Voller and C. Prakash, "Fixed grid numerical modeling methodology for convection - diffusion mushy region phase – change problems," *International Journal of Heat and Mass Transfer*, vol. 30, pp. 1709-1719, 1987.

[8] H. Wang, S. Shankar, and M. S. Hamed, "Numerical model for binary alloy solidification," in *5th International Conference on Computational Heat and Mass Transfer*, Canmore, Canada, 2007, pp. 345-351.

[9] W. D. Bennon and F. P. Incropera, "Numerical analysis of binary solid – liquid phase change using a continuum model," *Numerical Heat Transfer*, vol. 13, pp. 277-296, 1988.

[10] S. D. Felicelli, J. C. Heinrich, and D. R. Poirier, "Numerical models for dendritic solidification of binary alloys," *Numerical Heat Transfer, Part B: Fundamentals,* vol. 23, pp. 461-481, 1993.

[11] J. C. Heinrich and D. R. Poirier, "The effect of volume change during directional solidification of binary alloys," *Modeling and Simulation in Materials Science and Engineering,* vol. 12, pp. 881-899, Sep. 2004.

[12] E. McBride, J. C. Heinrich, and D. R. Poirier, "Numerical simulation of incompressible flow driven by density variations during phase change," *International Journal for Numerical Methods in Fluids,* vol. 31, pp. 787-800, Nov. 1999.

[13] D. XU and Q. LI, "Gravity- and solidification-shrinkage-induced liquid flow in a horizontally solidified alloy ingot," *Numerical Heat Transfer: An International Journal of Computation and Methodology,* vol. Part A: Applications, 20, pp. 203-221, 1991.

[14] K. C. Chiang and H. L. Tsai, "Shrinkage-induced fluid flow and domain change in two-dimensional alloy solidification " *International Journal of Heat and Mass Transfer,* vol. 35, pp. 1763-1770, 1992.

[15] K. C. Chiang and H. L. Tsai, "Interaction between shrinkage-induced fluid flow and natural convection during alloy solidification," *International Journal of Heat and Mass Transfer,* vol. 35, pp. 1771-1778, 1992.

[16] M. J. M. Krane and F. P. Incropera, "Analysis of the effect of shrinkage on macrosegregation in alloy solidification," *Metallurgical and Materials Transactions A: Physical Metallurgy and Materials Science,* vol. 26A, pp. 2329-2339, 1995.

[17] S. Steinbach and L. Ratke, "The effect of rotating magnetic fields on the microstructure of directionally solidified Al-Si-Mg alloys," *Materials Science and Engineering A,* vol. 413-414, pp. 200-204, Dec. 15 2005.

[18] T. Magnusson and L. Arnberg, "Density and solidification shrinkage of hypoeutectic aluminum-silicon alloys," *Metallurgical and Materials Transactions A: Physical Metallurgy and Materials Science,* vol. 32, pp. 2605-2613, Oct. 2001.

[19] M. C. Schneider and C. Beckermann, "Formation of macrosegregation by multicomponent thermosolutal convection during the solidification of steel," *Metallurgical and Materials Transactions A (Physical Metallurgy and Materials Science),* vol. 26A, pp. 2373-2388, 1995.

[20] M. C. Schneider and C. Beckermann, *Summary of a method for numerically simulating the columnar dendritic solidification of binary alloys* vol. UIME-CB01-1993. Department of Mechanical Engineering, University of Iowa, Iowa City, 1993.

[21] M. D. Peres, C. A. Siqueira, and A. Garcia, "Macrostructural and microstructural development in Al-Si alloys directionally solidified under unsteady-state conditions," *Journal of Alloys and Compounds,* vol. 381, pp. 168-181, November 3 2004.

[22] J. E. Spinelli, M. D. Peres, and A. Garcia, "Thermosolutal convective effects on dendritic array spacings in downward transient directional solidification of Al-Si alloys," *Journal of Alloys and Compounds,* vol. 403, pp. 228-238, Novermber 2005.

[23] M. C. Flemings, *Solidification processing.* New York, NY.: McGraw-hill Book Co., 1974.

[24] M. H. Burden and J. D. Hunt, "Cellular and dendritic growth. I," *Journal of Crystal Growth*, vol. 22, pp. 99-108, 1974.

[25] M. H. Burden and J. D. Hunt, "Cellular and dendritic growth. II," *Journal of Crystal Growth*, vol. 22, pp. 109-116, 1974.

[26] P. C. Carman, "Fluid flow through granular beds," *Trans. Inst. Chem. Engs.*, vol. 15, pp. 150-156, 1937.

[27] P. C. Carman, "The determination of the specific surface of powders " *I. J. Soc. Chem. Indus.*, vol. 57, pp. 225-234, 1938.

[28] S. Asai and I. Muchi, "Thearoetical analysis and model experiments of the formation mechanism of channel - type segregation," *Transactions of the Iron and Steel Institute of Japan*, vol. 18, pp. 290-298, 1978.

[29] D. Bouchard and J. S. Kirkaldy, "Prediction of dendrite arm spacings in unsteady- and steady-state heat flow of unidirectionally solidified binary alloys," *Metallurgical and Materials Transactions B (Process Metallurgy and Materials Processing Science)*, vol. 28B, pp. 651-663, Aug. 1997.

[30] P. Lehmann, R. Moreaub, D. Camela, and R. Bolcatob, "A simple analysis of the effect of convection on the structure of the mushy zone in the case of horizontal Bridgman solidification. Comparison with experimental results," *Journal of Crystal Growth*, vol. 183, pp. 690-704, 1998.

[31] H. Wang, "Solidification Simulation of Binary Al-Si Alloys: Prediction of Primary Dendrite Arm Spacing with Macro-scale Simulations (~1mm Length Scale)," in *Department of Mechanical Engineering* McMaster University, Hamilton, Ontario, Canada, Ph. D. Thesis, 2009.

[32] H. Wang, "Solidification Simulation of Binary Al-Si Alloys: Prediction of Primary Dendrite Arm Spacing with Macro-scale Simulations (~1mm Length Scale)," in *Department of Mechanical Engineering, McMaster University*, Hamilton, Ontario, Canada, Publication A, Ph. D. Thesis, 2009.

INTERACTION BETWEEN PRIMARY DENDRITE ARM SPACING AND VELOCITY OF FLUID FLOW DURING SOLIDIFICATION OF Al-Si BINARY ALLOYS.

Hongda Wang[1,2], Mohamed S. Hamed[1], Sumanth Shankar[2,*]
[1]Thermal Processing Laboratory (TPL)
[2]Light Metal Casting Research Centre (LMCRC)
McMaster University, Hamilton, ON, Canada L8S 4L7

ABSTRACT

The interaction between the primary arm spacing, λ_1 and fluid flow is critical to fully understand the fluid flow development in unsteady state solidification of binary alloys with continuously changing values of the primary dendrite arm spacing, λ_1. Present numerical models can be divided into two parts: *macro (~1mm length scale) simulations and micro (~1 μm length scale) evaluations.* In the macro-scale simulations of the present study, the energy, concentration, momentum and continuity equations were solved by using the finite-volume method. Temperature and liquid concentration inside the mushy zone were coupled by local equilibrium assumptions. Energy equation was applied to determine liquid fraction inside mushy zone while considering the undercooling of the liquid temperature at the mushy zone/liquid interface. Momentum and continuity equations were coupled by the SIMPLE algorithm. In the micro-scale evaluations, parameters from the macro-scale simulations were applied to evaluate λ_1. Several theoretical and empirical models for the evaluation of λ_1 were analyzed and compared. It was found that the model specified for the unsteady state solidification process combined with the effect of fluid flow (simulated in macro-scale) could best evaluate λ_1. Results from the macro-scale simulation and micro –scale evaluation, such as transient temperature, solidification time and λ_1, were validated by experiments. Macro-scale simulations have been carried out under various experimental conditions to generate certain types of fluid flow regimes in the solidifying domain and their effects on λ_1 were investigated. Further, metallographic results from uni-directional solidification simulations of Al-Si hypoeutectic alloys were used to evaluate the effect of using instantaneous λ_1 values at each time step or one constant value of λ_1 for the complete simulation, on the development of transient fluid flow regimes in the domain. Using any constant value of λ_1 from the observed range of transient values obtained from the simulations did not have any appreciable effect on the G, R and magnitude and/or type of fluid flow regimes developed in the domain. However, it was also observed that changing the type and magnitude of fluid flow in the domain had a significant effect on the transient values of λ_1, G and R during downward solidification. From the results of this study, it was recommended that during micro –scale simulations of unsteady state binary alloy downward solidification, the type and magnitude of fluid flow regimes during downward solidification

---

[*] Corresponding Author: shankar@mcmaster.ca , voice: (905) 512-1324

should be evaluated from a macro-scale simulation study at each time step to estimate a valid value for λ_1.

NOMENCLATURE

c_{ps}	Specific heat of solid as a function of temperature (J Kg^{-1} K^{-1}) [1];
c_{pl}	Specific heat of liquid (J Kg^{-1} K^{-1}) [1];
C_L	Liquid concentration (wt%);
C_o	Average alloy composition (wt%);
C_S	Solid concentration (wt%);
D	Solute diffusivity coefficient of liquid (6.25×10^{-9} (m^2 s^{-1})) [2];
G	Temperature gradient in liquid at the mushy zone/liquid interface (°C mm^{-1});
k	Average partition coefficient (0.116) [3];
K_s	Thermal conductivity of solid as a function of temperature (W m^{-1} K^{-1}) [1];
K_l	Thermal conductivity of liquid (W m^{-1} K^{-1}) [1];
L	Latent heat of fusion (J Kg^{-1}) [3];
m	The slope of liquidus line (– 6.675 (K $wt\%^{-1}$)) [3];
p	Pressure(Pa);
R	Velocity of mushy zone/liquid interface (mm s^{-1});
t	Time (s);
T	Temperature (°C);
T_{liq}	Liquidus temperature (°C) [3];
T_{ini}	Initial temperature of liquid (°C);
T_m	Melting temperature of pure aluminum (660 °C) [3];
T_{eut}	Eutectic temperature (578.6 °C) [3];
$\dot{T}$	Instantaneous tip cooling rate = G×R (°C s^{-1});
ΔT	Undercooling of T_{liq} (°C);
U_r	Velocity in r direction (mm.s^{-1});
U_y	Velocity in y direction (mm.s^{-1});
U	Flow velocity in the liquid of mushy zone/liquid interface (mm.s^{-1});
β	Contraction ratio $\left[\beta=\frac{\rho_s-\rho_l}{\rho_l}\right]$ (volumetric shrinkage during solidification) [1];
β_C	Solute expansion coefficient (-4.26×10^{-4} (K^{-1})) [1];
β_T	Thermal expansion coefficient (1.39×10^{-4} (K^{-1})) [1];
Γ	Gibbs-Thomson coefficient (1.97×10^{-7} (K m^{-1})) [4];
ϕ	Liquid fraction;
ρ_l	Liquid density (Kg m^{-3}) [1];
ρ_s	Solid density (Kg m^{-3}) [1];
μ	Dynamic viscosity 1.3×10^{-3} (Pa s) [1];
λ_1^0	Primary arm spacing if no fluid flow effect is considered (µm);
λ_1	Primary arm spacing (µm);

THERMO-PHYSICAL MATERIAL PROPERTIES

Properties	Al-3wt%Si	Al-5wt%Si	Al-7wt%Si
K_s	228.08 – 0.061055×T	226.01-0.077488×T	223.93-0.093920×T
K_l	85.476	84.568	83.661
C_{ps}	887.23+0.50227×T	883.54+0.50227×T	879.85+0.50227×T
C_{pl}	1168.9	1163.7	1158.6
ρ_s	2627.9	2621.6	2614.5
ρ_l	2415.0	2422.8	2430.6
L	4.05×10^5	4.25×10^5	4.45×10^5

INTRODUCTION

The mechanical properties and performance of a cast component is largely dependent and highly sensitive to the microstructure details, specifically the primary dendrite arm spacing, λ_1 and secondary arm spacing, λ_2 [5, 6]. Solidification simulations have been traditionally carried out in two length scales: Micro-simulation (control volume ≤ 10 μm) and macro-simulation (control volume ~ 1 mm). During solidification of binary alloys, there is fluid flow in the solidifying domain caused by shrinkage due to volume changes during solidification and natural convection due to density gradient in the liquid phase. Traditionally, the macro-simulation is able to quantify the fluid flow regimes but does not enable estimation of microstructure features such as λ_1 [7-18]. Similarly, the micro-simulation can evaluate λ_1 but does not enable estimation of the fluid flow regimes [19-24] because the length scales for continuity of the fluid –flow regimes is in the macro-scale and that of λ_1 is in the micro-scale.

A complete and valid solidification simulation can only be possible if the macro- and micro-simulations are merged together. This is possible by quantifying the fluid flow regimes by the macro-simulations and input the results into the micro-simulation to quantify the transient values of λ_1. Conventional micro-simulations assume arbitrary types and magnitudes of fluid flow regimes in the computing domain to study the effect of fluid flow on the resultant values of λ_1 [25, 26].

Although the merger of the macro- and micro-simulations is still an issue of the future, this study is directed to quantify the effect of fluid flow types and magnitudes on the resultant transient values of λ_1 and vice-versa. The various transient values λ_1 used in the macro-simulation were obtained from empirical and theoretical models proposed by various researchers[27, 28]. Some of the popular empirical models to evaluate λ_1 from estimated values of temperature gradient of the liquid at the mushy zone/liquid interface, G and the velocity of the mushy zone/liquid interface, R have been verified by macro-scale solidification simulations and experimental results. The magnitude and type of fluid flow in the computing domain significantly influences the estimation of G and R.

Al-Si hypoeutectic alloys are one of most commonly used casting alloys and hence, Al-3wt%Si and Al-5wt%Si alloys were used in this study for the simulations. Further, reliable experiment results for these two alloys were readily available [29, 30].

Wang et al [31] has presented a comprehensive summary of the previous research efforts on macro-simulations of solidification of binary alloys. These efforts have not been able to predict λ_1 because simulations could not be successfully validated by experiments with transient temperature. There are two reasons for this, one being that none of the previous macro-simulation studies had considered the undercooling of the liquidus temperature prior to the solidification event, ΔT because the energy equation was solved first and subsequently the mass conservation equation was solved to determine the solute concentration and liquid fraction in the mushy zone (solid and liquid co-exist). Since the magnitude of the diffusion coefficient of the solute atoms in the liquid phase is four orders lower than the thermal diffusivity, considering ΔT was not feasible. In the present new approach presented by Wang et al [31], the mass concentration equation is solved first followed by the solution of the energy equation. The energy equation was solely used to evaluate the liquid fraction in the mushy zone, enabling the use of ΔT during solidification. The other reason for the previous macro-scale solidification simulations not to be validated by experiments is that the thermo-physical material properties were mostly considered as constants in the respective liquid and solid phases and this was shown to be erroneous by Wang et al [32], who demonstrated that the material properties of the solid phases have to be considered as function of temperature (not constant).

Four popular empirical models [27, 33-35] for the estimation of λ_1 were used independently in this study. Equations (1) to (4) present these four models. Equations (1) to (3) estimate the values of λ_1 in a steady state solidification process and Equation (4) for an unsteady state process. Steady state solidification means that G and R are kept constant during solidification. However, during unsteady solidification, G and R change (present investigation in either upward or downward solidification). In Equation (4), $G_{0\varepsilon}$ is a characteristic parameter ≈ 360 K mm^{-1} [27], coefficient a1 = 250. L_T is a constant that depends on harmonic perturbations and is equal to 28 [30] for dendritic growth according to Trivedi model [35]. Furthermore, Equations (1) to (4) do not include the effect of fluid velocity in estimating λ_1. Lehmann et al [28] proposed a model to include the effect of fluid velocity using any of the values of λ_1^0 obtained from Equations (1) to (4). Equation (5) enables the evaluation of λ_1 with the effect of fluid flow in the solidifying domain. Each value of λ_1^0 estimated from Equations (1) to (4) will be individually introduced in Equation (5) to evaluate λ_1 with the effect of fluid flow distribution.

$$\lambda_1^0 = 2.83[m(k-1)D\Gamma]^{0.25} C_o^{\frac{1}{4}} R^{-\frac{1}{4}} G^{-\frac{1}{2}} \qquad \text{Hunt Model[33]} \tag{1}$$

$$\lambda_1^0 = 4.3[m(k-1)D\Gamma / k^2]^{0.25} C_o^{\frac{1}{4}} R^{-\frac{1}{4}} G^{-\frac{1}{2}} \qquad \text{Kurz – Fisher Model [34]} \tag{2}$$

$$\lambda_1^0 = 2.83[m(k-1)D\Gamma L_T]^{0.25} C_o^{\frac{1}{4}} R^{-\frac{1}{4}} G^{-\frac{1}{2}} \qquad \text{Trivedi Model [35]} \tag{3}$$

$$\lambda_1^0 = a1\left(\frac{16C_o^{\frac{1}{2}} G_o \varepsilon \Gamma D}{(1-k)mGR}\right)^{\frac{1}{2}} \qquad \text{Bouchard- Kirkaldy Model [27]} \tag{4}$$

$$\lambda_1 = \lambda_1^0 \left(1 + \frac{U}{R}\right)^{-\frac{1}{2}} \qquad \text{Lehmann Model [28]} \tag{5}$$

Lehmann et al [28] theoretically analyzed the effects of fluid flow induced by an external magnetic field on the value of λ_1. Theoretical data for λ_1 was compared with experimental results obtained from solidification of Cu – 60 wt% Ag and Al – 10wt% Cu alloys. It was reported that an increase of the ratio of fluid velocity and solidification velocity would decrease λ_1. Equation (5) has also been validated with experiment results from solidification of commercial A357 (Al–Si–Mg) alloy with fluid flow induced by an external magnetic field [36].

DOMAIN DEFINITION

Figure 1 shows the schematics of the two types of solidification and the corresponding computing domains considered in this study. Figure 1 also shows the direction of the heat extraction, $\vec{q}$ and the gravity vector, $\vec{g}$. The domain in Figure 1(a) is for upward solidification wherein the heat extraction in the same direction of the gravity vector. Boundary conditions for C_L and T are also shown in Figure 1(a). There is no natural convection in this case because the density gradient is positive in the direction of the gravity vector [13]. The domain in Figure 1(b) is for downward solidification wherein the heat extraction is in the opposite direction to gravity vector. Boundary conditions for C_L and T are also shown in Figure 1(b), the functions will be given in next section. In this case, there is natural convection in the liquid phase and mushy zone because the density gradient is positive against the direction of the gravity vector [13]. Solid phase may re-melt due to convective currents in the liquid region. All dimensions used in simulations were similar to those reported in the experimental studies by Peres et al [29] and Spinelli et al [30]. The simulation geometry is a cylinder with a diameter of 55 mm and height of 145 mm. The computing domain in Figure 1 is a two-dimensional cross-section of the geometry, and owing to symmetry only one half of the cylinder was considered in the simulations. Al – Si alloy melt with a marginal superheat temperature was considered in this study.

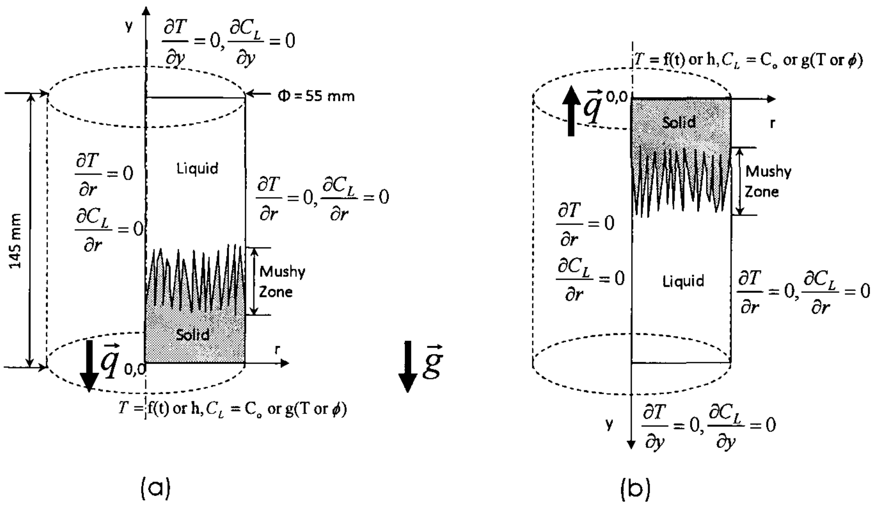

Figure 1: Schematic and boundary conditions for C_L and T during the solidification simulations. (a) upward solidification and (b) downward solidification. Dimensions of geometry shown in (a) and (b) are identical.

Governing Equations

The governing equations of solidification taking place in the geometry shown in Figure 1 are presented in this section. The energy equation is presented in Equation (6) and the concentration equation in Equation (7).

$$\overbrace{\frac{\partial((\phi\rho_l c_{pl}+(1-\phi)\rho_s c_{ps})T)}{\partial t}}^{\text{Transient Term}}+\overbrace{\rho_l c_{pl}u_r\frac{\partial T}{\partial r}+\rho_l c_{pl}u_y\frac{\partial T}{\partial y}}^{\text{Convection Term}}+\overbrace{\rho_s L\frac{\partial\phi}{\partial t}}^{\text{Phase Transformation Term}}$$

$$=\underbrace{\frac{1}{r}\frac{\partial}{\partial r}(r(\phi K_l+(1-\phi)K_s)\frac{\partial T}{\partial r})+\frac{\partial}{\partial y}((\phi K_l+(1-\phi)K_s)\frac{\partial T}{\partial y})}_{\text{Diffusion Term}} \tag{6}$$

$$\overbrace{\frac{\partial(\phi\rho_l C_L+(1-\phi)\rho_s C_S)}{\partial t}}^{\text{Transient Term}}+\overbrace{\rho_l u_r\frac{\partial C_L}{\partial r}+\rho_l u_y\frac{\partial C_L}{\partial y}}^{\text{Convection Terms}}$$

$$=-\rho_l[\underbrace{\beta C_L\frac{\partial\phi}{\partial t}}_{\substack{\text{Source Term}\\\text{from Shrinkage}}}\underbrace{-D(\frac{1}{r}\frac{\partial}{\partial r}(\phi r\frac{\partial C_L}{\partial r}))-D\frac{\partial}{\partial y}(\phi\frac{\partial C_L}{\partial y})}_{\text{Diffusion Term}}] \tag{7}$$

Temperature of the control volume(CV) in the mushy zone was determined by Equation (8) wherein local equilibrium conditions were assumed [37].

$$T=T_m+mC_L \tag{8}$$

If there is no re-melting of solid, the average solute concentration of the solid phase in any CV was evaluated by Equation (9).

$$C_S = \frac{1}{1-\phi}\int_{\phi}^{1} kC_L d\phi \tag{9}$$

Re-melting is the phenomenon that the already solidified solid phase is melted inside CV during solidification procedure. This may occur because the convective current with higher temperature is flowed into this CV. If re-melting of solid occurs, Cs must be taken from the history of Cs during solidification [38]. During solidification procedure as solid phase inside CV keeps on growing (no re-melting), the magnitude of Cs has to be recorded with the decreasing of ϕ from the first piece of solid at the beginning of solidification according to equation (9). As re-melting occurs, Cs need to be obtained from the recorded history according to the different ϕ instead of directly applying equation (9).

Mass conservation is presented in Equation (10).

$$\frac{1}{r}\frac{\partial(ru_r)}{\partial r} + \frac{\partial u_y}{\partial y} = \beta\frac{\partial\phi}{\partial t} \tag{10}$$

The momentum equations in the r and y directions defined in Figure 1 are presented in Equations (11) and (12), respectively.

$$\begin{aligned}\rho_l\frac{\partial u_r}{\partial t} + \rho_l\frac{u_r}{\phi}\frac{\partial u_r}{\partial r} + \rho_l\frac{u_y}{\phi}\frac{\partial u_r}{\partial y} + \rho_l\frac{\beta}{\phi}\frac{\partial\phi}{\partial t}u_r \\ = -\phi\frac{\partial p}{\partial r} + \frac{1}{r}\frac{\partial(r2\mu\frac{\partial u_r}{\partial r})}{\partial r} - \frac{2\mu u_r}{r^2} + \frac{\partial(\mu\frac{\partial u_y}{\partial r} + \mu\partial\frac{\partial u_r}{\partial y})}{\partial y} + \mu\frac{\beta}{3}\frac{\partial(\frac{\partial\phi}{\partial t})}{\partial r} - \frac{\mu\phi u_r}{k_n}\end{aligned} \tag{11}$$

$$\begin{aligned}\rho_l\frac{\partial u_y}{\partial t} + \rho_l\frac{u_r}{\phi}\frac{\partial u_y}{\partial r} + \rho_l\frac{u_y}{\phi}\frac{\partial u_y}{\partial y} + \rho_l\frac{\beta}{\phi}\frac{\partial\phi}{\partial t}u_y \\ = -\phi\frac{\partial p}{\partial y} + \frac{1}{r}\frac{\partial[r(\mu\frac{\partial u_y}{\partial r} + \mu\partial\frac{\partial u_r}{\partial y})]}{\partial r} + \frac{\partial(2\mu\frac{\partial u_y}{\partial y})}{\partial y} + \mu\frac{\beta}{3}\frac{\partial(\frac{\partial\phi}{\partial t})}{\partial y} - \frac{\mu\phi u_y}{k_p} + \rho_l^*\phi g_y\end{aligned} \tag{12}$$

Where ρ_l^* is applied with Boussinesq assumption: $\rho_l^* = \rho_l\left(\beta_T(T-T_{ini}) - \beta_c(C_L - C_o)\right)$

Undercooling was estimated by the model proposed by Burden et al [39, 40] and given in equation (13).

$$\Delta T = (\frac{GD}{R}) + \frac{\left(-8mR(1-k)C_o\Gamma\right)^{\frac{1}{2}}}{D^{\frac{1}{2}}} \tag{13}$$

The magnitude of undercooling in the present work is not a constant throughout the solidification process but is updated at every time step for each control volume (CV) in the domain.

A simplified version of the Kozeny – Carman model [41, 42] was used to define the permeability in the mushy zone as function of liquid fraction. Asai et al [43] proposed the simplified model in Equation (14). The morphology of the dendrites in Equation (14) is assumed to be conical with a large height to base diameter ratio and the magnitude of permeability in the direction normal to dendrite growth, K_n is identical to its magnitude in the parallel direction, K_p.

$$K_p = K_n = \frac{1}{5\left(\frac{6}{\lambda_1}\right)^2}\frac{\phi^3}{(1-\phi)^2} \tag{14}$$

Initial Conditions

C_o	C_s	**Solidification Mode**	T_{Ini} (°C)	U_r(m.s^{-1})	u_y(m.s^{-1})	ϕ	λ_1(μm)
Al-3wt%Si	$=C_o \times k$	Upward	644.0	0	0	1	300
Al-7wt%Si		Upward	617.3				
Al-5wt%Si		Downward	633.7				
Al-7wt%Si		Downward	620.3				

Boundary Conditions

Boundary conditions for T and C_L are shown in Figure 1 and that for velocities, u_r, and u_y are shown Figure 2. In Figure 1, the thermal boundary condition at the heat extraction boundary are given either as heat transfer coefficient h or function of time, f(t). Function f(t) or heat transfer coefficient was taken from the experiments [29, 30].

Thermal boundary condition at y = 0 for Al-wt7%Si upward solidification is defined as $h = 3900 \times t^{-0.09}$ (W m^{-2} K^{-1}) [29]. The function f(t), shown in Figure 1(a), at y = 0 for Al-3wt%Si upward solidification is determined by the correlation equation from experimental work, Peres et al [29], as shown in equation (15):

$$f(t) = \begin{cases} -12 \times t + 644 \ (t \leq 10s) \\ 637.44 - 63.08 \times \ln(t) + 198.96/\ln(t) - 8.30 \times \ln(t)^2 - 115.26/\ln(t)^2 + 0.89 \times \ln(t)^3 \ (t > 10s) \end{cases} \tag{15}$$

Thermal boundary condition for Al-5wt%Si downward solidification at $y = 0$ is: $h = 2400$ (W m^{-2} K^{-1}) [30]. For Al-7wt%Si downward solidification, thermal boundary condition at $y = 0$ is defined as transient temperature distribution f(t) by correlation equation (16) from experimental work Spinelli et al [30], as shown in Figure 1(b):

$$\begin{aligned} f(t) = {} & 620.35 - 9.89\times t + 9.32\times10^{-2}\times t^{2} + 4.00\times10^{-3}\times t^{3} - 1.60\times10^{-4}\times t^{4} + 2.68\times10^{-6}\times t^{5} - 2.50\times10^{-8}\times t^{6} \\ & + 1.43\times10^{-10}\times t^{7} - 4.90\times10^{-13}\times t^{8} + 9.10\times10^{-16}\times t^{9} - 7.20\times10^{-19}\times t^{10} \end{aligned} \tag{16}$$

Boundary conditions for C_L at $y = 0$ in either upward or downward solidification is defined by equation (17):

$$C_L = \begin{cases} C_o & T > T_{liq} - \Delta T \\ g(\phi) & T = T_{liq} - \Delta T \quad g(\phi)\text{ defined by Equation (7)} \\ g(T) & T < T_{liq} - \Delta T \quad g(T)\text{ defined by Equation (8)} \end{cases} \tag{17}$$

The velocities at the boundaries of the computing domain presented in Figure 1 are shown in Figure 2. In Figure 2, the velocity, $u_y(r)$ at $y = 145$mm is adopted a second order (parabolic) function of r, as discussed in Wang et al [31]. $u_y(r)$ is defined by equation (18):

$$u_y(r) = u_{\max}\left\{1 - \left(\frac{r}{R}\right)^2\right\} \tag{18}$$

where u_{max} is the maximum velocity at $r = 0$ and evaluated by the shrinkage observed during solidification. Volume flow rate (VFR) due to shrinkage at $y = 145$mm is calculated at each time step during simulation and is given in equation (19):

$$VFR = \int_0^H \int_0^{Ri} 2\pi \cdot r\left(\frac{1}{r}\frac{\partial(ru_r)}{\partial r} + \frac{\partial u_y}{\partial y}\right)\cdot dr \cdot dy \tag{19}$$

Ri and H are the radius and height of computing domain, respectively. With values of VFR after each time step, u_{max} could be evaluated and subsequently, the boundary condition could be determined at each time step.

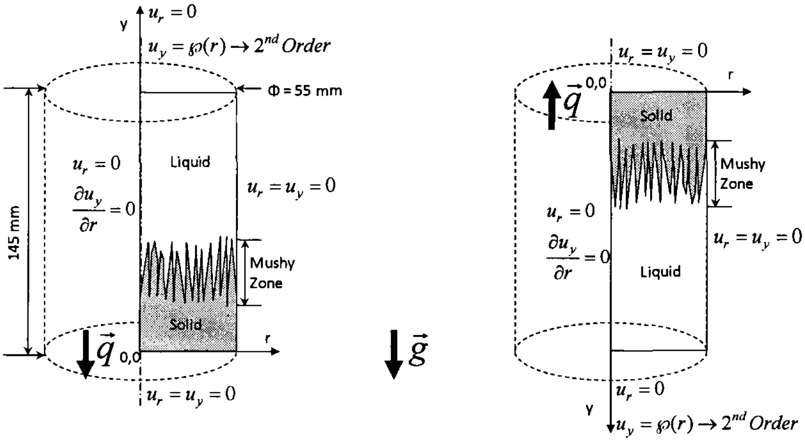

(a) (b)

Figure 2: Velocities at the boundaries of the computing domains presented in Figure 1. (a) upward solidification and (b) downward solidification.

The governing equations (6) to (14) have been solved in the macro simulations. The results of the macro simulations include fluid velocity (u) and transient temperature distribution, which can be used to calculate solidification time, G and R. The evaluated values of G, R and u will be further employed as input parameters for the estimation of λ_1 by using one of the models (1) to (4) and equation (5).

NUMERICAL PROCEDURE

In this study, the new numerical algorithm and method developed by Wang et al [31] has been incorporated with optimized thermo-physical material properties in the solid and liquid phases and considering the effect ΔT in the solidification simulation. The flow chart of the numerical procedure is shown in Figure 3. The salient feature of the new algorithm that distinguishes it from all other solidification simulation algorithms is that the concentration equation is solved first followed by the energy equation in Loop L1. Furthermore, the energy equation is solely used in Loop L1 to obtain the distribution of ϕ in the mushy zone. Loop L4 has been introduced to consider the effect of ΔT and estimate the transient values of λ_1 in the solidifying domain, which was not previously achieved.

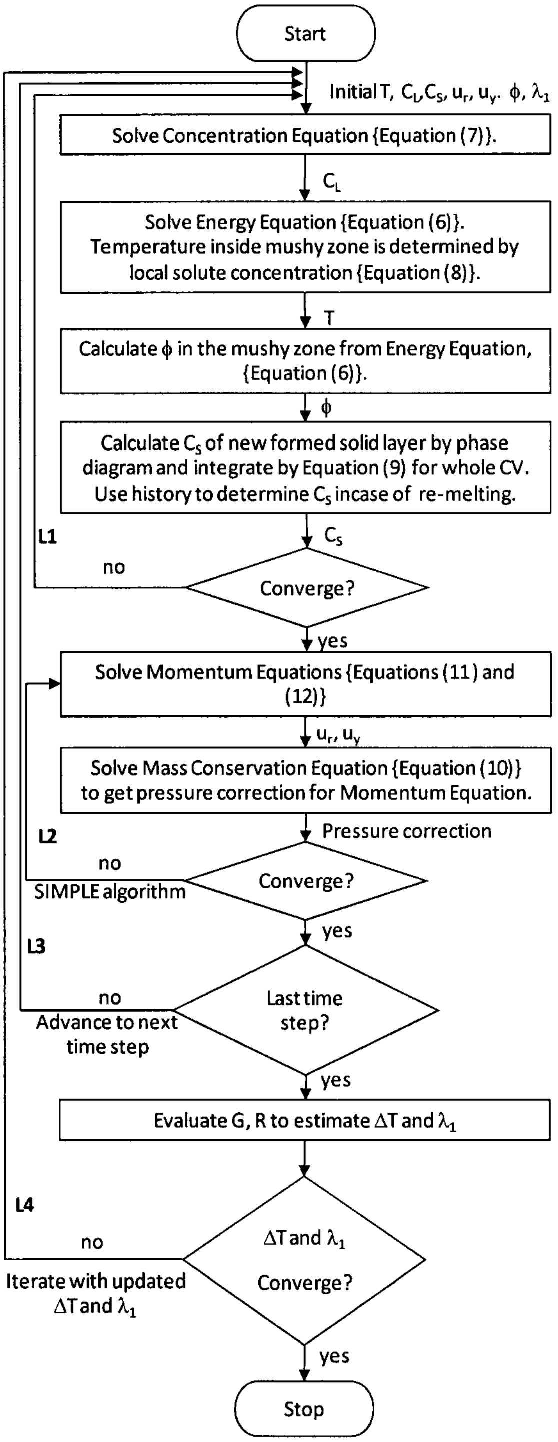

Figure 3: Numerical algorithm developed by Wang et al [31].

Table 1 presents the list and details of the simulations carried out in this study. Simulations S1 and S3 were validated with experiments of Peres et al [29] and simulations S2 and S6 were validated by results from Spinelli et al [30]. All simulations in Table 1 were carried out with the effect of ΔT [31] and using the optimized thermo-physical material properties Wang et al [32]. Since simulations in macro scale are transient problems, λ_1 determined by the macro parameters is not constant and is function of y inside computational domain, which is defined as instantaneous λ_1 as shown in Table 1. For example, simulation S3 is applied with instantaneous values of λ_1. The maximum value of λ_1 obtained from simulation S3 was used as a constant input in simulation S4 to obtain the distribution of G, R and u. Hence for simulation S4, loop L4 in Figure 3 was carried out only to update values of ΔT. A similar approach was used in simulations S6 and S7 wherein the instantaneous values of λ_1 was evaluated in S6 and the maximum value determined from S6 was used to evaluate the solidification parameters in S7. The aim is to evaluate the effect of using either instantaneous transient values of λ_1 or one constant value on the solidification parameters. Figure 3 shows the flow chart outlining the details of the numerical procedure used in the present solidification simulation. A detailed explanation of this procedure is presented in Wang et al [31].

Table 1: Identification and details of the simulations carried out.

Simulation Identification	Solidification Mode	C_o	λ_1	Flow
S1	Upward	Al-7wt%Si	Instantaneous(variable)	Yes
S2	Downward	Al-7wt%Si	Instantaneous(variable)	Yes
S3	Upward	Al-3wt%Si	Instantaneous(variable)	Yes
S4	Upward	Al-3wt%Si	Maximum(constant)	Yes
S5	Upward	Al-3wt%Si	Instantaneous(variable)	No
S6	Downward	Al-5wt%Si	Instantaneous(variable)	Yes
S7	Downward	Al-5wt%Si	Maximum(constant)	Yes
S8	Downward	Al-5wt%Si	Instantaneous(variable)	No

RESULTS AND DISCUSSION

The results and discussion will be presented in the following sections:

- Validation of numerical results by experiments
- Estimation of λ_1
- Effect of λ_1 on fluid flow, G and R
- Effect of fluid flow on G, R and λ_1

Validation of Numerical Results by Experiments

The experiment results by Peres et al [29] for upward solidification of Al-7wt%Si and Al-3wt%Si alloys were used for validating the transient temperature distribution and solidification times (location of mushy zone/liquid interface with time) evaluated by simulations S1 and S3. The experiment results by Spinelli et al [30] for downward solidification of Al-7wt%Si and Al-5wt%Si alloys were used for validating the transient temperature distribution and solidification times.

Figure 4(a) shows a typical validation for the transient temperature distribution at r = 0 and y = 4, 18, 34, 49 and 64 mm from the heat extraction boundary for the upward solidification of Al-3wt%Si alloy; and Figure 4(b) shows that for the downward solidification of Al-7wt%Si alloy at r = 0 and y = 8, 22, 36 and 57 mm from the heat extraction boundary. Figure 4 shows good agreement of both the upward and downward numerical solidification simulations. Figure 5 shows comparison of solidification times predicted by simulations S1, S3, S2 and S6 and experiment results for upward solidification reported in [29] and experimental results for downward solidification reported in [30]. Figure 4 and Figure 5 show good agreement between the experiment results and numerical results of the respective simulations.

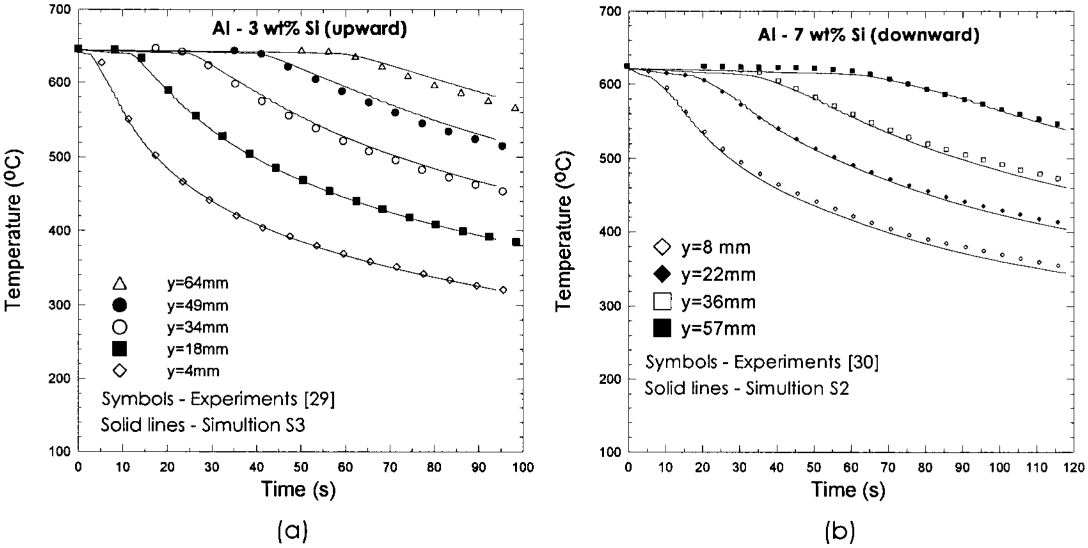

(a) (b)

Figure 4: comparison of transient temperature distributions for simulations S3 and S2 at r = 0 with experimental data of (a) Peres et al [29] for upward solidification simulation S3 and (b) Spinelli et al [30] for downward solidification simulation S2.

Estimation of λ_1

Figure 6 shows values of λ_1 predicted from simulations S3 (Al-3%wtSi upward solidification) and S6 (Al-5%wtSi downward solidification) using models given by equations (1) to (4) coupled with the Lehmann model in (equation (5)) compared with experimental results reported in [29, 30]. It can be seen that the best agreement with the experiments is when the Bouchard-Kirkaldy model[27] is used along with the Lehmann model[28]. The Bouchard-Kirkaldy model is the only model that estimates λ_1 in an unsteady solidification process among the ones listed in equations (1) to (4). Hence, in all subsequent simulations, the Bouchard-Kirkaldy model coupled with the Lehmann model have been used to evaluate λ_1.

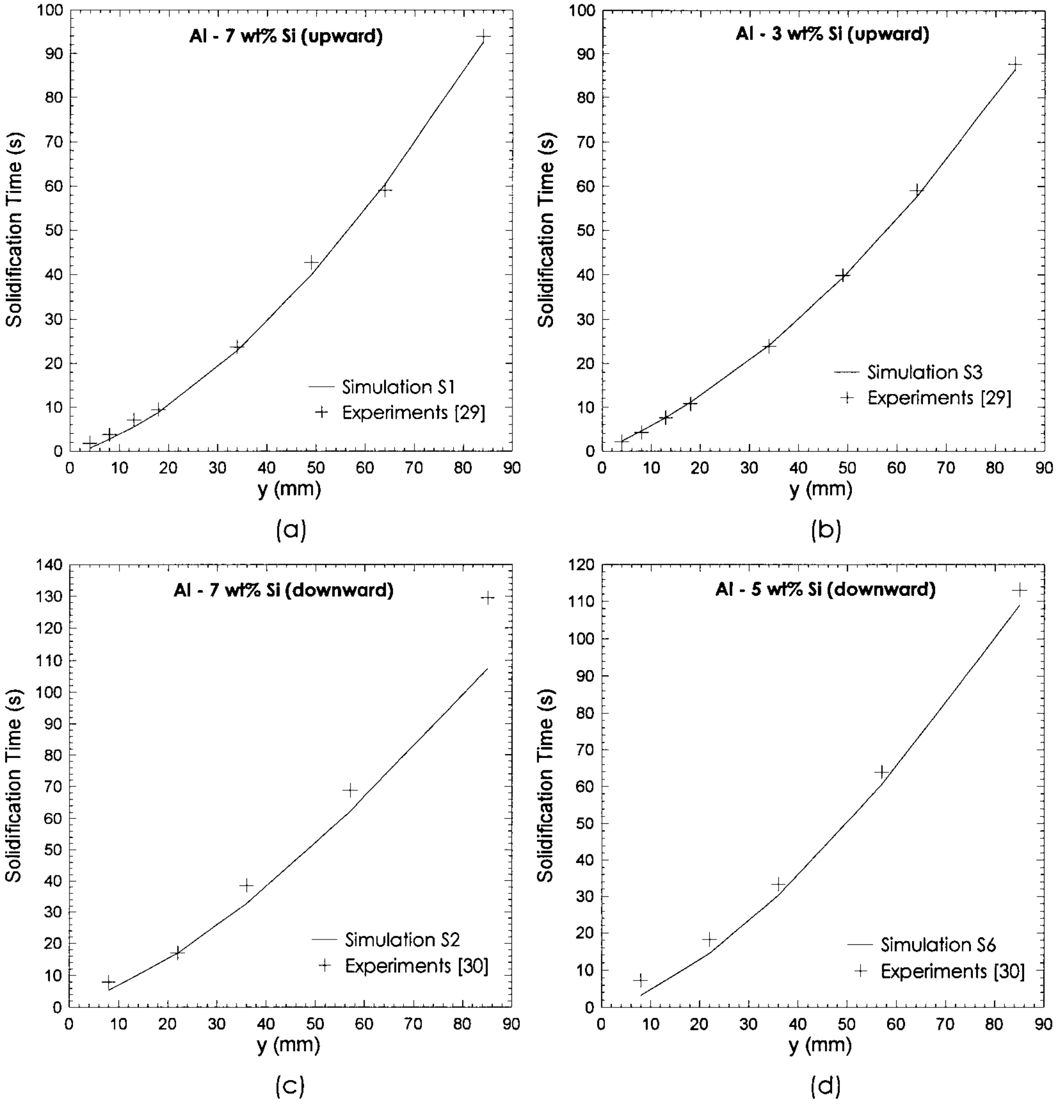

Figure 5: Comparison between solidification times predicted by present numerical investigation and experimental works reported in [29, 30] at r = 0 and at various vertical locations for (a) 7% upward (S1); (b) 3% upward (S3); (c) 7% downward (S2); and (d) 5% downward (S6).

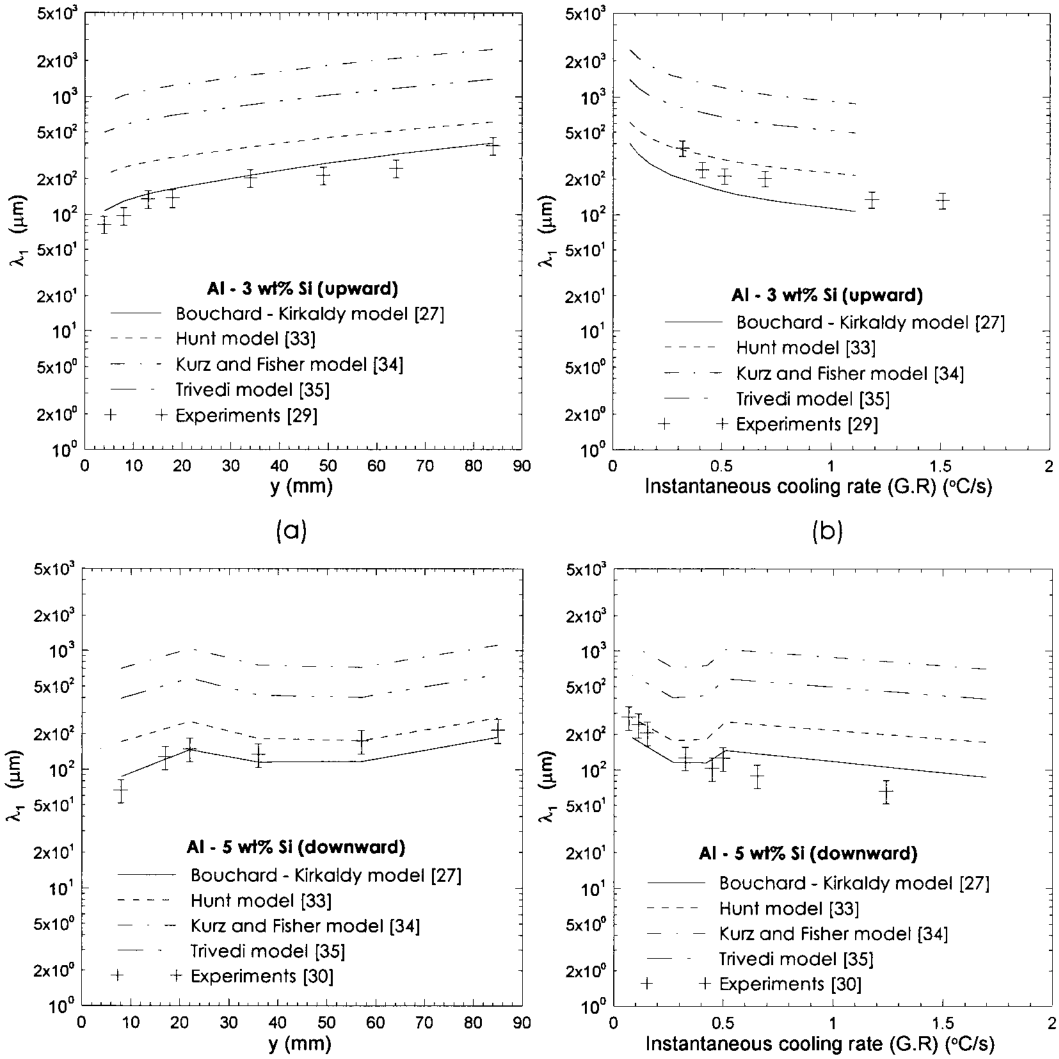

(a) (b)

(c) (d)

Figure 6: Values of λ_1 predicted using various models and the Lehmann model [28] for Al-3wt%Si alloy upward solidification and Al-5wt%Si alloy downward solidification.

Effect of λ_1 on Fluid Flow, G and R

Figure 7(a) and Figure 7(b) show the development of fluid velocity, u for Al-3wt%Si upward solidification simulations S3 and S4, respectively. In Figure 7(a) and Figure 7(b), the magnitude of maximum velocity for each time is shown below each of the respective domain snapshot. Also, shown in these figures are the typical locations of the three zones: *solid, mushy zone and liquid*. The horizontal lines shown in Figure 7(a) and Figure 7(b) in the mushy zone are constant liquid fraction lines.

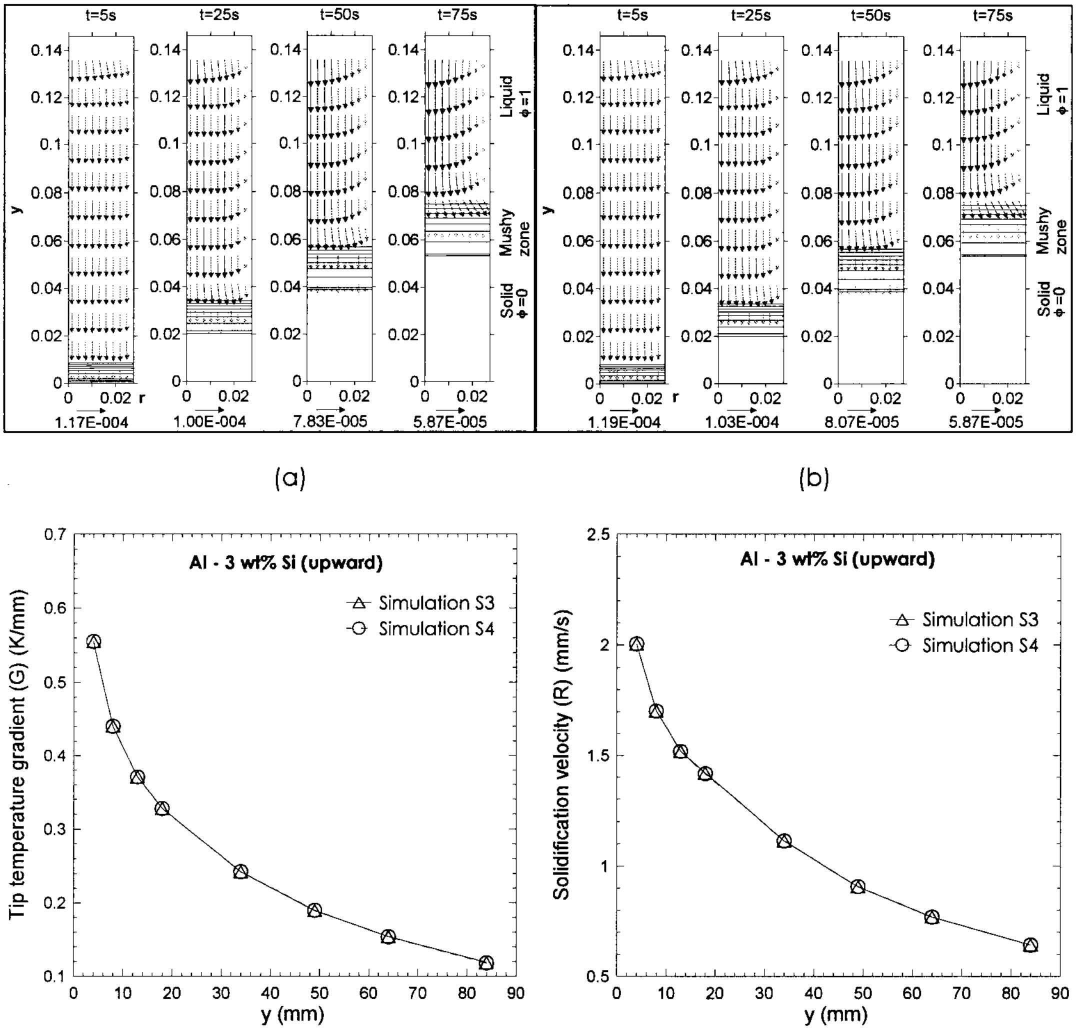

(a) (b)

(c) (d)

Figure 7: Development of fluid flow, G and R for Al-3wt%Si upward solidification. (a) fluid flow in simulation S3 (using instantaneous values of λ_1), (b) fluid flow development in simulation S4 (using maximum value of $\lambda 1$), (c) G in simulations S3 and S4 and (d) R in simulations S3 and S4.

Figure 7 shows that there is no significant variation ($\leq 3\%$) between results obtained in simulations S3 (using instantaneous values of transient λ_1) and S4 (using maximum value of constant λ_1). In upward solidification, the fluid flow is only caused by shrinkage and the positive density gradient is in the direction of gravity vector resulting in no natural convection effect. The difference in S3 and S4 is that in the former the value of λ_1 varies with the location between 100 and 450 μm and in the latter the value of λ_1 is kept at a constant value of 450 μm. The value of λ_1 affects the permeability of the mushy zone (Equation (14)) and the fluid flow in the mushy zone is only due to the effect of solidification shrinkage. During solidification in the mushy zone, liquid fills the voids caused by shrinkage and this will be carried out similar efficiency for a wide range of permeability values (λ_1 values) due to the similar solidification velocity (R) as shown in Figure 7(d) and hence, there is no discernible difference in the fluid flow development between simulations S3 and S4 as shown in Figure 7(a) and Figure 7(b), respectively. Figure 7(c) and Figure 7(d) show distributions of G and R predicted in simulations S3 and S4 showing that the values of G and R are almost identical because fluid flow induced by shrinkage even much smaller than solidification velocity (R). Hence, there is no discernible difference in the solidification parameters whether a range of λ_1 or a constant value of λ_1 is used in simulations of upward solidification.

Figure 8(a) and Figure 8(b) show fluid flow development during downward solidification of Al-5wt%Si alloy predicted in simulations S6 and S7, respectively. In these figures, the magnitude of the maximum fluid velocity is shown on the bottom of each snapshot. In downward solidification, there is enhanced fluid flow in the liquid phase due to natural convection combined with the effect of solidification shrinkage. However, flow due to natural convection cannot penetrate deep into the mushy zone leaving flow in the mushy zone dominated by shrinkage alone for most parts [17, 31]. In Figure 8(a) and Figure 8(b), the initial stages of solidification (flow dominated by shrinkage) are nearly identical. However, after time t = 25s, the effect of natural convection develops and the fluid flow is marginally weaker (lower maximum velocity) in at each time step in simulation S6 wherein a range of λ_1 values were used (100 to 450 μm) than that in simulation S7 wherein a constant value of λ_1 (450μm) was used. The reason is that the permeability of the mushy zone will be greater in simulation S7 at each respective time step due to a higher value of λ_1. Higher permeability in simulation S7 will enhance the fluid velocity at the top of the mushy zone where the flow due to natural convection can penetrate. As a result, a marginally stronger fluid flow development can be observed in simulation S7. Since the flow due to natural convection cannot penetrate deep into the mushy zone, the change in maximum fluid velocity at each respective time step is only marginally greater in S7 as compared to S6. Figure 8(c) and Figure 8(d) show the distribution of G and R in simulations S6 and S7, respectively. Since, the fluid flow in S7 is only marginally stronger than that in S6, there is only a marginal change in the values of G and R at the respective locations after the initial stages of solidification ($t > 14.3$ s). There is almost no change in flow velocity during the initial period of solidification ($t < 14.3$ s) because only little change can be observed during shrinkage dominating period as show in (Figure 8(a) and Figure 8(b)).

Maximum flow in the computing domain can always be observed at left top of the liquid region (centre of the solidifying cylinder) in Figure 8(a) and Figure 8(b) for $t \geq 25$s. Fluid flow with higher temperature from liquid region is driven into mushy zone in this region. Therefore, solidification time will increase in this region and the hence the constant liquid fraction lines get closer along y direction inside mushy zone. With development of clockwise flow, direction of flow velocity at interface of liquid/mushy zone is primarily in the positive r direction. This flow pattern will create accumulation of enthalpy in the right top side of the liquid region (along the wall of the solidifying cylinder). As a result, solidification in this region is slowed down and the constant liquid fraction lines along the walls also get closer as shown in Figure 8(a) and Figure 8(b) for t ≥ 50s.

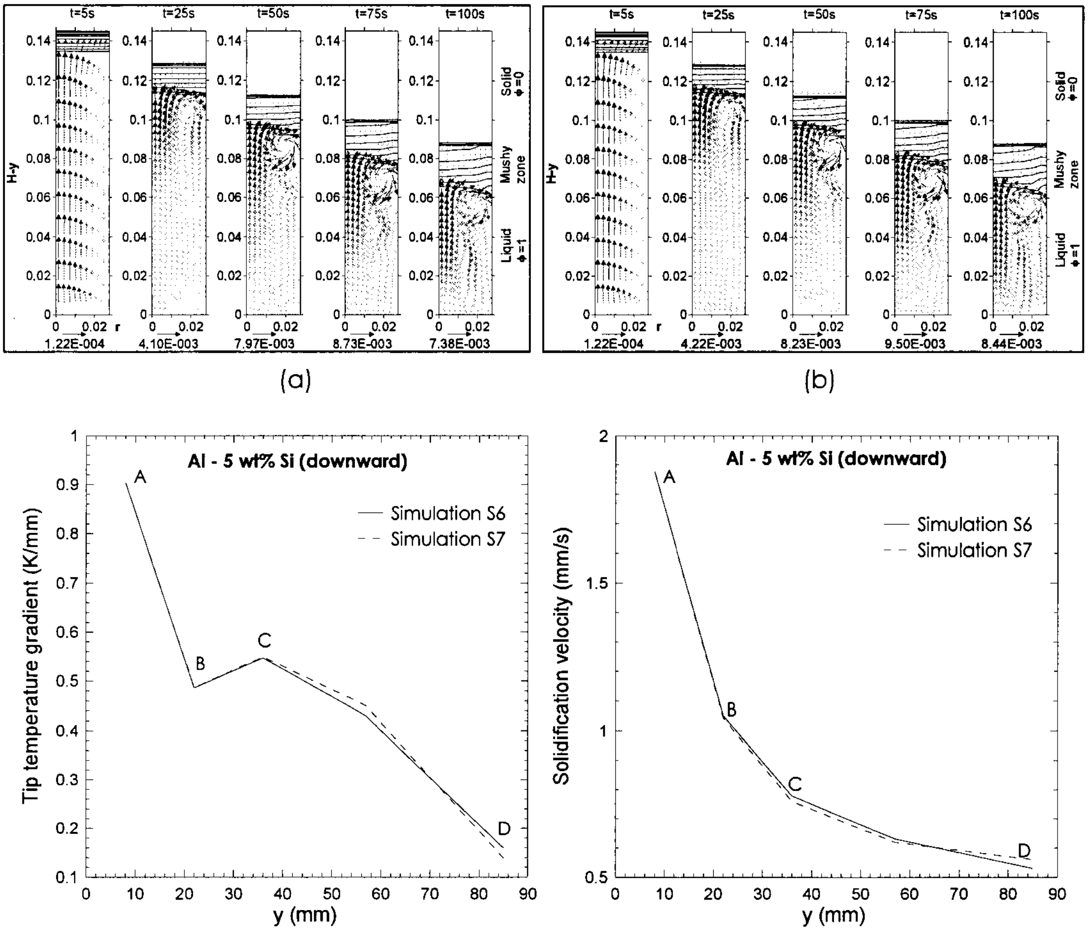

(a) (b)

(c) (d)

Figure 8: Development of fluid flow, G and R for Al-5wt%Si downward solidification. (a) fluid flow development in simulation S6 (instantaneous λ_1), (b) fluid flow development in simulation S7 (maximum λ_1), (c) G in simulations S6 and S7 and (d) R in simulations S6 and S7.

The normalized iso stream function lines at various solidification times inside computational domain are shown in Figure 9(a) and Figure 9(b) in simulations S6 and S7. Maximum magnitude of stream function is shown below each snap shot figure for the respective times. Higher maximum stream function implies stronger fluid flow. The maximum magnitude of stream function (m^3/s) in Figure 9 increases from t = 5s to t = 75s and decreases after t = 75s in both simulations S6 and S7. The development of stream function implies that the strength of flow field changes from weaker to stronger and back to weaker as solidification proceeds. When Figure 9(a) is compared to Figure 9(b), smaller maximum magnitude of stream function can be observed due to the smaller λ_1 applied in simulation S6. However, the variation is not significant as shown in Figure 9. Further, the variation of flow pattern can hardly be observed.

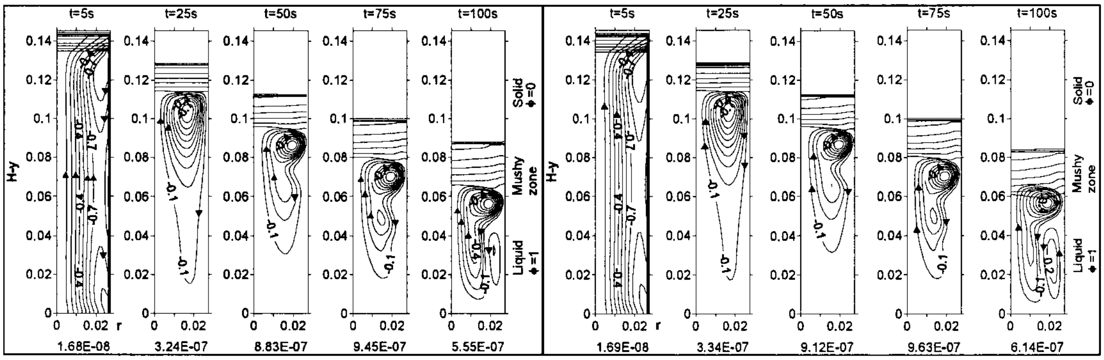

(a) (b)

Figure 9: Development of the iso normalized stream function lines during solidification simulation for Al-5wt%Si downward solidification. (a) with instantaneous values of λ_1 (Simulation S6) (b) with constant maximum value of λ_1 (Simulation S7). The maximum magnitudes of stream function (m^3/s) are presented at the bottom of each snapshot.

Effect of Fluid Flow on G, R and λ_1

Figure 10(a) and Figure 10(b) show the distribution of G and R at various locations in the solidifying domain in simulations S3 (with fluid flow) and S5 (without fluid flow) for Al-3wt%Si alloy during upward solidification. It can be observed that in upward solidification, there is no significant effect on G by fluid flow because, the flow is only caused by solidification shrinkage and the maximum magnitude of this flow is in the order of 10^{-4} $m.s^{-1}$ as shown in Figure 7(a), which is even much smaller than R (Figure 10(b)). The value of R at each respective location decreases by about 6% when fluid flow was considered in simulation S3 as compared to simulation S5 (without fluid flow). With the fluid flow induced by shrinkage, hotter liquid will flow into the CV and delay the solidification process and hence, decreases the value of R at each respective location (Figure 10(b)). Figure 10(c) shows the distribution of instantaneous values of λ_1 as a function of the location y (Figure 1) for the upward solidification of Al-3wt%Si alloy with the effect of fluid flow (S3) and without (S5). This figure shows that there is no discernible difference in the values of λ_1 between simulations S3 and S5. There are two reasons: 1. There is insignificant change in value of R and G between S3 and S5 in upward solidification (Figure 10(a) and Figure 10(b)); 2. Fluid velocity (Figure 7(a)) is much smaller than R (Figure 10(b)).

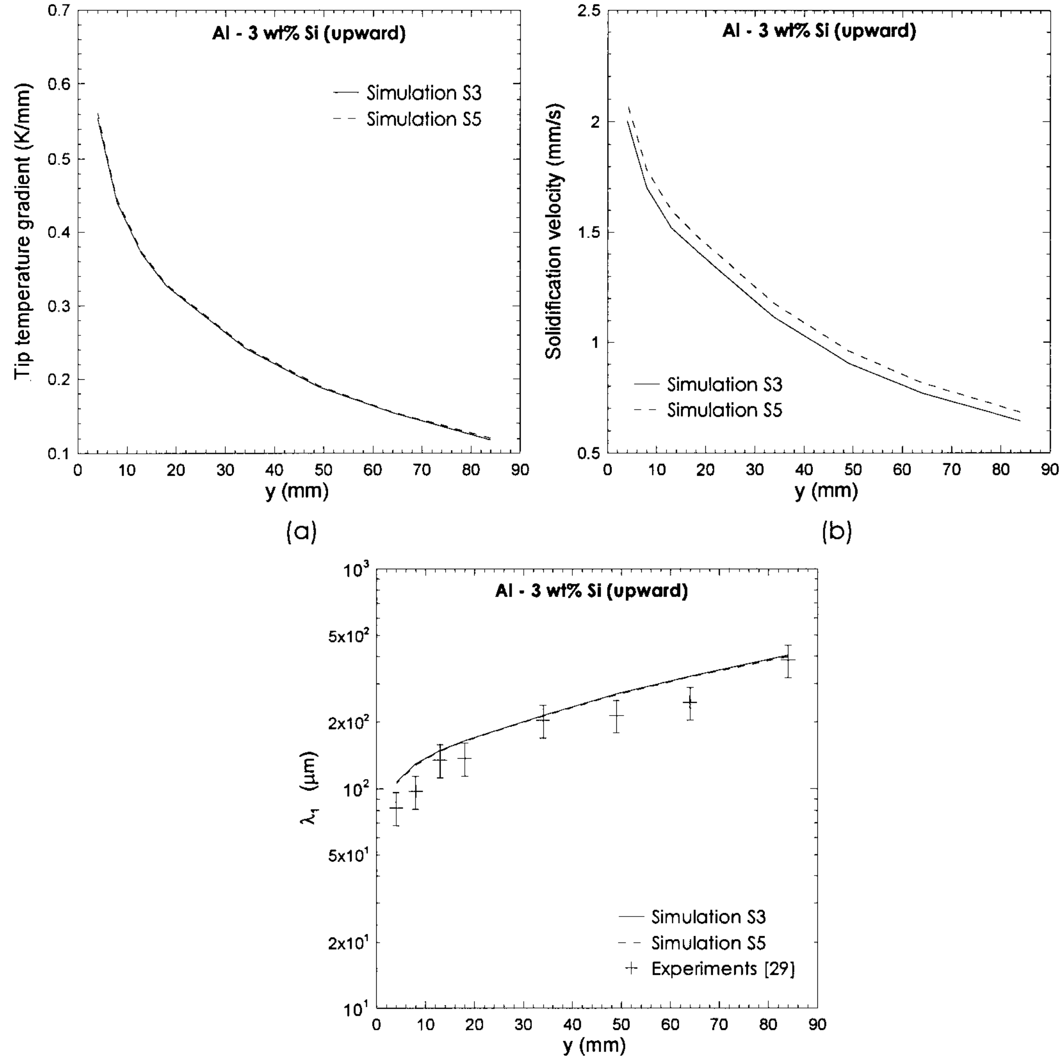

(a)

(b)

(c)

Figure 10: Effect of fluid flow on (a) G, (b) R and (c) λ_1 in upward Al-3wt%Si solidification in simulations S3 (with fluid flow) and S5 (without fluid flow).

Figure 11 shows the effect of fluid flow on G, R and the instantaneous values of λ_1 in the downward solidification simulations S6 (with fluid flow) and S8 (without fluid flow) for Al-5wt%Si alloy. As mentioned above in the discussion for Figure 8, there are three regions during solidification marked by points A, B, C and D at four locations in the domain. Figure 11(a) shows that there is no appreciable change in the value of G between points A and B because, only shrinkage dominates fluid flow in this region and the maximum velocity of the flow is in the order of 10^{-4} m.s^{-1} (Figure 8(a)). Around location B, the effect of the positive density gradient against the direction of the gravity vector introduces natural convection fluid flow in the domain. This will significantly increase the fluid velocity in the domain in simulation S6 as compared to the absence of fluid flow in S8. The increased fluid flow in S6 will increases the value of G between points B and C. At around point C, the fluid velocity due to natural convection gets weaker and continues to decrease to point D. At point D, because the fluid flow in simulation S6 enhances heat transfer condition inside liquid region during solidification, the bulk temperature away from the mushy zone/liquid interface decreases to a point where G becomes comparable between S6 and S8 simulations. Figure 11(b) shows that the value of R in simulation S6 is lower than S8 at all locations because shrinkage will result in hotter fluid flowing into the CV and reducing the solidification rate and the value of R. Figure 11(c) shows the values of λ_1 at various locations in the domain. There are four curves shown in Figure 11(c):

(i) simulation S8 without fluid flow,
(ii) simulation S6 with fluid flow. Effect of fluid flow in domain was not considered in evaluating λ_1 (only Bouchard-Kirkaldy model, equation (4)),
(iii) simulation S6 with fluid flow. Effect of fluid flow in domain was considered in evaluating λ_1 (use of both Bouchard-Kirkaldy model (equation (4)) and Lehmann model (equation (5)), and
(iv) results from experiments [30].

In Figure 11(c), the three regions shown by points A, B, C and D could only been seen in the simulation S6 wherein the fluid flow was used to evaluate λ_1 (curve (iii)) and experiment results (curve (iv)) [30], alike. However, curves (i) and (ii) do not show these three regions because the fluid flow was absent in curve (i) and not used to evaluate λ_1 in curve (ii). In Figure 11(c), it can be observed that the curve (iii) (simulation S6) is in good agreement with the values of λ_1 reported in experimental works [30] and the three regions from the simulation are also in good agreement with those found in the experiments. In region marked by A to B, all the three simulation curves show a similar value of λ_1 (increasing) because the fluid flow is mainly caused by shrinkage in this region. Further, the velocity of the flow is quite low (~10^{-4} m.s^{-1}). In the region marked by B and C, the fluid velocity increases for curves (ii) and (iii). However, the value of λ_1 evaluated with the effect of the fluid flow in curve (iii) decreases alone, because λ_1 is evaluated by considering Lehmann model (equation (5)) in curve (iii). Since only equation (4) is used to evaluate λ_1 in curve (ii), the value of λ_1 only changes marginally in this region without putting the effect of fluid flow for evaluating λ_1. The value of G is higher and R is lower with consideration of fluid flow (S6) as compared with those in S8 as shown in Figure 11(a) and Figure 11(b). When these two parameters in S6 are applied for the evaluation of λ_1 for curve (ii), there is only a marginal decrease in the value of λ_1 in curve (ii) as compared to curve (i) (calculated from parameters in S8). At point D, the value of G for curves (ii) is slightly lower than that for curve (i) and the value of R is lower for curve (ii) than that for curve (i) and hence, the value of λ_1 (estimated by equation (4)) is slightly higher in curve (ii) than that in curve (i).

It can be summarized that the use of fluid velocity in the domain to evaluate the value of λ_1 is critical and makes a significant difference in the estimation of λ_1. Moreover, an accurate evaluation of the fluid flow is important for the valid estimation of λ_1.

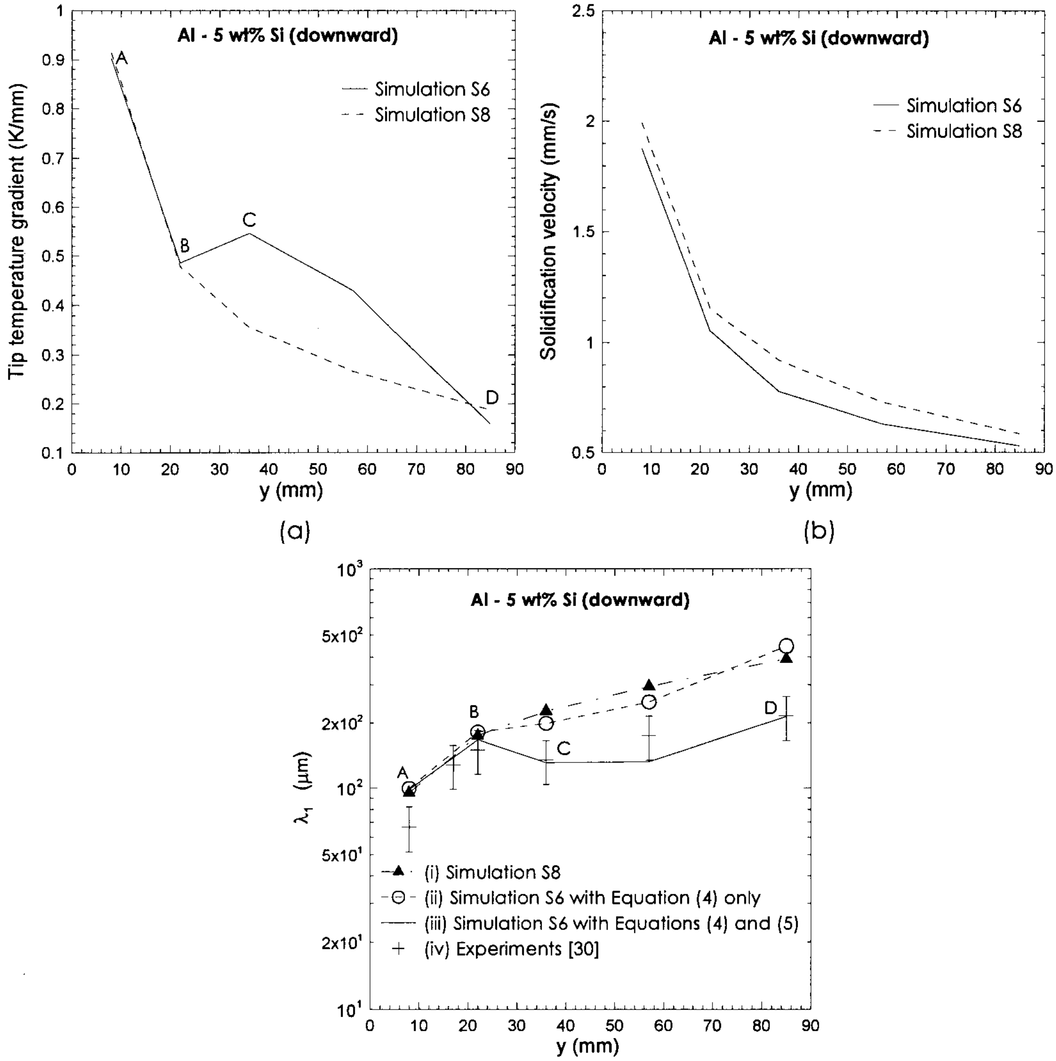

(a)

(b)

(c)

Figure 11: Effect of fluid flow on (a) G and (b) R (c) λ_1 during Al-5wt%Si downward solidification for simulation S6 (with fluid flow) and S8 (without fluid flow).

SUMMARY AND CONCLUSIONS

Numerical simulations were carried out to investigate macro-scale solidification parameters, such as transient temperature distribution, fluid flow, G and R, for upward and downward solidification of hypoeutectic Al-Si alloys. These macro-scale solidification parameters were used to evaluate the micro-scale value of λ_1 by various theoretical and empirical equations. Effect of magnitude and type of fluid flow in the domain on G, R and λ_1 was investigated. Further, effect of λ_1 on G, R and fluid flow was also studied.

The following are the salient conclusions from this study:

- The algorithm and numerical method used in this study for solidification simulation of binary alloys has been successfully validated by experiment results from parameters: T, solidification time and λ_1.
- In the absence or with low values of flow velocity in the solidifying domain (upward solidification mode), the Bouchard-Kirkaldy model to evaluate the primary arm spacing in a binary Al-Si hypoeutectic alloy is the best among the various models available in the literature such as the Hunt, Trivedi and Kurz-Fisher models. Amongst these models, the Bouchard-Kirkaldy model is the only one that evaluates λ_1 proposed for an unsteady solidification process.
- In the presence of strong fluid flow in the solidifying domain (downward solidification mode), the Bouchard-Kirkaldy model coupled with the Lehmann model to estimate the primary arm spacing with fluid velocity values is in good agreement with the experiment results as compared to the other models coupled with the Lehmann model.
- The use of any constant value of the primary arm spacing in the range of 100 to 450 μm do not create an appreciable change in the fluid type and velocity, G and R in the domain during the upward solidification. In the downward solidification, the use of any constant value of the primary arm spacing in the range of 100 to 450 μm only causes a marginal change in the fluid velocity, G and R. Hence, the estimation of flow type and velocity, G and R by an approximate average value of λ_1 is acceptable.
- The fluid flow is only caused by shrinkage in the upward solidification mode and the value of the flow velocity is in the order of 10^{-4} m.s^{-1} and hence, there is no appreciable effect of considering fluid flow on G, R and λ_1 at any location in the solidifying domain.
- In downward solidification mode, initially, the shrinkage mostly dominated the fluid velocity and type. After a short period of time, the effect of natural convection begins to dominate the fluid flow and significantly increases the flow velocity by one to two orders of magnitude which will significantly increase the value of G and decrease the value of λ_1 in the solidifying domain. Once, the effect of natural convection gets weaker, the value of G and λ_1 again decrease and increases, respectively. The effect of natural convection induced fluid flow does not alter the value of R significantly.
- While evaluating the primary arm spacing in the downward and horizontal solidification mode (presence of strong fluid flow caused by natural convection), the effect of instantaneous fluid velocity in the domain should be considered (using the Bouchard-Kirkaldy model coupled with the Lehmann model) to achieve a valid prediction of the primary dendrite arm spacing. The estimation of λ_1 without the effect of fluid velocity in the solidifying domain is erroneous.

REFERENCES

[1] JMatPro, 4.1 ed Guildford ,UK.: Sente Software Ltd.

[2] D. P. Sekulic, P. K. Galenko, M. D. Krivilyov, L. Walker, and F. Gao, "Dendritic growth in Al–Si alloys during brazing. Part 2: Computational modeling," *International Journal of Heat and Mass Transfer*, vol. 48, pp. 2385-2396, 2005.

[3] Factsage, 5.5 ed Madison, WI, USA.: Computherm LLC.

[4] M. Gunduz and J. D. Hunt, "The measurement of solid-liquid surface energies in the Al-Cu, Al-Si and Pb-Sn systems," *Acta Metallurgica*, vol. 33, pp. 1651-1672, 1985.

[5] J. M. V. Quaresma, C. A. Santos, and A. Garcia, "Correlation between unsteady-state solidification conditions, dendrite spacings, and mechanical properties of Al-Cu alloys," *Metallurgical and Materials Transactions A: Physical Metallurgy and Materials Science*, vol. 31, pp. 3167-3178, 2000.

[6] S. G. Shabestari and F. Shahri, "Influence of modification, solidification conditions and heat treatment on the microstructure and mechanical properties of A356 aluminum alloy," *Journal of Materials Science Letters*, vol. 39, pp. 2023-2032, 2004.

[7] W. D. Bennon and F. P. Incropera, "A continuum model for momentum, heat and species transport in binary solid – liquid phase change systems - I. Model formulation," *International Journal of Heat and Mass Transfer*, vol. 30, pp. 2161-2170, 1987.

[8] W. D. Bennon and F. P. Incropera, "A continuum model for momentum, heat and species transport in binary solid – liquid phase change systems - II. Application to solidification in a rectangular cavity," *International Journal of Heat and Mass Transfer*, vol. 30, pp. 2171-2178, October 1987.

[9] W. D. Bennon and F. P. Incropera, "Numerical analysis of binary solid – liquid phase change using a continuum model," *Numerical Heat Transfer*, vol. 13, pp. 277-296, 1988.

[10] J. C. Heinrich and D. R. Poirier, "The effect of volume change during directional solidification of binary alloys," *Modeling and Simulation in Materials Science and Engineering*, vol. 12, pp. 881-899, Sep. 2004.

[11] C.-J. Ho and R. Viskanta, "Heat transfer during inward melting in a horizontal tube," *International Journal of Heat and Mass Transfer*, vol. 27, pp. 705-716, 1984.

[12] M. J. M. Krane and F. P. Incropera, "Analysis of the effect of shrinkage on macrosegregation in alloy solidification," *Metallurgical and Materials Transactions A: Physical Metallurgy and Materials Science*, vol. 26A, pp. 2329-2339, 1995.

[13] T. Magnusson and L. Arnberg, "Density and solidification shrinkage of hypoeutectic aluminum-silicon alloys," *Metallurgical and Materials Transactions A: Physical Metallurgy and Materials Science*, vol. 32, pp. 2605-2613, Oct. 2001.

[14] E. McBride, J. C. Heinrich, and D. R. Poirier, "Numerical simulation of incompressible flow driven by density variations during phase change," *International Journal for Numerical Methods in Fluids*, vol. 31, pp. 787-800, Nov. 1999.

[15] V. R. Voller and C. Prakash, "Fixed grid numerical modeling methodology for convection - diffusion mushy region phase – change problems," *International Journal of Heat and Mass Transfer*, vol. 30, pp. 1709-1719, 1987.

[16] H. Wang, S. Shankar, and M. S. Hamed, "Numerical model for binary alloy solidification," in *5th International Conference on Computational Heat and Mass Transfer*, Canmore, Canada, 2007, pp. 345-351.

[17] D. Xu and Q. Li, "Gravity- and solidification-shrinkage-induced liquid flow in a horizontally solidified alloy ingot," *Numerical Heat Transfer: An International Journal of Computation and Methodology*, vol. Part A: Applications, 20, pp. 203-221, 1991.

[18] L. S. Yao, "Natural convection effects in the continuous casting of a horizontal cylinder," *International Journal of Heat and Mass Transfer*, vol. 27, pp. 697-704, 1984.

[19] J. C. Ramirez, C. Beckermann, A. Karma, and H.-J. Diepers, "Phase-field modeling of binary alloy solidification with coupled heat and solute diffusion," *Physical Review E*, vol. 69, pp. 051607-1-051607-16, May 2004.

[20] J. A. Warren, W. J. Boettinger, C. Beckermann, and A. Karma, "Phase-field simulation of solidification," *Annual Review of Materials Science*, vol. 32, pp. 163-194, 2002.

[21] C. Beckermann, Q. Li, and X. Tong, "Microstructure evolution in equiaxed dendritic growth," *Science and Technology of Advanced Materials*, vol. 2, pp. 117-126, 2001.

[22] K. R. Elder, M. Grant, N. Provatas, and J. M. Kosterlitz, "Sharp interface limits of phase-field models," *Physical Review E (Statistical, Nonlinear, and Soft Matter Physics)*, vol. 64, pp. 021604/1-021604/18, Aug. 2001.

[23] N. Provatas, N. Goldenfeld, and J. Dantzig, "Modeling solidification using a phase-field model and adaptive mesh refinement," *Solidification 1999. Proceedings*, pp. 151-160, 1999.

[24] A. Karma and W.-J. Rappel, "Phase-field method for computationally efficient modeling of solidification with arbitrary interface kinetics," *Physical Review E (Statistical Physics, Plasmas, Fluids, and Related Interdisciplinary Topics)*, vol. 53, pp. R3017-R3020, 1996.

[25] J. H. Jeong, N. Goldenfield, and J. A. Dantzig, "Phase field model for three-dimensional growth with fluid flow," *Physical Review E.*, vol. 64, pp. 041602 -1-14, 2001.

[26] C. W. Lan and C. J. Shih, "Efficient phase field simulation of a binary dendritic growth in a forced flow," *Physical Review E (Statistical, Nonlinear, and Soft Matter Physics)*, vol. 69, pp. 31601-1-10, 2004.

[27] D. Bouchard and J. S. Kirkaldy, "Prediction of dendrite arm spacings in unsteady- and steady-state heat flow of unidirectionally solidified binary alloys," *Metallurgical and Materials Transactions B (Process Metallurgy and Materials Processing Science)*, vol. 28B, pp. 651-663, Aug. 1997.

[28] P. Lehmann, R. Moreaub, D. Camela, and R. Bolcatob, "A simple analysis of the effect of convection on the structure of the mushy zone in the case of horizontal Bridgman solidification. Comparison with experimental results," *Journal of Crystal Growth*, vol. 183, pp. 690-704, 1998.

[29] M. D. Peres, C. A. Siqueira, and A. Garcia, "Macrostructural and microstructural development in Al-Si alloys directionally solidified under unsteady-state conditions," *Journal of Alloys and Compounds*, vol. 381, pp. 168-181, November 3 2004.

[30] J. E. Spinelli, M. D. Peres, and A. Garcia, "Thermosolutal convective effects on dendritic

array spacings in downward transient directional solidification of Al-Si alloys," *Journal of Alloys and Compounds*, vol. 403, pp. 228-238, Novermber 2005.

[31] H. Wang, "Solidification Simulation of Binary Al-Si Alloys: Prediction of Primary Dendrite Arm Spacing with Macro-scale Simulations (~1mm Length Scale)," in *Department of Mechanical Engineering, McMaster University*, Hamilton, Ontario, Canada, Publication A, Ph. D. Thesis, 2009.

[32] H. Wang, "Solidification Simulation of Binary Al-Si Alloys: Prediction of Primary Dendrite Arm Spacing with Macro-scale Simulations (~1mm Length Scale)," in *Department of Mechanical Engineering* McMaster University, Hamilton, Ontario, Canada, Publication C, Ph. D. Thesis, 2009.

[33] J. D. Hunt, "Solidification and casting of metals," *Proceedings of the International Conference on Solidification and Casting of Metals, The Metals Society, London*, pp. 3-9, 1979.

[34] W. Kurz and D. J. Fisher, "Dendritic growth and limit of stability tip radius and spacing," *Acta Metall.*, vol. 29, pp. 11-20, 1981.

[35] R. Trivedi, "Interdendritic spacing: part II. A. comparison of theory and experiment," *Metallurgical Transactions A (Physical Metallurgy and Materials Science)*, vol. 15A, pp. 977-982, 1984.

[36] S. Steinbach and L. Ratke, "The effect of rotating magnetic fields on the microstructure of directionally solidified Al-Si-Mg alloys," *Materials Science and Engineering A*, vol. 413-414, pp. 200-204, Dec. 15 2005.

[37] M. C. Flemings, *Solidification processing*. New York, NY.: McGraw-hill Book Co., 1974.

[38] S. D. Felicelli, J. C. Heinrich, and D. R. Poirier, "Simulation of freckles during vertical solidification of binary alloys," *Metallurgical Transactions B (Process Metallurgy)*, vol. 22, pp. 847-859, Dec. 1991.

[39] M. H. Burden and J. D. Hunt, "Cellular and dendritic growth. I," *Journal of Crystal Growth*, vol. 22, pp. 99-108, 1974.

[40] M. H. Burden and J. D. Hunt, "Cellular and dendritic growth. II," *Journal of Crystal Growth*, vol. 22, pp. 109-116, 1974.

[41] P. C. Carman, "Fluid flow through granular beds," *Trans. Inst. Chem. Engs.*, vol. 15, pp. 150-156, 1937.

[42] P. C. Carman, "The determination of the specific surface of powders " *I. J. Soc. Chem. Indus.*, vol. 57, pp. 225-234, 1938.

[43] S. Asai and I. Muchi, "Thearoetical analysis and model experiments of the formation mechanism of channel - type segregation," *Transactions of the Iron and Steel Institute of Japan*, vol. 18, pp. 290-298, 1978.